BRNO UNIVERSITY OF TECHNOLOGY
FACULTY OF INFORMATION TECHNOLOGY
DEPARTMENT OF COMPUTER GRAPHICS AND MULTIMEDIA

MODERN FLIGHT CONTROL SYSTEM DESIGN AND EVALUATION

Ph.D. THESIS

AUTHOR Ing. JAN VLK

SUPERVISOR Doc. Ing. PETER CHUDÝ, Ph.D. MBA

BRNO 2020

ABSTRACT

This thesis addresses the research on modern methods in automatic Flight Control System design and evaluation, as seen from the perspective of state-of-the-art and future utilization on Unmanned Aerial Systems. The thesis introduces a Flight Control System design process with a special emphasis on the Model-Based Design approach. An integral part of this process is the creation of the aircraft's mathematical model employed in the flight control laws synthesis and the composition of a simulation framework for the evaluation of the automatic Flight Control System's stability and performance. The core of this thesis is aimed at flight control laws synthesis built around a unique blend of optimal and adaptive control theory. The researched flight control laws originating from the proposed design process were integrated into an experimental digital Flight Control System. The final chapter of the thesis introduces the evaluation of the designed automatic Flight Control System and is divided into three phases. The first phase contains the Robustness Evaluation, which investigates the stability and robustness of the designed control system within the frequency domain. The second phase is the controller's Performance Evaluation employing computer simulations using created mathematical models in the time domain. As for the final phase, the designed Flight Control System is integrated into an experimental aircraft platform, serving as a testbed for future Unmanned Aerial Systems, and subjected to a series of flight tests.

KEYWORDS

Adaptive Control; Aircraft; Equations of Motion; Flight Control System; Flight Parameters; Kalman Filter; Optimal Control; State Estimation; System Linearization; Unmanned Aerial Vehicle.

ABSTRAKT

Tato práce je zaměřena na výzkum moderních metod automatického řízení letu a jejich ověření s ohledem na současný stav poznání a budoucí využití bezpilotních letadlových systémů. Práce představuje proces návrhu automatického systému řízení letu s důrazem na přístupy z oblasti návrhu založeného na modelování (Model-Based Design). Nedílnou součástí tohoto procesu je tvorba matematického modelu letounu, který byl využit k syntéze zákonů řízení a k vytvoření simulačního rámce pro evaluaci stability a kvality regulace automatického systému řízení letu. Jádro této práce se věnuje syntéze zákonů řízení založených na unikátní kombinaci teorie optimálního a adaptivního řízení. Zkoumané zákony řízení byly integrovány do digitálního systému řízení letu, jenž umožňuje vysoce přesné automatické létání. Závěrečná část práce se zabývá ověřením a analýzou navrženého systému řízení letu a je rozdělena do 3 fází. První fáze ověření obsahuje evaluaci robustnosti a analyzuje stabilitu a robustnost navrženého systému řízení letu ve frekvenční oblasti. Druhá fáze, evaluace kvality regulace, probíhala v rámci počítačových simulací s využitím vytvořených matematických modelů v časové oblasti. V poslední fázi ověření došlo k integraci navrženého systému řízení letu do experimentálního letounu, sloužícího jako testovací platforma pro budoucí bezpilotní letadlové systémy a jeho evaluaci v rámci série letových experimentů.

KLÍČOVÁ SLOVA

Adaptivní řízení; bezpilotní letadlo; estimace stavu; Kálmánův filtr; letové parametry; letadlo; linearizace systému; pohybové rovnice; robustní řízení; systém řízení letu.

CONTENTS

1 INTRODUCTION 1
1.1 State-of-the-Art in Flight Control System Design . . . 1
1.2 Goals and Contribution of the Thesis . . . 4
1.3 Outline of the Thesis . . . 6
2 FLIGHT DYNAMICS 8
2.1 Nonlinear Equations of Motion . . . 8
2.2 Aircraft State-Space Representation . . . 11
3 AIRCRAFT SIMULATION MODEL 14
3.1 Mass, Inertia and Gravity Model . . . 15
3.2 Propulsion System Model . . . 16
3.3 Actuator Model . . . 16
3.4 Sensor Model . . . 18
3.5 Atmospheric Model . . . 20
3.6 Aerodynamic Model . . . 25
3.7 Plant Model . . . 25
4 PARAMETER ESTIMATION 28
4.1 Model for Parameter Estimation . . . 29
4.2 Equation Error Method . . . 31
4.3 State Estimation Techniques . . . 31
5 CONTROL SYSTEM SYNTHESIS 35
5.1 LQR-based Flight Control System Synthesis . . . 35
5.2 Model Reference Adaptive Control . . . 40
6 DIGITAL FCS IMPLEMENTATION 46
6.1 Linear Quadratic Regulator Implementation . . . 46
6.2 Linear Quadratic Gaussian Controller Implementation . . . 47
6.3 Model Reference Adaptive Control Implementation . . . 48
6.4 Code Generation . . . 50
7 DIGITAL FLIGHT CONTROL SYSTEM EVALUATION 52
7.1 Robustness Evaluation . . . 53
7.2 Performance Evaluation . . . 61
7.3 Flight Test Evaluation . . . 72
8 CONCLUSION 85
8.1 Summary . . . 85
8.2 Thesis Contributions . . . 86
8.3 Future Development . . . 86

LIST OF ACRONYMS

AAS	Automatic Approach System
ADC	Air Data Computer
AGL	Above Ground Level
BFF	Body-Fixed Frame
C2	Command and Control
CAS	Control Augmentation System
CDU	Control Display Unit
CG	Center of Gravity
COTS	Commercial of the Shelf
DE	Differential Equation
DNP	Digital Navigation Platform
EASA	European Aviation Safety Agency
ECI	Earth-Centered Inertial
EKF	Extended Kalman Filter
EMA	Electro-Mechanical Actuator
EOM	Equations of Motion
FAA	Federal Aviation Administration
FBW	Fly-by-Wire
FCC	Flight Control Computer
FCS	Flight Control System
FMS	Flight Management System
GA	General Aviation
GNSS	Global Navigation Satellite System
GPS	Global Positioning System
HOTAS	Hands on Throttle and Stick

IAS	Indicated Airspeed
ICAO	International Civil Aviation Organisation
ILS	Instrument Landing System
IMU	Inertial Measurement Unit
LQG	Linear Quadratic Gaussian
LQR	Linear Quadratic Regulator
LSA	Light Sport Aircraft
LTI	Linear Time Invariant
LTR	Loop Transfer Recovery
MBD	Model Based Design
MEMS	Micro Electro Mechanical System
MIT	Massachusetts Institute of Technology
MFD	Multifunction Display
MIMO	Multi-Input Multi-Output
MRAC	Model Reference Adaptive Control
NED	North-East-Down
PFD	Primary Flight Display
PMU	Propulsion Monitoring Unit
RPA	Remotely Piloted Aircraft
RPAS	Remotely Piloted Aircraft Systems
RPS	Remote Pilot Station
SAS	Stability Augmentation System
TAS	True Airspeed
UAS	Unmanned Aerial Systems
UAV	Unmanned Aerial Vehicle
UKF	Unscented Kalman Filter
WPT	WayPoint

1 INTRODUCTION

The market segment of Unmanned Aerial Systems (UAS) experienced a remarkable upturn over the period of last decades. The UAS utilization evolved in a response to emerging new advanced technologies and an associated high demand for application flexibility in serving the surveillance, entertainment industry and cargo transport. Various manned aircraft platforms, which were originally designed for sport and recreational flying, could play an important role in the future UAS development, providing accessible and flexible airframes enabling a cost-efficient holistic design and development. A seamless system integration into the air traffic network places strict demands on operational safety, reliability and robustness of UAS. Addressed elements serve as prerequisites for the future design of advanced automatic flight control techniques in this fast evolving segment.

Higher demands on flight endurance and load carrying capacity motivate the conversion of traditionally piloted aircraft to an Unmanned Aerial Vehicle (UAV). However, increased safety requirements have to be considered during such transformation, as well as proper training of UAV operators. Inexperienced UAV operators with limited flight experience can be ill-prepared for solving critical in flight situations related to bad weather conditions, failures or emergencies, which can suddenly evolve into serious accidents. New technologies aimed at enhanced UAV automation and safety improvements are therefore quickly being introduced to the market. However, these rapidly emerging solutions require thorough testing during the design, development and pre-production stages [5, 15].

This thesis introduces the reader to a Model Based Design (MBD) approach in the Flight Control System (FCS) development, harmonized with the state-of-the-art standards, best practices and regulatory requirements. The MBD process usually starts with the aircraft dynamic model development and simulation framework components description. This phase is followed by the control system synthesis and is concluded with system evaluation performed at first within the simulation environment and subsequently during real flight experiments.

1.1 STATE-OF-THE-ART IN FLIGHT CONTROL SYSTEM DESIGN

State-of-the-art control law designs, applied to large transport aircraft FCS, benefit from employing the classical control theory using linear control techniques for a control law synthesis. The Stability Augmentation System (SAS) or Control Augmentation System (CAS) are usually composed of a cascade of transfer functions and designed by employing linear control techniques. A linear approach to control system synthesis has several advantages over the nonlinear one, e.g., the linear control system synthesis is widely introduced in the literature, along with the apparatus for linear closed-loop system stability determination. Another advantage is in the linear control system design's acceptance by the certification authorities, as the stability of the closed-loop can be determined.

The task of SAS is not to navigate the aircraft to a specific heading or climb to a defined altitude, but to assist the pilot in stabilizing the aircraft's attitude. This system is usually necessary for most high-performance aircraft with intentionally reduced stability. The SAS uses the information from onboard sensors, usually from rate gyroscopes and accelerometers, to produce negative feedback to damp out the oscillatory aircraft motion. A good practice in FCS engineering is to design the longitudinal and lateral-directional SAS separately, as the associated longitudinal and lateral-directional modes can be decoupled for most of the flight phases. Basic types of SAS are the pitch, roll, and yaw dampers that utilize the angular rate measurements to stabilize the aircraft motion. Figure 1.1 shows a block diagram of an angular rate SAS.

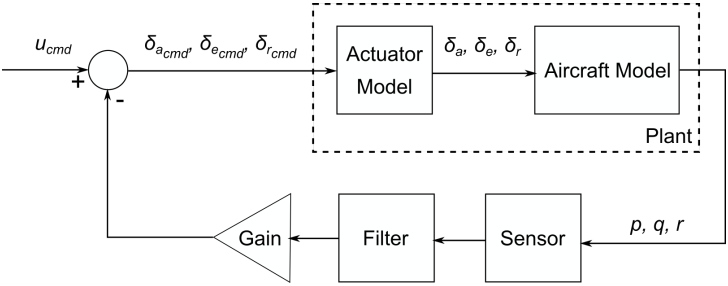

Figure 1.1: Stability Augmentation System.

A CAS is usually employed when high precision command tracking is required. Tasks executed by high-performance aircraft, as maneuvering to its physical limits, require precise control of selected variables, namely the acceleration or angular rates. When compared to SAS, which "only" improves the aircraft handling qualities, the CAS enables the pilot to perform various tasks dependent on precise command tracking, for example, high load factor maneuvering, flight path tracking during an approach and landing, or maneuvering during precise targeting. Basic variables employed in the design of respective CAS are the pitch-rate, normal and lateral accelerations. Figure 1.2 depicts a block diagram of acceleration CAS which also contains the pitch rate stability augmentation introduced in Figure 1.1 and a PI-controller for reference acceleration tracking.

In most cases, the FCS system serves navigation purposes as maintaining commanded altitude, heading, Mach number or airspeed. Other modes may involve an automatic control of specified climb rate or aircraft attitude. All these modes enable pilot overload reduction during the flight. Concerning the mentioned features, the FCS design must comply with legislation specific time domain evaluation criteria, namely the steady-state error, rising time and overshoot during transient motion. The FCS design shall consider respective transient effects during the FCS engage and disengage phases. The best practice is to initiate commanded variables with current values to avoid unwanted and, in some cases, unsafe oscillations, originating from a large difference between commanded and current measured value. Figure 1.3 shows a block

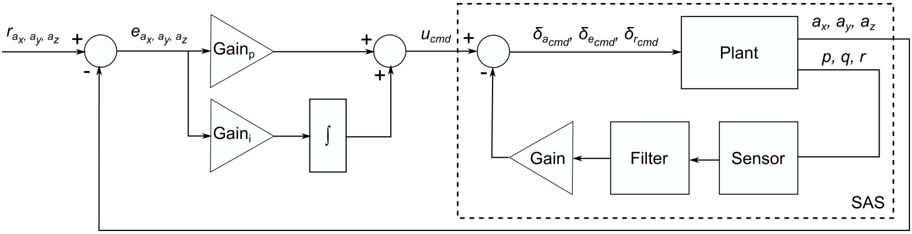

Figure 1.2: Control Augmentation System.

diagram of an altitude-hold FCS. It contains feedback loops of pitch rate stability augmentation, pitch angle hold, and above that, an altitude hold loop containing the controller G_C, in a transfer function form [50].

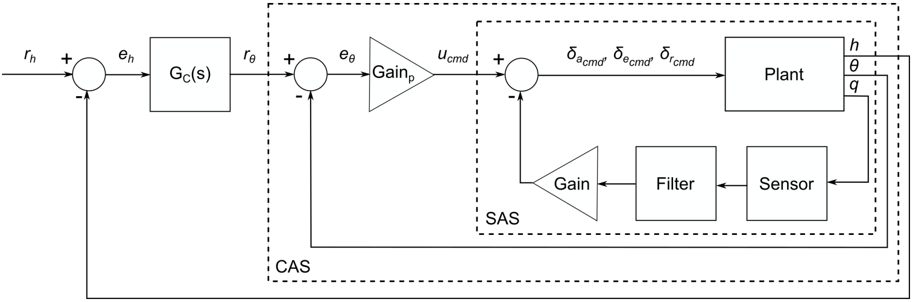

Figure 1.3: Altitude-hold mode.

One of the classical control approach limitations is that a control system's complexity rises with an increasing number of loops (angular rates, attitude, navigation, etc.) and the number of inputs/outputs (measured states and control commands). This limitation can be resolved by employing modern control design techniques that consider the aircraft model in a state-space representation and assesses the FCS for all of its inputs and outputs at once by solving one matrix equation. This unifying approach augments the difference in classical control design, which resolves every single loop separately.

Boeing researchers Wise and Lavretsky successfully employed a modern control design technique known as Linear Quadratic Regulator (LQR). The LQR is a Multi-Input Multi-Output (MIMO) linear control approach that relies on the controlled plant in state-space representation. The LQR is according to [34] one of the most widely used control algorithms. It is a state feedback control technique with excellent robustness characteristics in gain and phase margins and outstanding regulation performance. It is successful in minimizing control usage and has a convenient implementation. This technique solves problems of regulation, but it can easily be extended to command tracking system by adding an integral term. However, this method has some drawbacks as well. For the stability margins to be guaranteed, all states have to be observable. The LQR lacks the noise attenuation capabilities, thus the best practice dictates to use a noise-canceling filter to cancel out the sensor noise. Another drawback of the LQR method is the fact that it requires tuning of weighting matrices. These matrices are necessary for feedback gain calculations. Since the LQR can be used as a baseline control technique for the FCS design, it will be described in detail in following chapters.

A common practice in the FCS integration process is to manually tune the FCS parameters. This practice consumes time and imposes additional costs. On the other hand, the approach introduced in this thesis is focused on Model-Based Design. It utilizes high fidelity aircraft dynamics model for analytic computation of controller settings.

1.2 GOALS AND CONTRIBUTION OF THE THESIS

This work's main contribution can be seen in the complexity and completeness of the FCS design process. It begins with the composition and analysis of a Light Sport Aircraft (LSA) mathematical model, which is later employed in the FCS design. The aircraft model will be used in the simulation framework core that serves the FCS evaluation. The process will continue by investigating various control system methods, their implementation on the target hardware platform and evaluation of their stability, robustness characteristics and performance during computer simulations. Availability permitting, the testing can be optionally augmented by utilization of high fidelity 6 DoF full flight simulator. The whole design process is finalized with the integration of a complete FCS into an experimental aircraft and an execution of flight tests. Figure 1.4 shows the experimental LSA, which will be used as a testing platform for the designed FCS.

Figure 1.4: Testing platform for Flight Control System design.

1.2.0.1 *High Fidelity 6 DoF Nonlinear Aircraft Model*

One of the most critical elements of a model-based FCS design is the composition of a controlled plant's high fidelity dynamics model. High fidelity mathematical representation of a real aircraft has to account for its various subsystems as the aerodynamics, mass and inertia model, sensor and actuator models, etc. to build a reliable framework for the FCS design. Model validation will be performed by comparing the model outputs to measurements collected during flight experiments. Flight measurement data collection and its processing using modern system identification techniques contributes to the high fidelity design process.

1.2.0.2 *Investigation of Modern Flight Control Methods*

Since an experimental LSA has been selected as a testing platform for the FCS implementation, the focus is aimed at linear state feedback or output feedback classes of control methods that can be augmented by the adaptation loop. The relatively limited flight envelope of an experimental LSA, defined by its applicable range of velocities and altitudes, enables a linear baseline controller design. As one of the design requirements is the overall robustness of the control system, the LQR technique will be explored. Model uncertainties will be canceled using adaptive augmentation of the baseline controller using Model Reference Adaptive Control (MRAC) method with its implementation tailored for the LSA dynamic model.

1.2.0.3 *Practical Evaluation of the Designed Flight Control System*

The FCS design process will be finalized with the flight experiment proving suitability of the researched design approach. The in-flight testing provides full evaluation potential compared to computer simulation, and underlines the relevancy of the whole design process. The experience to be gained during the flight test leads to an indisputable improvement potential for the whole FCS design process. The evaluation procedure will be composed of a series of automatic flight tasks, e.g., coordination in turns, maintaining aircraft attitude in steady level flight or optional heading and altitude changes. The evaluation framework will be inspired by the SAE-AS94900 standard Flight Control Systems - Design, Installation, and Test of Piloted Military Aircraft. Using this standard augments the relevancy of the FCS design.

1.2.0.4 *Automatic Approach System for Light Sport Aircraft*

The Automatic Approach System (AAS), as a component of the Automatic Landing System, can be found onboard large transport aircraft. This technology requires both the aircraft and the airport to be equipped with sophisticated and expensive radio-navigation equipment, Instrument Landing System (ILS), which provides the aircraft with information about its precise position relative to the airport runway. The AAS will utilize a combination of smart affordable technologies as Inertial Measurement Unit (IMU), Global Navigation Satellite System (GNSS), and Air Data Measurement unit. The AAS can therefore play an essential role in the segment of safety features at airports not equipped with ILS. Concerning the above mentioned statement, a successful implementation of an AAS designed without radio navigation technologies can be seen as one of the main contributions of this thesis.

1.2.0.5 *Research Goals*

The thesis itself focuses on the research of modern control theory methods, their application in unmanned aviation, stability and performance evaluation during the computer simulations and flight experiments. The following list summarizes the main research goals of the thesis.

- Research and implement a high fidelity 6 DoF nonlinear model of a LSA for the FCS design and evaluation.
- Research and implement suitable aircraft control techniques.
- Evaluate researched control approaches using a high fidelity FCS design framework.
- Integrate the researched FCS control laws into an experimental digital control system onboard a LSA and perform series of practical flight test evaluations.

1.3 OUTLINE OF THE THESIS

The introductory part of this thesis, summarizing historical development of automatic flight control systems, is followed by Chapter 2 dedicated to Flight Dynamics theory, which starts with introducing the 6 DoF nonlinear aircraft model, introduces all aspects of the aircraft motion accounting for respective forces and moments acting on the aircraft and its position changes. The aircraft motion itself is described by a set of first order differential equations called Equations of Motion (EOM). The chapter continues with the description of the linearization process, which leads to state-space representation of linear models. The linear models are used in the subsequent FCS design process steps. The general linearization algorithm is followed by forming respective linear state-space models that describe the longitudinal and lateral-directional motion of modeled aircraft.

The thesis continues with Chapter 3 that describes components for building an aircraft simulation model. The chapter starts with a description of the mass and inertia models and the definition of the gravity model. The subsequent sections introduce the aircraft propulsion system virtualization, composed of a piston engine model supplemented with propeller characteristics and models of sensor and actuator dynamics. The chapter continues with a mathematical description of the surrounding atmosphere, which contains details on continuous turbulence models further utilized within the simulation framework. The turbulence models use Dryden spectral representation taken form MIL-HDBK-1797 [8]. The subsequent section describes abstraction of aerodynamic forces and moments. The chapter is concluded with a description of the Plant model, which is a combination of the aircraft dynamics model with models of sensors and actuators.

Chapter 4 introduces the parameter estimation process employed to improve the aircraft dynamics model fidelity. The chapter describes in detail state estimation techniques, as Kalman Filter, and introduces the Equation-Error method used for aerodynamic parameter estimation. It is concluded with the results of aerodynamic parameter estimation.

Chapter 5 describes the design of the control system itself. This chapter starts with a description of the baseline controller design, which contains a LQR tailored for command tracking purposes. Furthermore, it includes a description of the Linear Quadratic Gaussian (LQG) method, which is a Kalman Filter containing extension of LQR. The Kalman Filter serves as a state estimator for the case when not all states are observable. The adaptive augmentation of the baseline controller called MRAC, which utilizes the Lyapunov stability theory of dynamic systems, is introduced as a next component of Chapter 5 and is responsible for canceling out the matched model uncertainties that may influence aircraft dynamics.

Chapter 6 describes the digital FCS implementation process. The first sections describe the implementation of the researched control laws. The chapter is concluded with the code generation process description.

The performance of the researched FCS is evaluated in Chapter 7. The first part summarizes computer simulations results and employs robustness and performance evaluation tools in frequency and time domains. The following sections present results of flight experiments. They describe the results of the designed FCS testing during aerial navigation when the test pilot performed heading command and altitude or airspeed select tasks. The SAE-AS94900 inspired evaluation of the FCS is introduced in this chapter. The last section of this chapter introduces an AAS results through measurements of aircraft state and control actions during a test flown automatic approach procedure. The final chapter summarizes the thesis and suggests directions for future research.

2

FLIGHT DYNAMICS

This chapter introduces the description of aircraft motion through a set of first order nonlinear differential equation known as EOM. These equations define the translational and rotational velocities, derived using second Newton's law. The set also contains kinematic and navigation differential equations describing aircraft attitude, respectively, its position. The following parts describe simplifications made to the nonlinear model. This simplification process is known as linearization. Linear models in state-space representation are prerequisites to FCS design techniques investigated in this thesis for the flight control design tasks.

The mathematical notation used in this thesis is based on following standards [24, 25, 26].

2.1 NONLINEAR EQUATIONS OF MOTION

Before the rigid body nonlinear equations of motion for an aircraft will be defined, we will summarize the assumptions made during the modeling process in the following list [30, 49]:

- Reference point is in the Center of Gravity (CG).
- Rigid body aircraft $\left(\frac{d}{dt}\right)^{B}(\vec{r}^{RP}) = (\dot{\vec{r}}^{RP})^{B}$.
- Non-rotating Earth $(\vec{\omega}_{K}^{IE}) = \vec{0}$.
- Flat Earth $(\vec{\omega}_{K}^{EO}) = \vec{0}$.
- Quasi-steady mass $\dot{m} = \frac{dm}{dt} \approx 0$.
- Quasi-steady mass distribution $\left(\frac{d}{dt}\right)^{B} I^{R} = 0$.

Some of these assumptions will contribute to the Equations of Motion simplification. The previously stated assumptions are valid, as we are addressing a LSA with a fairly limited flight envelope whose dynamics is rather slow as it usually flies at subsonic speeds and small angles of attack. In another case, if for example, the high-performance fighter aircraft would be described, it would be necessary to consider the effects of rotating spherical Earth, variable aircraft mass, and the equations of motion would become much complex. The extensive description of translational and rotational equations of motion can be found in [3, 10, 48, 41].

The translational motion is influenced by different types of forces acting on the aircraft, namely the aerodynamic forces originating from the airflow over the airframe, gravitational forces caused by Earth's gravity and propulsion forces due to aircraft propulsion system.

The linear momentum time variation is equal to the sum of all external forces acting on the rigid aircraft, as introduced in equation (2.1).

$$\frac{d\vec{p}}{dt} = \sum \vec{F} = \frac{d}{dt} \int \dot{\vec{r}}^{P}(t) \cdot \rho(t) \cdot dV \tag{2.1}$$

The following equation represents a vector in the Body-Fixed Frame (BFF), rotating at an angular rate ω:

$$\left(\frac{d(\cdot)}{dt}\right)_I = \left(\frac{d(\cdot)}{dt}\right)_B + \vec{\omega} \times (\cdot), \tag{2.2}$$

where subscripts I and B refer to the Inertial and the BFF, respectively. Equation 2.3 shows the translational equations of motion in a vector format in the BFF.

$$(\dot{\vec{V}}_K)_B = \frac{1}{m} \cdot (\vec{F}_T^G)_B - (\vec{\omega}_K)_B \times (\vec{V}_K)_B, \tag{2.3}$$

where the variable $(\vec{F}_T^G)_B$ describes the vector of total (T) forces acting in the aircraft CG (G) notated in the BFF (B) that can be described by the sum of gravitational, aerodynamic and propulsion forces

$$(\vec{F}_T^G)_B = \sum (\vec{F}^G)_B = (\vec{F}_G^G)_B + (\vec{F}_A^G)_B + (\vec{F}_P^G)_B, \tag{2.4}$$

and the variable $(\vec{V}_K)_B$ is the vector of aircraft kinematic velocities (K) expressed in the BFF

$$(\vec{V}_K)_B = [u_K, v_K, w_K]^T \tag{2.5}$$

The derivation of the rotational rigid-body equations of motion is also based on Newton's second law. Let $\vec{H}$ be an angular momentum, then the angular momentum time derivation equals the sum of all external moments acting on the body.

$$\frac{d\vec{H}}{dt} = \sum \vec{M} = \frac{d}{dt}(\vec{r}^{P}(t) \times \vec{V}^{P}(t) \cdot m) \tag{2.6}$$

As the angular momentum is simply given by the equation 2.7.

$$\vec{H} = \boldsymbol{I} \cdot \vec{\omega} \tag{2.7}$$

Variable $\boldsymbol{I}$ defines the inertia tensor and $\vec{\omega}$ is the angular rate vector.

$$\vec{\omega} = [p, q, r]^T \tag{2.8}$$

is the angular rate vector. The vector differential that defines the time variation of angular rates is expressed by equation 2.9,

$$(\dot{\vec{\omega}}_K^{IB})_B^B = (\boldsymbol{I}^G)_{BB}^{-1} \left[\overbrace{\sum (\vec{\boldsymbol{M}}^G)_B}^{\text{External moments}} - \overbrace{(\omega_K^{\vec{I}B})_B \times (\boldsymbol{I}^G)_{BB} (\vec{\omega}_K^{IB})_B}^{\text{Inertia cross coupling}} \right] \tag{2.9}$$

where $\sum(\vec{\boldsymbol{M}}^G)_B$ is the sum of all momentum acting in the aircraft's CG and matrix $\boldsymbol{I}_{BB}$ is the aircraft inertia tensor.

The aircraft's attitude in flight is defined using quaternions. This technique has a major advantage over the standard Euler angles stemming from avoiding the manipulation of singularities arising from the aircraft pitch angle reaching the value of $\pm\frac{\pi}{2}$. The attitude differential equations are shown in equation 2.10.

$$\begin{bmatrix} \dot{q}_0 \\ \dot{q}_1 \\ \dot{q}_2 \\ \dot{q}_3 \end{bmatrix} = \frac{1}{2} \begin{bmatrix} 0 & -p & -q & -r \\ p & 0 & r & -q \\ q & -r & 0 & p \\ r & q & -p & 0 \end{bmatrix} - \begin{bmatrix} q_0 \\ q_1 \\ q_2 \\ q_3 \end{bmatrix} \tag{2.10}$$

A mandatory condition the quaternions must fulfill is its unit normalization introduced in equation 2.11.

$$q_0^2 + q_1^2 + q_2^2 + q_3^2 = 1 \tag{2.11}$$

The following functions were employed for the transformation of the quaternions to standard Euler angles that describe the aircraft attitude with respect to the North-East-Down (NED) frame.

$$\begin{bmatrix} \phi \\ \theta \\ \psi \end{bmatrix} = \begin{bmatrix} \tan^{-1}(2\frac{q_1 q_2 + q_0 q_3}{q_0^2 + q_1^2 - q_2^2 - q_3^2}) \\ \sin^{-1}(-2[q_1 q_3 - q_0 q_2]) \\ \tan^{-1}(2\frac{q_2 q_3 + q_0 q_1}{q_0^2 - q_1^2 - q_2^2 + q_3^2}) \end{bmatrix} \tag{2.12}$$

The aircraft position can be defined in different frames, the most used ones are the NED frame, that has cartesian coordinates and expresses aircraft position with respect to selected reference point and the spherical WGS-84 frame and describes aircraft position using geodetic latitude, longitude and height. The position equations using NED frame are introduced in 2.13. The translational velocities u_k, v_k and w_k, are transformed from BFF to NED frame.

$$\begin{bmatrix} \dot{p}_N \\ \dot{p}_E \\ \dot{p}_D \end{bmatrix}_O = \begin{bmatrix} V_N \\ V_E \\ V_D \end{bmatrix}_O = M_{OB} \begin{bmatrix} u_K \\ v_K \\ w_K \end{bmatrix}_B = V \begin{bmatrix} \cos(\chi)\cos(\gamma) \\ \sin(\chi)\cos(\gamma) \\ -\sin(\gamma) \end{bmatrix} \tag{2.13}$$

M_{OB} is a 3×3 transformation matrix defining the relationship between the NED frame and the BFF using Euler angles and trigonometric functions. Another type of position differential equation can be described by airspeed V, the flight path angle γ, and flight path azimuth χ often called track. Position in NED frame is defined by the vector

$$p_O = [p_N, p_E, p_D] \tag{2.14}$$

and accounts for a Flat-Earth assumption. Transforming the position vector from Flat-Earth to the geodetic coordinates or inversely is a common process shown in thesis Appendix.

However, the geodetic coordinates can be computed by using the aircraft velocities as well

$$\dot{\lambda}_G = \left(\frac{v_K}{(N_\mu + h_G)\cos(\mu_G)}\right)_O^E \tag{2.15}$$

$$\dot{\mu}_G = \left(\frac{u_K}{M_\mu + h_G}\right)_O^E \tag{2.16}$$

$$\dot{h}_G = (-w_K)_O^E, \tag{2.17}$$

where the variable λ_G describes the geodetic longitude, variable μ_G is geodetic latitude and h_G the geodetic height. The additional variables M_μ and N_μ are defined by equations

$$\begin{aligned} M_\mu &= a\frac{1-e^2}{(1-e^2\sin^2(\mu_G))^{3/2}} \\ &= N_\mu \frac{1-e^2}{1-e^2\sin^2(\mu_G)} \end{aligned} \tag{2.18}$$

$$N_\mu = \frac{a}{\sqrt{1-e^2\sin^2(\mu_G)}} \tag{2.19}$$

2.2 AIRCRAFT STATE-SPACE REPRESENTATION

The aircraft model to be utilized in the FCS design contains the aircraft's longitudinal and lateral-directional motion description in the form of its state-space representation introduced in the previous section. As defined in previous section, it is possible to decouple the overall state-space model the longitudinal and lateral-directional motion. The condition for steady level flight can be defined by equations 2.20-2.25.

$$\beta = \phi = p = q = r = 0 \tag{2.20}$$

$$\dot{V} = \dot{\alpha} = \dot{q} = \dot{\theta} = \dot{\gamma} = \dot{h} = 0 \tag{2.21}$$

$$\dot{\beta} = \dot{\phi} = \dot{\psi} = \dot{p} = \dot{r} = 0 \tag{2.22}$$

$$V = V_0 \tag{2.23}$$

$$\alpha = \alpha_0 \tag{2.24}$$

$$\theta = \theta_0 \tag{2.25}$$

The subscript 0 in equations 2.23 - 2.25 denotes the trim condition. The longitudinal motion's state vector x_{lon} contains following listed flight quantities: airspeed V, angle of attack α, pitch rate q, flight path angle γ and altitude h. The input vector of longitudinal motion u_{lon} is composed of the throttle lever position δ_T and the elevator deflection δ_e. Based on linearized longitudinal equations it is possible to express the components of the longitudinal state-space model, i.e. the system dynamic matrix A_{lon} and system input matrix B_{lon}, that will be composed of coefficients computed during the linearization process. The experience shows, that derivatives $C_{L_{\dot{\alpha}}}$, $C_{D_{\dot{\alpha}}}$ and $C_{m_{\dot{\alpha}}}$ are very small, therefore the coefficients $Z_{\dot{\alpha}}$, $X_{\dot{\alpha}}$ and $M_{\dot{\alpha}}$ can be neglected, which simplifies the resulting state-space model.

Equations 2.26 through 2.29 introduce the longitudinal motion's state-space model with the state vector x_{lon} and the input vector u_{lon},

$$\dot{x}_{lon} = A_{lon}x_{lon} + B_{lon}u_{lon} \tag{2.26}$$

$$y_{lon} = C_{lon}x_{lon}, \tag{2.27}$$

where

$$x_{lon} = [V, \alpha, q, \gamma, h]^T \tag{2.28}$$

$$u_{lon} = [\delta_T, \delta_e]^T \tag{2.29}$$

Equations 2.30 and 2.31 introduce the internal structures of the longitudinal model's state matrix A_{lon} and the input matrix B_{lon} [50].

$$A_{lon} = \begin{bmatrix} X_V & X_\alpha & X_q & -g\cos(\gamma_0) & X_h \\ Z_V & Z_\alpha & Z_q + 1 & -\frac{g}{V_0}\cos(\gamma_0) & Z_h \\ M_V & M_\alpha & M_q & 0 & M_h \\ -Z_V & -Z_\alpha & -Z_q & \frac{g}{V_0}\cos(\gamma_0) & -Z_h \\ \sin(\gamma_0) & 0 & 0 & V_0\cos(\gamma_0) & 0 \end{bmatrix} \tag{2.30}$$

$$B_{lon} = \begin{bmatrix} X_{\delta_T} & X_{\delta_e} \\ Z_{\delta_T} & Z_{\delta_e} \\ M_{\delta_T} & M_{\delta_e} \\ -Z_{\delta_T} & -Z_{\delta_e} \\ 0 & 0 \end{bmatrix} \tag{2.31}$$

Variables X, Z, M are force and moment coefficients, that are constant for specified trim point condition defined by a combination of velocity and altitude, and are computed during linearization process derived in the previous section. Variables V_0, γ_0 are aircraft states at a trim point. In case of fully observable state vector, the output matrix C_{lon} from equation 2.27 is represented by a simple 5×5 identity matrix [18].

The lateral-directional motion model state x_{lat} is composed of flight quantities including sideslip angle β, roll angle ϕ, heading angle ψ, roll rate p and yaw rate r. Input variables of lateral-directional motion are the aileron δ_a and rudder δ_r deflections, which create the input vector u_{lat}. As the derivative of angle of sideslip doesn't have a significant effect on the lateral-directional model dynamics, the related derivatives $Y_{\dot{\beta}}$, $L_{\dot{\beta}}$ and $N_{\dot{\beta}}$ can be neglected. This assumption simplifies the lateral-directional model's system matrix A_{lat} and input matrix B_{lat}.

The following equations define the state-space representation of lateral-directional dynamics [50].

$$\dot{x}_{lat} = A_{lat}x_{lat} + B_{lat}u_{lat} \tag{2.32}$$

$$y_{lat} = C_{lat}x_{lat} \tag{2.33}$$

$$x_{lat} = [\beta, \phi, \psi, p, r]^T \tag{2.34}$$

$$u_{lat} = [\delta_a, \delta_r]^T \tag{2.35}$$

Equations 2.36 and 2.37 introduce internal structures of the lateral-directional model's state matrix A_{lat} and the input matrix B_{lat}.

$$A_{lat} = \begin{bmatrix} Y_\beta & \frac{g}{V_0}\cos(\alpha_0) & 0 & Y_p + \sin(\alpha_0) & Y_r - \cos(\alpha_0) \\ 0 & 0 & 0 & 1 & \tan(\theta_0) \\ 0 & 0 & 0 & 0 & \frac{1}{\cos\theta_0} \\ L_\beta & 0 & 0 & L_p & L_r \\ N_\beta & 0 & 0 & N_p & N_r \end{bmatrix} \tag{2.36}$$

$$B_{lat} = \begin{bmatrix} Y_{\delta_a} & Y_{\delta_r} \\ 0 & 0 \\ 0 & 0 \\ L_{\delta_a} & L_{\delta_r} \\ N_{\delta_a} & N_{\delta_r} \end{bmatrix} \tag{2.37}$$

Variables Y, L, N are, similarly to the longitudinal case, the force and moment coefficients, which are constant for the specified trim point and are computed during the linearization process. Variables V_0, α_0, θ_0 again refer to aircraft state at trim point. The output matrix C_{lat} from equation 2.33 is a 5×5 the identity matrix as in the longitudinal motion, which means that all lateral-directional states are assumed to be observable.

AIRCRAFT SIMULATION MODEL

3

This chapter introduces the subsystems and mathematical background necessary for building an aircraft simulation model, which will be used throughout the following chapters as part of the researched designed flight control system framework. In fact, the Equations of Motion derived in the previous chapter and their linearized state-space models cover only one part of the model, namely the aircraft dynamics, as shown in Figure 3.1. The remaining necessary flight simulation subsystems will be described in the following sections. The chapter starts with a description of the mass, inertia and gravity models. The subsequent paragraphs are dedicated to the modeling of the propulsion system, and sensor and actuator dynamics. The sensor model is built up around a stochastic description of the measurement noise using the Allan variance technique to precisely express its noise characteristics. The dynamics of both, sensor and actuator models can be conveniently expressed using second-order transfer functions. The chapter continues with the description of the atmospheric model, which contains a detailed specification of the continuous turbulence model inevitable in the evaluation of the researched flight control system's performance. The final section describes in detail the aerodynamic model.

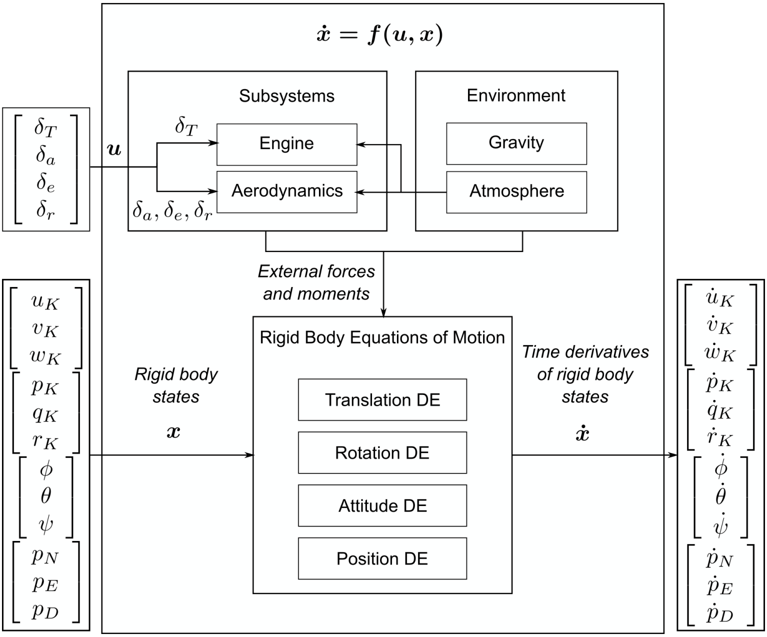

Figure 3.1: State representation of an aircraft simulation model. Source [19]

Chapter 3 is concluded with a description of a plant model, which is a combination of the aircraft and actuator dynamics. This model will be used in the subsequent chapters for the flight control system design.

3.1 MASS, INERTIA AND GRAVITY MODEL

The aircraft total weight m is computed as a sum of empty weight m_{conf} at specific balance configuration and weight of other elements m_i, accounting for the crew, fuel or payload [31]. Total weight calculation formula is shown in equation 3.1.

$$m = m_{conf} + \sum_i m_i \tag{3.1}$$

An instantaneous CG position x_{CG} is defined by elementary weights and associated known CG positions of respective configuration elements using equation 3.2.

$$x_{CG} = \frac{x_{CG_{conf}} m_{conf} + \sum_i x_{CG_i} m_i}{m} \tag{3.2}$$

In order to calculate the rotational dynamics of a simulated aircraft, it is inevitable to carefully compose the resulting inertia tensor $\boldsymbol{I}_{BB}$ [16, 28]. Equation 3.3 shows the inertia tensor's structure, while equations 3.4-3.9 introduce the tensor's elements computation.

$$\boldsymbol{I}_{BB} = \begin{bmatrix} I_{xx} & -I_{xy} & -I_{xz} \\ -I_{xy} & I_{yy} & -I_{yz} \\ -I_{xz} & -I_{yz} & I_{zz} \end{bmatrix} \tag{3.3}$$

$$I_{xx} = \int_m (y^2 + z^2) dm \tag{3.4}$$

$$I_{yy} = \int_m (x^2 + z^2) dm \tag{3.5}$$

$$I_{zz} = \int_m (x^2 + y^2) dm \tag{3.6}$$

$$I_{xy} = \int_m (xy) dm \tag{3.7}$$

$$I_{yz} = \int_m (yz) dm \tag{3.8}$$

$$I_{xz} = \int_m (xz) dm \tag{3.9}$$

The Gravity model is defined by force and moment vectors shown in equations 3.10-3.11, along with their transformations from NED frame to BFF. These transformations are necessary from the model compatibility perspective as other models as aerodynamics or propulsion are developed in BFF [51].

$$(\vec{F}_G)_B = M_{BO} \cdot \begin{bmatrix} X_G \\ Y_G \\ Z_G \end{bmatrix}_0 = M_{BO} \cdot \begin{bmatrix} 0 \\ 0 \\ m \cdot g \end{bmatrix}_0 \tag{3.10}$$

$$(\vec{M}_G)_B = M_{BO} \cdot \begin{bmatrix} L_G \\ M_G \\ N_G \end{bmatrix}_0 = \vec{0} \tag{3.11}$$

3.2 PROPULSION SYSTEM MODEL

The thrust of a propulsion system, made of for example 4-stroke reciprocity combustion engine and propeller, is computed using propeller characteristics containing advance ratio J, thrust coefficient C_T, propeller diameter D_{prop} and propeller or engine revolutions n_{prop}. At first, the advance ratio is defined by equation 3.12.

$$J = \frac{V}{n_{prop} D_{prop}} \tag{3.12}$$

The thrust coefficient C_T can be defined as a function of the advance ratio J. Using the state-of-the-art engineering practice is to approximate this function by a lookup table. The last step is expressing the thrust T using equation 3.13 [46].

$$T = C_T \rho n_{prop}^2 D^4 \tag{3.13}$$

The engine model can be defined using a function relating the engine revolutions to the throttle lever position and the instantaneous operating condition.

3.3 ACTUATOR MODEL

An important aspect of a digital FCS design is the consideration of the actuator's dynamic effects. The modeled actuator dynamics, with its time delays, influences the aircraft's overall dynamic behavior. The actuator model dynamics can be described by a second order transfer function, with properties expressed in terms of its natural frequency ω_{act} and damping ζ_{act} as shown in the equation (3.14) [12].

$$F_{act}(s) = \frac{\omega_{act}^2}{s^2 + 2\zeta_{act}\omega_{act}s + \omega_{act}^2} \tag{3.14}$$

To conveniently combine the actuator model with the state-space representations of the aircraft's longitudinal and lateral-directional motion, the transfer function

$F_{act}(s)$ can be transformed into its state-space representation as introduced in equations (3.15) and (3.16).

$$\dot{x}_{act} = A_{act}x_{act} + B_{act}u_{act} \tag{3.15}$$

$$y_{act} = C_{act}x_{act} \tag{3.16}$$

The actuator's state-space model for longitudinal motion contains a state vector composed of the throttle and elevator deflections along with their associated deflection rates. The actuator model inputs for the longitudinal motion are the respective command values defined in the equation 3.19. The lateral-directional state-space actuator model, on the other hand, contains a state vector composed of aileron and rudder deflections and their associated rates. The actuator model inputs for the lateral-directional motion are the command values defined by equation 3.20. Equations 3.17 and 3.18 show the actuator model state vectors for the longitudinal and lateral-directional motion cases, while equations 3.19 and 3.20, as stated above, show the respective actuator model input vectors for the longitudinal and lateral-directional case.

$$x_{act,lon} = \left[\dot{\delta}_T, \delta_T, \dot{\delta}_e, \delta_e\right]^T \tag{3.17}$$

$$x_{act,lat} = \left[\dot{\delta}_a, \delta_a, \dot{\delta}_r, \delta_r\right]^T \tag{3.18}$$

$$u_{act,lon} = \left[\delta_{T_{cmd}}, \delta_{e_{cmd}}\right]^T \tag{3.19}$$

$$u_{act,lat} = [\delta_{a_{cmd}}, \delta_{r_{cmd}}]^T \tag{3.20}$$

The actuator's state matrix A_{act}, input matrix B_{act} and output matrix C_{act} are introduced in equations 3.21, 3.22, 3.23, 3.24 and 3.25 respectively, and have the same structure for both, the longitudinal and the lateral-directional motion.

$$A_{act,lon} = \begin{bmatrix} -2\zeta_{\delta_T}\omega_{\delta_T} & -\omega_{\delta_T}^2 & 0 & 0 \\ 1 & 0 & 0 & 0 \\ 0 & 0 & -2\zeta_{\delta_e}\omega_{\delta_e} & -\omega_{\delta_e}^2 \\ 0 & 0 & 1 & 0 \end{bmatrix} \tag{3.21}$$

$$B_{act,lon} = \begin{bmatrix} \omega_{\delta_T}^2 & 0 \\ 0 & 0 \\ 0 & \omega_{\delta_e}^2 \\ 0 & 0 \end{bmatrix} \tag{3.22}$$

Variables ζ and ω represent the actuator's damping and natural frequency for thrust and elevator actuator model, respectively. This model is a part of the longitudinal dynamics.

$$A_{act,lat} = \begin{bmatrix} -2\zeta_{\delta_a}\omega_{\delta_a} & -\omega_{\delta_a}^2 & 0 & 0 \\ 1 & 0 & 0 & 0 \\ 0 & 0 & -2\zeta_{\delta_r}\omega_{\delta_r} & -\omega_{\delta_r}^2 \\ 0 & 0 & 1 & 0 \end{bmatrix} \tag{3.23}$$

$$B_{act,lat} = \begin{bmatrix} \omega^2_{\delta_a} & 0 \\ 0 & 0 \\ 0 & \omega^2_{\delta_r} \\ 0 & 0 \end{bmatrix} \tag{3.24}$$

The lateral-directional motion's actuator model contains natural frequency ω and damping ζ characteristics differentiated by subscripts δ_a, δ_r for the aileron and the rudder control respectively.

The output matrix C_{act} introduced in the equation (3.25) is identical for both, the longitudinal and the lateral-directional actuator model, and consist of only two rows, as only the control surface deflections, without the respective rates, are assumed to be measurable [30].

$$C_{act} = \begin{bmatrix} 0 & 1 & 0 & 0 \\ 0 & 0 & 0 & 1 \end{bmatrix} \tag{3.25}$$

3.4 SENSOR MODEL

An unmanned aircraft's sensor network contains several measurement units that influence aircraft state variables in a different manner. The aircraft's accelerations, angular rates and Euler angles can be measured by Micro Electro Mechanical System (MEMS) IMU, usually equipped with a magnetometer to sense the magnetic field. The airspeed and pressure altitude are acquired through a pitot-static system. Finally, the position of an aircraft is sensed by a GNSS receiver. Almost all sensors add some errors into the measurement, either it is noise, drift or time delay.

3.4.1 *Sensor dynamics*

State-of-the-art sensors for UAV applications are mostly based on the MEMS technology. The dynamics of such sensor can be conveniently modeled as a second-order linear system and described by a transfer function. Example of sensor transfer function is shown in equation 3.26.

$$F_{sens}(s) = \frac{\omega^2_{sens}}{s^2 + 2\zeta_{sens}\omega_{sens}s + \omega^2_{sens}} \tag{3.26}$$

The sensor dynamics is characterized by its natural frequency ω_{sens} and by the sensor damping ζ_{sens}. A block diagram of sensor dynamics implementation is shown in Figure 3.2.

3.4.2 *Noise characteristics estimation*

This section describes the process of sensor noise and bias estimations, which are needed for high fidelity sensor modeling. Once estimated these parameters are added to the clean signal in order to create precise sensor output signal comparable to the

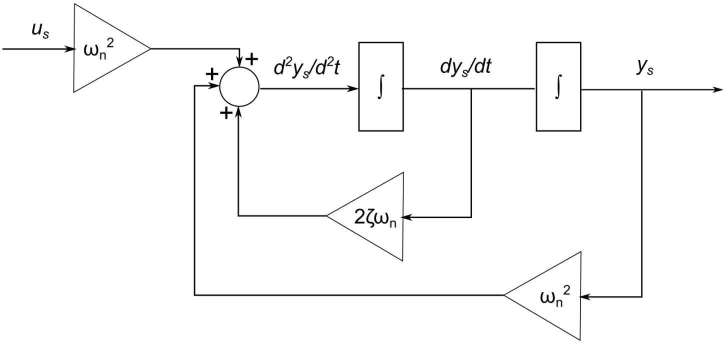

Figure 3.2: Block diagram of sensor dynamics.

real sensor output. The sensor bias can be computed through the utilization of a simple mean calculation over selected signal length under steady conditions, as described in equation 3.27. In the case of specific forces, the signal needs to be compensated for gravity effects [21].

$$b = \frac{1}{N}\sum_{i=1}^{N} A_i \tag{3.27}$$

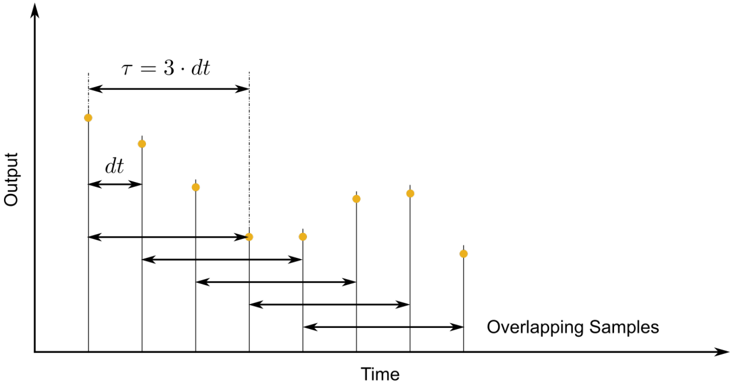

Figure 3.3: Time clusters for Allan variance calculation.

Signal noise power can be estimated by employing the Allan variance technique. This method is usually applicable to oscillator frequency stability measurements. The advantage of this approach is that it can be used without data-sheet information and based only on the measured sensor signal. For this thesis's purpose, the Allan variance calculation of a gyroscope signal will be used for the algorithm explanation. The first step of computing Allan variance is the integration of measured angular velocity samples $\omega(t)$ over the time span t, which results in angle $\theta(t)$.

The Allan variance $\sigma^2(\tau)$ can be computed as a function of τ and $<>$, which is an expression for ensemble average. Equation 3.28 shows the Allan variance formula

$$\sigma^2(\tau) = \frac{1}{2\tau^2} < (\theta_{k+2m} - 2\theta_{k+m} + \theta_k)^2 > \tag{3.28}$$

Variable τ is the so called cluster time, and its width is defined by the parameter m as defined in the following equation.

$$\tau = m \cdot dt \tag{3.29}$$

After explaining ensemble average, the result could be written by equation 3.30.

$$\sigma^2(\tau) = \frac{1}{2\tau^2(N-2m)} \sum_{k=1}^{N-2m} \left[(\theta_{k+2m} - 2\theta_{k+m} + \theta_k)^2 \right] \tag{3.30}$$

The parameter N is the total number of samples and m, as mentioned above, the number of samples in an overlapping cluster time τ. This version of Allan variance algorithm is called overlapping due to the time clusters defined by the parameter τ being overlapping, as shown in Figure 3.3. The noise characteristics can be estimated using the above-defined algorithm in a laboratory experiment, in which accelerometer and gyroscope signals are recorded under steady conditions. The noise characteristics are then extracted from measured signals.

3.5 ATMOSPHERIC MODEL

Future implementations of an aircraft dynamic model include an atmospheric model compliant to the international standard ISO 2533, which is useful for altitude ranges from -2 to 20 km (from the troposphere to lower stratosphere)[27]. This model is used to calculate important physical quantities, namely the air temperature T, air density ρ, Mach number M and dynamic pressure $\bar{q}$. The first step in using the ISO 2533 model is to calculate the geopotential height H_G, which is necessary for the calculation of the air temperature, static pressure and air density.

$$H_G = \frac{r_E \cdot h}{r_E + h} \tag{3.31}$$

Following expressions define the above mentioned physical quantities for geopotential heights from -2 to 11 km:

$$T = (1 + \gamma_{TR} \cdot \frac{H_G}{T_S}) \cdot T_S \tag{3.32}$$

$$p_{stat} = (1 + \gamma_{TR} \cdot \frac{H_G}{T_S})^{\frac{n_{TR}}{n_{TR}-1}} \cdot p_S \tag{3.33}$$

$$\rho = (1 + \gamma_{TR} \cdot \frac{H_G}{T_S})^{\frac{1}{n_{TR}-1}} \cdot \rho_S \tag{3.34}$$

Table 3.1: Atmospheric constants.

Name	Nomenclature	Value	Units
Sea Level Temperature	T_S	288.15	[K]
Sea Level Density	ρ_S	1.225	$[kg \cdot m^{-3}]$
Sea Level Pressure	p_S	1.013×10^5	$[Pa]$
Troposphere constant	n_{TR}	1.235	[1]
Lapse Rate	γ_{TR}	-6.5×10^{-3}	$[K \cdot m^{-1}]$
11 Km Temperature	T_{11}	216.65	[K]
11 Km Density	ρ_{11}	0.364	$[kg \cdot m^{-3}]$
11 Km Pressure	p_{11}	2.263×10^4	$[Pa]$
Ideal Gas Constant	R	287.05	$[J \cdot kg^{-1} K^{-1}]$
Adiabatic index	κ	1.41	[1]

The isothermal character of the stratosphere higher layers leads to different modified for temperature, static pressure and air density computation for altitudes between 11 and 20 km. Constants for both atmospheric layers are given in Table 3.1.

$$T = T_{11} \tag{3.35}$$

$$p_{stat} = p_{11} \cdot e^{-\frac{g_0}{R \cdot T_{11}} \cdot (H_G - 11000)} \tag{3.36}$$

$$\rho = \rho_{11} \cdot e^{-\frac{g_0}{R \cdot T_{11}} \cdot (H_G - 11000)} \tag{3.37}$$

Finally, with the availability for the air density and airspeed, it is possible to define the dynamic pressure and Mach number essential for expressing aerodynamic forces and moments.

$$\bar{q} = \frac{1}{2} \cdot \rho \cdot V \tag{3.38}$$

$$M = \frac{V}{\sqrt{\kappa \cdot R \cdot T}} \tag{3.39}$$

3.5.1 *Continuous Atmospheric Turbulence Model*

The continuous atmospheric turbulence model as described in this thesis was taken from the standard MIL-HDBK-1797 [8]. The model estimates continuous turbulence contributions to aircraft translational and rotational velocities based on the aircraft altitude, velocity, attitude and user setting of wind speed at 20ft altitude (low altitude model) supplemented by the probability of exceedance coefficient (high altitude model). The user may adjust parameters according to requested turbulence severity. Table 3.2 shows parameter settings for 3 levels of turbulence severity: light, moderate and severe.

Table 3.2: Severity parameters for high and low altitude conditions turbulence models.

Severity	**Wind velocity at 20 ft [kts]**	**Probability of exceedance [1]**
Light	15	10^{-2}
Moderate	30	10^{-3}
Severe	45	10^{-5}

3.5.1.1 *Forming Filters*

Equations 3.40-3.45 describe linear filters which process white noise on input and generate transtational and rotational velocities affecting the aircraft state. Linear filter parameters are adjusted with respect to scale lengths L_u, L_v, L_w, turbulence intensities $\sigma_u, \sigma_v, \sigma_w$, aircraft airspeed V and altitude h. Filter structure is identical for low and high altitude conditions. Following subsection describes differences in scale lengths and turbulence intensities. Parameter b_w represents the aircraft's wing span [8].

$$F_u(s) = \sigma_u\sqrt{\frac{2L_u}{\pi V}}\cdot\frac{1}{1+\frac{L_u}{V}s} \tag{3.40}$$

$$F_v(s) = \sigma_v\sqrt{\frac{L_v}{\pi V}}\cdot\frac{1+\frac{\sqrt{3}L_v}{V}s}{(1+\frac{L_v}{V}s)^2} \tag{3.41}$$

$$F_w(s) = \sigma_w\sqrt{\frac{L_w}{\pi V}}\cdot\frac{1+\frac{\sqrt{3}L_w}{V}}{(1+\frac{L_w}{V}s)^2} \tag{3.42}$$

$$F_p(s) = \sigma_w\sqrt{\frac{0.8}{V}}\cdot\frac{(\frac{\pi}{4b_w})^{1/6}}{L_w^{1/3}(1+(\frac{4b_w}{\pi V})s)} \tag{3.43}$$

$$F_q(s) = \frac{\pm\frac{s}{V}}{1+(\frac{4b_w}{\pi V})s}\cdot F_w(s) \tag{3.44}$$

$$F_r(s) = \frac{\pm\frac{s}{V}}{1+(\frac{3b_w}{\pi V})s}\cdot F_v(s) \tag{3.45}$$

3.5.1.2 *Low Altitude Model*

The low altitude model describes scale lengths and turbulence intensities for altitudes below 1000 ft. Scale lengths are affected only by the aircraft altitude, while turbulence intensities are influenced by wind speed W_{20} at 20ft above the ground. The velocity vector orientation in low altitude model is defined in the BFF [8].

$$\begin{aligned} L_u &= L_v = \frac{h}{(0.177 + 0.000823h)^{1.2}} && (3.46) \\ L_w &= h && (3.47) \\ \sigma_w &= 0.1W_{20} && (3.48) \\ \sigma_u &= \sigma_v = \frac{\sigma_w}{(0.177 + 0.000823h)^{0.4}} && (3.49) \end{aligned}$$

3.5.1.3 *Medium/High Altitude Model*

The high altitude model describes turbulence behavior above 2000 ft. The scale lengths are constant as shown in equation 3.50, and turbulence intensities are defined by a 2D lookup table, the graphical representation of which is shown in Figure 3.4. Inputs to the lookup table are the aircraft altitude and the probability of exceedance, set by the user according to requested turbulence severity. The velocity vector of the high altitude model is defined in BFF.

$$L_u = L_v = L_w = 1750\text{ft} \qquad (3.50)$$

$$\sigma_u = \sigma_v = \sigma_w \qquad (3.51)$$

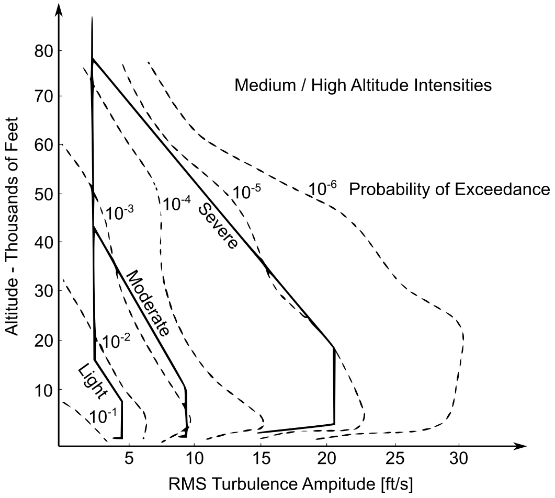

Figure 3.4: Continuous turbulence intensities based on the probability of exceedance. Source [8]

The medium altitude velocities and angular rates between 1000 ft and 2000 ft are determined as a linear interpolation between low and high altitude results and are expressed in the BFF axis frame [8].

3.5.1.4 *Turbulence Model Structure*

The inputs to the turbulence model described by a block diagram in Figure 3.5 are the geodetic altitude h, Euler angles ϕ, θ, ψ, airspeed V, wind speed at 20 ft above ground W_{20} and the probability of exceedance. Outputs that influence the aircraft simulation model are turbulence induced velocities and angular rates in BFF. The turbulence model contains three main subsystems, as shown in Figure 3.5, the Low Altitude Model, the High Altitude Model, and the function for assembling the turbulence contributions. The white noise generator block computes turbulence intensities and scale lengths. The Turbulence Filter blocks include implementation of linear filters from equations 3.40-3.45.

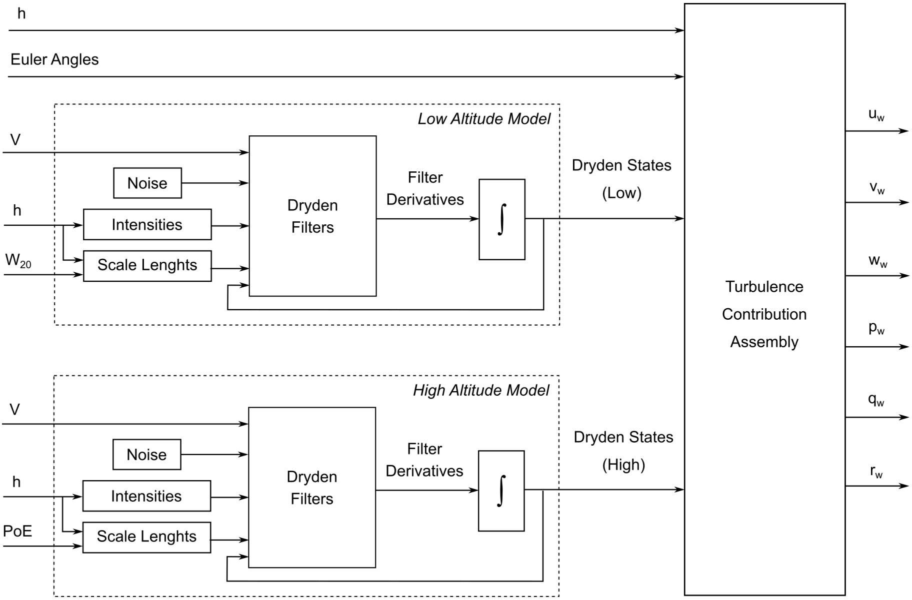

Figure 3.5: Continuous atmospheric turbulence model.

3.6 AERODYNAMIC MODEL

Aerodynamic forces and moments are influenced by the shape of the aircraft and its configuration. Equations 3.52 and 3.53 introduce aerodynamic forces and moments as functions of the mean aerodynamic chord $\bar{c}$, wing area S, wingspan b_w, air density ρ, airspeed V, and aerodynamic force and moment coefficients of the modeled aircraft [36].

$$\begin{bmatrix} D \\ Q \\ L \end{bmatrix} = \underbrace{\frac{1}{2}\rho V^2}_{\bar{q}} S \begin{bmatrix} C_D \\ C_Q \\ C_L \end{bmatrix} \tag{3.52}$$

$$\begin{bmatrix} L_A \\ M_A \\ N_A \end{bmatrix} = \underbrace{\frac{1}{2}\rho V^2}_{\bar{q}} S \begin{bmatrix} b_w & 0 & 0 \\ 0 & \bar{c} & 0 \\ 0 & 0 & b_w \end{bmatrix} \begin{bmatrix} C_l \\ C_m \\ C_n \end{bmatrix} \tag{3.53}$$

Applicable drag C_D, side-force C_Q and lift C_L coefficients, together with the roll C_l, pitch C_m and yaw C_n moment coefficients are defined by the following set of equations [30, 50].

$$C_D = C_{D_0} + C_{D_\alpha}\alpha + C_{D_{\dot{\alpha}}}\frac{\dot{\alpha}\bar{c}}{2V} + C_{D_q}\frac{q\bar{c}}{2V} + C_{D_{\delta_e}}\delta_e \tag{3.54}$$

$$C_Q = C_{Q_\beta}\beta + C_{Q_{\dot{\beta}}}\frac{\dot{\beta}b_w}{2V} + C_{Q_p}\frac{pb_w}{2V} + C_{Q_r}\frac{rb_w}{2V} + C_{Q_{\delta_a}}\delta_a + C_{Q_{\delta_r}}\delta_r \tag{3.55}$$

$$C_L = C_{L_0} + C_{L_\alpha}\alpha + C_{L_{\dot{\alpha}}}\frac{\dot{\alpha}\bar{c}}{2V} + C_{L_q}\frac{q\bar{c}}{2V} + C_{L_{\delta_e}}\delta_e \tag{3.56}$$

$$C_l = C_{l_\beta}\beta + C_{l_{\dot{\beta}}}\frac{\dot{\beta}b_w}{2V} + C_{l_p}\frac{pb_w}{2V} + C_{l_r}\frac{rb_w}{2V} + C_{l_{\delta_a}}\delta_a + C_{l_{\delta_r}}\delta_r \tag{3.57}$$

$$C_m = C_{m_0} + C_{m_\alpha}\alpha + C_{m_{\dot{\alpha}}}\frac{\dot{\alpha}\bar{c}}{2V} + C_{m_q}\frac{q\bar{c}}{2V} + C_{m_{\delta_e}}\delta_e \tag{3.58}$$

$$C_n = C_{n_\beta}\beta + C_{n_{\dot{\beta}}}\frac{\dot{\beta}b_w}{2V} + C_{n_p}\frac{pb_w}{2V} + C_{n_r}\frac{rb_w}{2V} + C_{n_{\delta_a}}\delta_a + C_{n_{\delta_r}}\delta_r \tag{3.59}$$

3.7 PLANT MODEL

The plant model is made of a combination of the aircraft and the actuator state-space model connected via control surface deflections. The output of the plant is a combination of the already defined state vector of the longitudinal or lateral-directional aircraft model and the actuator state as defined by the equation 3.60

$$x_{pl} = [x_{lat/lon}, x_{act}]^T \tag{3.60}$$

The plant system for a longitudinal and lateral-directional motion can be defined by equations 3.61 and 3.62.

$$\dot{x}_{pl} = \underbrace{\begin{bmatrix} A_{lat/lon} & B_{lat/lon}C_{act} \\ 0^{4\times5} & A_{act} \end{bmatrix}}_{A_{pl}} x_{pl} + \underbrace{\begin{bmatrix} 0^{5\times2} \\ B_{act} \end{bmatrix}}_{B_{pl}} u_{act} \tag{3.61}$$

$$y_{pl} = \underbrace{\begin{bmatrix} 1 & 0 \end{bmatrix}}_{C_{pl}} \begin{bmatrix} x_{lon/lat} \\ x_{act} \end{bmatrix} \tag{3.62}$$

When assigning equations 2.30, 2.31, 3.21, 3.22 to the equation 3.61 we get the plant dynamic matrix $A_{pl\,lon}$ expressed by the equation 3.63 and input matrix $B_{pl\,lon}$ shown in equation 3.64.

$$A_{pl\,lon} =$$

$$\begin{bmatrix} X_V & X_\alpha & X_q & -g\cos\gamma_0 & X_h & 0 & X_{\delta_T} & 0 & X_{\delta_e} \\ Z_V & Z_\alpha & Z_q & -\frac{g}{V_0}\cos\gamma_0 & Z_h & 0 & Z_{\delta_T} & 0 & Z_{\delta_e} \\ 0 & M_\alpha & 0 & M_q & M_h & 0 & M_{\delta_T} & 0 & M_{\delta_e} \\ -Z_V & -Z_\alpha & -Z_q & +\frac{g}{V_0}\cos\gamma_0 & -Z_h & 0 & 0 & 0 & 0 \\ \sin\gamma_0 & 0 & 0 & -V_0\cos\gamma_0 & 0 & 0 & 0 & 0 & 0 \\ 0 & 0 & 0 & 0 & 0 & -2\zeta_{\delta_T}\omega_{\delta_T} & -\omega^2_{\delta_T} & 0 & 0 \\ 0 & 0 & 0 & 0 & 0 & 1 & 0 & 0 & 0 \\ 0 & 0 & 0 & 0 & 0 & 0 & 0 & -2\zeta_{\delta_e}\omega_{\delta_e} & -\omega^2_{\delta_e} \\ 0 & 0 & 0 & 0 & 0 & 0 & 0 & 1 & 0 \end{bmatrix} \tag{3.63}$$

$$B_{pl\,lon} = \begin{bmatrix} 0 & 0 \\ 0 & 0 \\ 0 & 0 \\ 0 & 0 \\ 0 & 0 \\ \omega^2_{\delta_T} & 0 \\ 0 & 0 \\ 0 & \omega^2_{\delta_e} \\ 0 & 0 \end{bmatrix} \tag{3.64}$$

The dynamic matrix of lateral-directional plant model is shown in equation 3.65. Similarly, as the input matrix of longitudinal plant model, we can describe the input matrix of the lateral-directional plant model by equation 3.66

$$A_{pl\,lat} = \begin{bmatrix} Y_\beta & \frac{g}{V_0} & 0 & Y_p + s(\alpha_0) & Y_r - c(\alpha_0) & 0 & Y_{\delta_a} & 0 & Y_{\delta_r} \\ 0 & 0 & 0 & 1 & t(\theta_0) & 0 & 0 & 0 & 0 \\ 0 & 0 & 0 & 0 & \frac{1}{c(\theta_0)} & 0 & 0 & 0 & 0 \\ L_\beta & 0 & 0 & L_p & L_r & 0 & L_{\delta_a} & 0 & L_{\delta_r} \\ N_\beta & 0 & 0 & N_p & N_r & 0 & N_{\delta_a} & 0 & N_{\delta_r} \\ 0 & 0 & 0 & 0 & 0 & -2\zeta_{\delta_a}\omega_{\delta_a} & -\omega_{\delta_a}^2 & 0 & 0 \\ 0 & 0 & 0 & 0 & 0 & 1 & 0 & 0 & 0 \\ 0 & 0 & 0 & 0 & 0 & 0 & 0 & -2\zeta_{\delta_r}\omega_{\delta_r} & -\omega_{\delta_r}^2 \\ 0 & 0 & 0 & 0 & 0 & 0 & 0 & 1 & 0 \end{bmatrix} \quad (3.65)$$

$$B_{pl\,lat} = \begin{bmatrix} 0 & 0 \\ 0 & 0 \\ 0 & 0 \\ 0 & 0 \\ 0 & 0 \\ \omega_{\delta_a}^2 & 0 \\ 0 & 0 \\ 0 & \omega_{\delta_r}^2 \\ 0 & 0 \end{bmatrix} \quad (3.66)$$

Both dynamic and input matrices of longitudinal and lateral-directional plant models contain information about the aircraft and actuator dynamics. Equation 3.67 describes the output matrix, which is the same for the longitudinal, as well as lateral-directional plant model. The plant model is shown in a form in which it will be later utilized in the sections dedicated to the FCS design process.

$$C_{pl} = \begin{bmatrix} 1 & 0 & 0 & 0 & 0 & 0 & 0 & 0 & 0 \\ 0 & 1 & 0 & 0 & 0 & 0 & 0 & 0 & 0 \\ 0 & 0 & 1 & 0 & 0 & 0 & 0 & 0 & 0 \\ 0 & 0 & 0 & 1 & 0 & 0 & 0 & 0 & 0 \\ 0 & 0 & 0 & 0 & 1 & 0 & 0 & 0 & 0 \end{bmatrix} \quad (3.67)$$

4

PARAMETER ESTIMATION

The process of building an aircraft mathematical model from flight testing campaigns generally relies on System Identification techniques. The aim of this chapter is introduce the aerodynamic model parameter estimation algorithms. There are two main approaches to creating models. The first one is called the mathematical modeling and is based on the knowledge of laws of physics used for the description of system dynamics. This approach is rather analytical. The other approach uses the system's input-output data collected during test campaigns. This approach is rather experimental. The analytical approach has limited use in modeling systems with complex structure and unknown parameters. At this point, the parameter estimation approach on experimental data needs to be used. The mathematical models obtained through identification have following features:

- It is relatively easy to create them, but their validity can be limited to the surroundings of a certain working point.
- Mathematical models created via identification usually do not have true physical meaning.
- Assistance of domain expert is usually necessary during the process of the mathematical model identification.

The expert opinion about choosing the right model structure or selecting and preprocessing the correct input-output data for parameter estimation can be a better strategy than performing the trial and error process of choosing the right model structure and data set.

The motivation for creating mathematical models can be driven from the desire of better understanding the modeled systems. An identified mathematical model of an aircraft can be employed either in the process of control system design or for creating high fidelity flight simulators. The identified aircraft model can be used for a baseline FCS design and can also serve as a reference model in the adaptive flight control design , which will be introduced in the subsequent chapters. Figure 4.1 describes a general aircraft parameter estimation process using the input-output data, a priory model values and selected model structure.

Following paragraphs will introduce the basic aerodynamic model structure used in the parameter estimation along with the Equation Error Method estimation technique, which will be explained later. The estimation algorithms presented in this chapter are inspired by [28, 30]. The interested reader is referred to [11, 14, 37, 40] for more in-depth insight into system identification and parameter estimation.

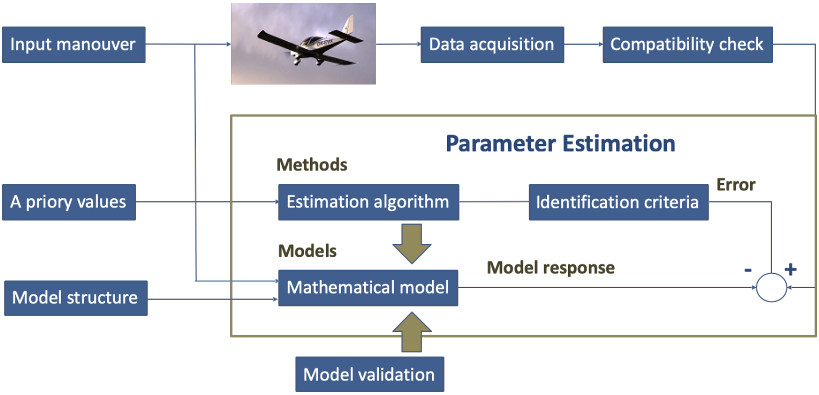

Figure 4.1: System identification process.

4.1 MODEL FOR PARAMETER ESTIMATION

The aircraft model used for parameter estimation describes contains a structure made of force and moment coefficients. Equations 4.1 - 4.6 show a sample model structure that to be used for actual parameter estimation.

$$\begin{aligned}
C_D &= C_{D_0} + C_{D_\alpha}\alpha + C_{D_{\delta_e}}\delta_e && (4.1)\\
C_Y &= C_{Y_0} + C_{Y_\beta}\beta + C_{Y_{\delta_r}}\delta_r && (4.2)\\
C_L &= C_{L_0} + C_{L_0}\alpha + C_{L_{\delta_e}}\delta_e && (4.3)\\
C_l &= C_{l_0} + C_{l_\beta}\beta + C_{l_{\delta_a}}\delta_a + C_{l_{\delta_r}}\delta_r + C_{l_p}\frac{pb_w}{2V} + C_{l_r}\frac{rb_w}{2V} && (4.4)\\
C_m &= C_{m_0} + C_{m_\alpha}\alpha + C_{m_{\delta_e}}\delta_e + C_{m_q}\frac{q\bar{c}}{2V} && (4.5)\\
C_n &= C_{n_0} + C_{n_\beta}\beta + C_{n_{\delta_a}}\delta_a + C_{n_{\delta_r}}\delta_r + C_{n_p}\frac{pb_w}{2V} + C_{n_r}\frac{rb_w}{2V} && (4.6)
\end{aligned}$$

The model can be described in a simplified form by equation 4.7.

$$z = X\theta_P + \nu \qquad (4.7)$$

where the parameters to be estimated are formed in the vector θ_P. An example of the parameter vector for a roll moment coefficient C_l is shown in equation 4.8.

$$\theta_P = [C_{l_0}, C_{l_\beta}, C_{l_{\delta_a}}, C_{l_{\delta_r}}, C_{l_p}, C_{l_r}]^T \qquad (4.8)$$

The vector of measured states, called regressors, of the roll moment coefficient C_l is formed in equation 4.9.

$$X = [1, \beta, \delta_a, \delta_r, \frac{pb_w}{2V_0}, \frac{rb_w}{2V_0}] \qquad (4.9)$$

The vector of the so called measurements z that forms left side of equation 4.7, is for the roll moment coefficient example expressed by equation 4.10.

$$z = [C_l(1), C_l(2), \ldots, C_l(N)]^T \tag{4.10}$$

Parameter N represents the number of measured data points used for parameter estimation. Since the data contains the measured noise and errors, and the model itself is only an approximation, it is suitable to define the vector of equation errors ν that is expressed by equation 4.11

$$\nu = [\nu(1), \nu(2), \ldots, \nu(N)]^T \tag{4.11}$$

The dimensionless force and moment coefficients, expressed in the equation 4.10, are computed from variables measured during the flight experiment with using the knowledge of the equations of motion and laws of physics. Forces coefficients in BFF are computed using the acceleration measurements and thrust estimates.

$$C_X = \frac{ma_x - T}{\bar{q}S} \tag{4.12}$$

$$C_Y = \frac{ma_y}{\bar{q}S} \tag{4.13}$$

$$C_Z = \frac{ma_z}{\bar{q}S} \tag{4.14}$$

These coefficients are converted in the next step using rotation about the measured angle of attack to the stability axis frame, which is often used for expressing the aerodynamic force and moment coefficients. This rotation does not affect the side-force coefficient C_Y, which remains the same.

$$C_D = -C_X \cos(\alpha) - C_Z \sin(\alpha) \tag{4.15}$$

$$C_L = -C_Z \cos(\alpha) + C_X \sin(\alpha) \tag{4.16}$$

Moment coefficient computations are based on the moment equations of motion and the knowledge of moments of inertia and rotational accelerations that are usually computed as a numerical derivative of angular rate signals.

$$C_l = \frac{I_x}{\bar{q}Sb_w}\left[\dot{p} - \frac{I_{xz}}{I_x}(pq + \dot{r}) + \frac{(I_z - I_y)}{I_x}qr\right] \tag{4.17}$$

$$C_m = \frac{I_y}{\bar{q}S\bar{c}}\left[\dot{q} + \frac{(I_x - I_z)}{I_y}pr + \frac{I_x z}{I_y}(p^2 - r^2)\right] \tag{4.18}$$

$$C_n = \frac{I_z}{\bar{q}Sb_w}\left[\dot{r} - \frac{I_{xz}}{I_z}(\dot{p} - qr) + \frac{(I_y - I_x)}{I_z}pq\right] \tag{4.19}$$

4.2 EQUATION ERROR METHOD

In its most basic form, the Equation Error Method becomes the parameter estimator based on the minimization of the sum of squared differences, i.e., the least-squares estimator. This type of estimator requires a type of model that is linear in parameters. The advantages of the least-squares estimator are simple implementation and low computational complexity. The aerodynamic force and moment coefficients equations 4.1-4.6 fulfill the condition of linearity in parameter fits to the required model structure expressed in equation 4.10. As stated above, the least square estimator minimizes the sum of squared differences defined by criterion $J(\theta_P)$ within the equation 4.20.

$$\begin{aligned} J(\theta_P) &= \frac{1}{2}(z - X\theta_P)^T(z - X\theta_P) \\ &= \frac{1}{2}[\theta_P^T X^T X\theta_P - \theta_P^T X^T z - z^T X\theta_P + z^T z] \end{aligned} \tag{4.20}$$

The vector of parameters θ_P that minimizes quadratic criterion $J(\theta_P)$ is defined by equation 4.21

$$\frac{dJ(\theta_P)}{d\theta_P} = -z^T X + \theta_P^T(X^T X) = 0 \tag{4.21}$$

and by expressing the parameter vector θ_P form equation 4.21 its least square estimate can be expressed by equation 4.22.

$$\hat{\theta}_P = (X^T X)^{-1} X^T z \tag{4.22}$$

The analysis of parameter estimate given by equation 4.22 can be done assuming that the regressor X is without error, and the noise within the measurement z is white and Gaussian. In that case, the output estimate $\hat{y}$ can be expressed using equation 4.23, which leads to computation of measurement variance σ^2 defined by equation 4.24. Resulting estimate covariance matrix P_{ij} and standard deviation s, which is the squared root of estimate covariance, can be expressed using equations 4.25 and 4.26.

$$\hat{y} = X\hat{\theta}_P \tag{4.23}$$

$$\hat{\sigma}^2 = \frac{(z - \hat{y})^T(z - \hat{y})}{N - n_p} \tag{4.24}$$

$$\begin{aligned} \mathrm{cov}(\hat{\theta}_P) &= E[(\hat{\theta}_P - \theta_P)(\hat{\theta}_P - \theta_P)^T] = \hat{\sigma}^2(X^T X)^{-1} \\ &= [P_{ij}] \text{ where } i, j = 1, 2, \ldots, n_p \end{aligned} \tag{4.25}$$

$$s(\hat{\theta}_{P_j}) = \sqrt{P_{jj}} \tag{4.26}$$

4.3 STATE ESTIMATION TECHNIQUES

The state estimation is a technique that computes the state of a dynamic system from the measured variables. The use-cases of state estimation, which is widely used throughout the control system design, include the signal noise suppression, signal reconstruction (in aerospace applications known as flight path reconstruction) and data fusion that improves the accuracy of the state estimate by combining different sensors, widely used in navigation systems as Global Positioning System (GPS) or robotics application. One of the most utilized techniques for state estimation, which will be described in this section, is the Kalman filter. The Kalman filter was co-invented by Rudolph Kalman in 1958 during his work on the Apollo project navigation computer and became quickly popular, especially among the engineering community. The reason was its transparency. In contrast to the Wiener filter, which is based on frequency description and spectral factorization, the Kalman filter operates in the time domain and with system state variables. More details about the state estimation topics can be found in [1, 7, 29]. Kalman filter is a linear optimal state estimator in the means of minimal variance, and its basic working principle is the calculation of weighted average between the measured and predicted state, where the weight (Kalman gain) depends on the uncertainty of the measurement, the higher the uncertainty, the lower the weight. It can be expressed by a general equation 4.27

$$x_{estimated} = x_{predicted} + K \cdot (z_{measured} - z_{predicted}) \tag{4.27}$$

The motivation of using state estimation within the task of parameter estimation is that the result of parameter estimation, i.e., the identified model is directly influenced by the quality of input-output data used. If the data is noisy and biased or some necessary variables are missing, it is highly likely that the parameter estimator's performance will be poor. In other words, if there is garbage at the input to the parameter estimator, there will be garbage at the output as well. Another utilization of state estimation techniques is related to the control system design. The state estimator, namely the Kalman filter, is an integral part of the LQG control technique, which will be researched in detail in Chapter 5. The LQG control approach combines the Kalman filter with the state feedback control. The Kalman filter assumes stochastic, affine, linear and time-variant system in a form defined by equations 4.28 and 4.29.

$$\dot{x}(t) = A(t)x(t) + B(t)u(t) + G(t)w(t) \quad x(t_0) = x_0 \tag{4.28}$$

$$z(t) = H(t)x(t) + D(t)u(t) + v(t) \quad t = t_i, \quad i = 1, 2, \ldots \tag{4.29}$$

Matrices A, B, G, H, D are assumed to be known and possibly time-varying. The variable $w(t)$ is the process continuous white noise and $v(t)$ is the measurement white noise. The noise characteristics, namely the process noise mean $E[w(t)]$, process noise covariance $E\left[w(t)w(t)^T\right]$, measurement noise mean $E[v(t)]$ and measurement noise covariance $E\left[v(t)v(t)^T\right]$ are introduced in equations 4.30-4.33

$$E[w(t)] = 0 \tag{4.30}$$

$$E\left[w(t)w(t)^T\right] = Q(t) \tag{4.31}$$

$$E[v(t)] = 0 \tag{4.32}$$

$$E\left[v(t)v(t)^T\right] = R(t) \tag{4.33}$$

Before the definition of the Kalman filter algorithm it is necessary to discretize the continuous system expressed in equations 4.28 and 4.29, which results in a following discrete linear system described by equations 4.34 and 4.35.

$$\dot{x}_{k+1} = \Phi_{k+1}x_{k+1} + \Psi_{k+1}u_{k+1} + \Gamma_{k+1}w_{k+1} \tag{4.34}$$

$$z_{k+1} = H_{k+1}x_{k+1} + D_{k+1}u_{k+1} + v_{k+1} \tag{4.35}$$

Table 4.1: Kalman filter variables definition.

Description	Variable
Current real system state	x_k
One step ahead real system state	x_{k+1}
Current optimal estimated system state	$\hat{x}_{k,k}$
One step ahead state prediction	$\hat{x}_{k+1,k}$
One step ahead optimal state estimation	$\hat{x}_{k+1,k+1}$

Variable Φ_{k+1} represents the system transition matrix, Ψ_{k+1} is the input distribution matrix, and Γ_{k+1} defines the noise input matrix. Table 4.1 defines some variables that will be used throughout the Kalman filter description.

The first step in the Kalman filter definition is expressing the one step ahead state prediction described by equation 4.36, which is followed by the computation of the state prediction error covariance matrix expressed by equation 4.37.

$$\hat{x}_{k+1,k} = \Phi_{k+1,k}\hat{x}_k + \Psi_{k+1,k}u_k, \quad \hat{x}_{0,0} = \hat{x}_0 \tag{4.36}$$

$$P_{k+1,k} = \Phi_k P_{k,k} \Phi_k^T + \Gamma_{k+1,k} Q_d \Gamma_{k+1,k}^T, \quad P_{0,0} = P_0 \tag{4.37}$$

The subsequent step is the Kalman gain calculation, which represents the relative weight of difference between the measurement and estimate.

$$K_{k+1} = P_{k+1,k} H_{k+1}^T (H_{k+1} P_{k+1,k} H_{k+1}^T + R_{k+1})^{-1} \tag{4.38}$$

Afterwards the measurement update of the state estimate is introduced in equation 4.39.

$$\hat{x}_{k+1,k+1} = \hat{x}_{k+1,k} + K_{k+1} \underbrace{(z_{k+1} - H_{k+1}\hat{x}_{k+1,k})}_{\text{Measurement error}} \tag{4.39}$$

As stated in equation 4.27 the optimal estimate $\hat{x}_{k+1,k+1}$ is a combination of the biased state estimate $\hat{x}_{k+1,k}$ and the estimated measurement error scaled by the Kalman gain K_{k+1}. The state estimation error covariance matrix is computed at the end of the recursive cycle using equation 4.40. In other words, the sample covariance matrix $P_{k+1,k+1}$ can be expressed in terms of the old covariance matrix $P_{k+1,k}$.

$$P_{k+1,k+1} = (I - K_{k+1} H_{k+1}) P_{k+1,k} \tag{4.40}$$

The Kalman filter described by equations 4.36-4.40 is intentionally introduced in its recursive form as it is the most appropriate way for easy and straightforward implementation. After performing the last step, that is the computation of the state estimation error covariance matrix, the recursive cycle starts again from the equation 4.36, therefore it is referred to as a state prediction computation.

To determine the noise covariance matrices Q and R, it is possible to use the knowledge of the sensor calibration process. If the system input vector is defined by equation 4.41, then each input has a standard deviation defined by vector Σ_u specified in equation 4.42.

$$u = [u_1, \dots, u_n]^T \tag{4.41}$$

$$\Sigma_u = [\sigma_{u1}, \dots, \sigma_{un}] \tag{4.42}$$

Equivalently if the measurement vector z is expressed by equation 4.43, then the corresponding standard deviation vector Σ_z is defined by equation 4.44

$$z = [z_1, \dots, z_m] \tag{4.43}$$

$$\Sigma_z = [\sigma_{z1}, \dots, \sigma_{zm}] \tag{4.44}$$

The noise covariance matrices Q and R can be defined in the form of a diagonal matrix containing the squared input and measurement standard deviations.

$$Q = \begin{bmatrix} \sigma_{u1}^2 & 0 & 0 \\ 0 & \ddots & 0 \\ 0 & 0 & \sigma_{un} \end{bmatrix}, \quad R = \begin{bmatrix} \sigma_{z1}^2 & 0 & 0 \\ 0 & \ddots & 0 \\ 0 & 0 & \sigma_{zm} \end{bmatrix} \tag{4.45}$$

Considerations in the following list need to be made when implementing the ordinary linear Kalman filter.

- System assumed in the state estimator needs to be linear.
- System model (matrices A, B, H, D) needs to be known.
- Noise covariance matrices Q, R need to be known.
- The R matrix should be based on sensor noise measurements.
- Stochastic input noise represents both sensor noise and model uncertainties.
- The initial guess of the covariance matrix P_0 should be selected large for unknown initial state error.
- Initial state estimate $\hat{x}_0$ can be selected arbitrarily.
- The system has to be fully observable to guarantee the Kalman filter convergence.

As stated above, the ordinary Kalman filter can only estimate the state of a linear system. However, in practice, the system and measurement equations can become nonlinear. In that case, the Extended Kalman Filter (EKF) that linearizes the system and measurement equation around their nominal values can be used. However, when using the EKF, the state estimates are no longer guaranteed to converge to an optimally estimated state. Other versions of the Kalman filter, as the Iterated EKF or Unscented Kalman Filter (UKF), only improve the convergence of the state estimate. Similarly to the case of EKF they do not guarantee an optimal state estimate.

5

CONTROL SYSTEM SYNTHESIS

This chapter contains the theoretical background and practical aspects of modern Flight Control System (FCS) design.

The LQR is a state feedback control method known to provide an excellent design robustness capability. However, two deficiencies emerge when considering the LQR implementation into an automatic flight control system. The first implementation deficiency of the LQR method is that it is a state feedback approach requiring all system states to be measurable. The second implication is the fact that this method is unable to provide sufficient noise attenuation. In order to mitigate the previously introduced challenges, an optimal estimation technique (Kalman filter), along with optimal regulation, can be used to create an output feedback strategy known as LQG. In other words, the LQG control is a combination of Kalman filter and LQR. Even though the LQG provides reduced tracking performance and stability margins when compared to LQR, its robustness can be regained by employing the so-called Loop Transfer Recovery (LTR) technique. The cost for the recovery includes an obvious trade-off between the controller's stability margins and its noise attenuation capability. The linear-quadratic control topic is described in more detail in the following references [4, 13, 32, 44, 52].

5.1 LQR-BASED FLIGHT CONTROL SYSTEM SYNTHESIS

Since controlling an aircraft requires command tracking capabilities, e.g., maintaining specified airspeed, altitude or heading, the basic LQR algorithm has to be augmented with an integral error dynamics, which guarantees the steady-state error minimization of the controlled variables. The LQR based FCS design requires availability of a linear state-space system. Based on the assumption from Chapter 2, that a linearized aircraft model can be decoupled into longitudinal and lateral-directional motion models, the FCS for both models will be researched individually. Figure 5.1 shows the design scheme for an LQR based FCS. It contains three main subsystems, namely the Plant, which is a combination of the aircraft and actuator dynamics, the negative state feedback matrix K_{LQR}, and an Integral Error Dynamics.

The LQR might be employed assuming the full availability of the Design System state x_{DS}, yielding a control law as graphically illustrated in Figure 5.1.

$$u = -K_{LQR} \cdot x_{DS} \tag{5.1}$$

At first, the baseline controller for the longitudinal motion model will be expressed. The plant state is defined in the form of the following vector

$$x_{PL_{lon}} = [V, \alpha, q, \gamma, h, \dot{\delta}_T, \delta_T, \dot{\delta}_e, \delta_e]^T, \tag{5.2}$$

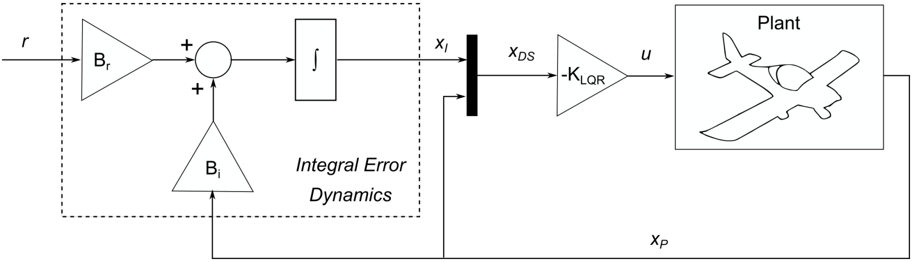

Figure 5.1: The LQR system scheme.

which is a combination of the longitudinal motion model state and the actuator model state. Selected controlled variables in the reference signal r are the commanded airspeed V_{cmd} and altitude h_{cmd}.

$$r = [V_{cmd}, h_{cmd}]^T \tag{5.3}$$

The Integral Error dynamics state vector x_{IE} contains respective airspeed and altitude errors, as introduced in equation 5.4.

$$x_{IE} = [e_V, e_h]^T \tag{5.4}$$

The Integral Error dynamics for the longitudinal motion FCS is described below by the equation 5.5.

$$\overbrace{\begin{bmatrix}\dot{e}_V\\ \dot{e}_h\end{bmatrix}}^{\dot{x}_{IE}} = \overbrace{\begin{bmatrix}0&0\\0&0\end{bmatrix}}^{A_{IE}}\overbrace{\begin{bmatrix}e_V\\ e_h\end{bmatrix}}^{x_{IE}} + \overbrace{\begin{bmatrix}-1&0&0&0&0&0&0&0&0\\0&0&0&0&-1&0&0&0&0\end{bmatrix}}^{B_{IE}} x_{PL_{lon}} + \underbrace{\begin{bmatrix}1&0\\0&1\end{bmatrix}}_{B_r}\underbrace{\begin{bmatrix}V_{cmd}\\ h_{cmd}\end{bmatrix}}_{r} \tag{5.5}$$

The system for the longitudinal FCS design is a combination of an Integral Error dynamics and a Plant model as show in equation 5.6.

$$\underbrace{\begin{bmatrix}\dot{x}_{PL_{lon}}\\ \dot{x}_{IE}\end{bmatrix}}_{\dot{x}_{DS}} = \underbrace{\begin{bmatrix}A_{PL_{lon}} & 0^{9\times 2}\\ B_{IE} & A_{IE}\end{bmatrix}}_{A_{DS}}\underbrace{\begin{bmatrix}x_{PL_{lon}}\\ x_{IE}\end{bmatrix}}_{x_{DS}} + \underbrace{\begin{bmatrix}B_{PL_{lon}}\\ 0^{2\times 1}\end{bmatrix}}_{B_{DS}} u + \begin{bmatrix}0^{9\times 2}\\ B_r\end{bmatrix} r \tag{5.6}$$

The lateral-directional plant model's state vector is composed of the sideslip β, roll ϕ and heading ψ angle, roll p and yaw r rates, the aileron δ_a and rudder δ_r deflections, and their respective rates as shown in equation 5.7.

$$x_{PL_{lat}} = [\beta, \phi, \psi, p, r, \dot{\delta}_a, \delta_a, \dot{\delta}_r, \delta_r]^T \tag{5.7}$$

The controlled variables for the lateral-directional FCS are the sideslip and heading angle commands, which define the content of the reference signal r.

$$x_{IE} = [e_\beta, e_\psi]^T \tag{5.8}$$

$$r = [\beta_{cmd}, \psi_{cmd}]^T \tag{5.9}$$

The integral error dynamics state vector x_{IE} for the lateral-directional FCS can be expressed using equation 5.10.

$$\overbrace{\begin{bmatrix}\dot{e}_\beta\\ \dot{e}_\psi\end{bmatrix}}^{\dot{x}_{IE}} = \overbrace{\begin{bmatrix}0&0\\0&0\end{bmatrix}}^{A_{IE}}\overbrace{\begin{bmatrix}e_\beta\\ e_\psi\end{bmatrix}}^{x_{IE}} + \overbrace{\begin{bmatrix}-1&0&0&0&0&0&0&0\\0&0&-1&0&0&0&0&0\end{bmatrix}}^{B_{IE}} x_{PL_{lat}} + \underbrace{\begin{bmatrix}1&0\\0&1\end{bmatrix}}_{B_r}\underbrace{\begin{bmatrix}\beta_{cmd}\\ \psi_{cmd}\end{bmatrix}}_{r} \tag{5.10}$$

Similarly to the longitudinal FCS design, the Design System used for the lateral-directional controller can be defined in the form of equation 5.11.

$$\underbrace{\begin{bmatrix}\dot{x}_{PL_{lat}}\\ \dot{x}_{IE}\end{bmatrix}}_{\dot{x}_{DS}} = \underbrace{\begin{bmatrix}A_{PL_{lat}} & 0^{9\times 2}\\ B_{IE} & A_{IE}\end{bmatrix}}_{A_{DS}}\underbrace{\begin{bmatrix}x_{PL_{lat}}\\ x_{IE}\end{bmatrix}}_{x_{DS}} + \underbrace{\begin{bmatrix}B_{PL_{lat}}\\ 0^{2\times 1}\end{bmatrix}}_{B_{DS}} u + \begin{bmatrix}0^{9\times 2}\\ B_r\end{bmatrix} r \tag{5.11}$$

The Design System defined by matrices A_{DS} and B_{DS}, from equations 5.6 and 5.6. is used for the computation of the feedback gain matrix K_{LQR}, which is then used for expressing the closed-loop system. The closed system, shown in equation 5.12, will have an identical structure for the longitudinal and the lateral-directional model.

$$\dot{x}_{cl} = \left(\begin{bmatrix}A_{PL} & 0^{9\times 2}\\ B_{IE} & A_{IE}\end{bmatrix} - \begin{bmatrix}B_{PL}\\ 0^{2\times 1}\end{bmatrix} K_{LQR}\right) x_{cl} + \begin{bmatrix}0^{9\times 2}\\ B_r\end{bmatrix} r \tag{5.12}$$

5.1.1 *LQG-based Flight Control System Synthesis*

For Linear Time Invariant (LTI) systems with normally distributed process and measurement noise, the optimal state estimator with respect to the minimal variance is the Kalman Filter [34]. The system for a LQG controller design is described by the equation 5.13.

$$\dot{x}_{DS} = A_{DS}x_{DS} + B_{DS}u_c + \begin{bmatrix}0^{9\times 2}\\ B_r\end{bmatrix} r + w_{DS} \tag{5.13}$$

Subscript DS stands for Design System, which is a combination of Plant and Integral Error dynamics. Variable w_{DS} represents the Design System's process noise. The estimator used in the LQG control design can be expressed by equations 5.14 and 5.15, which is the Kalman filter form.

$$\dot{\hat{x}}_{DS} = \hat{A}_{DS}\hat{x}_{DS} + \begin{bmatrix} 0^{9\times 2} \\ B_r \end{bmatrix} r + L_{LQG}(y_{DS} - \hat{y}_{DS}) \tag{5.14}$$

$$\hat{y}_{DS} = \hat{C}_{DS}\hat{x}_{DS} \tag{5.15}$$

Figure 5.2 shows the combination of the feedback gain matrix K_{LQR} and a Kalman Filter in a closed loop with a state-space Plant description. Variables $\hat{x}$ and $\hat{y}$ represents system's state and output estimates, while variables w and n are the process and measurement noise.

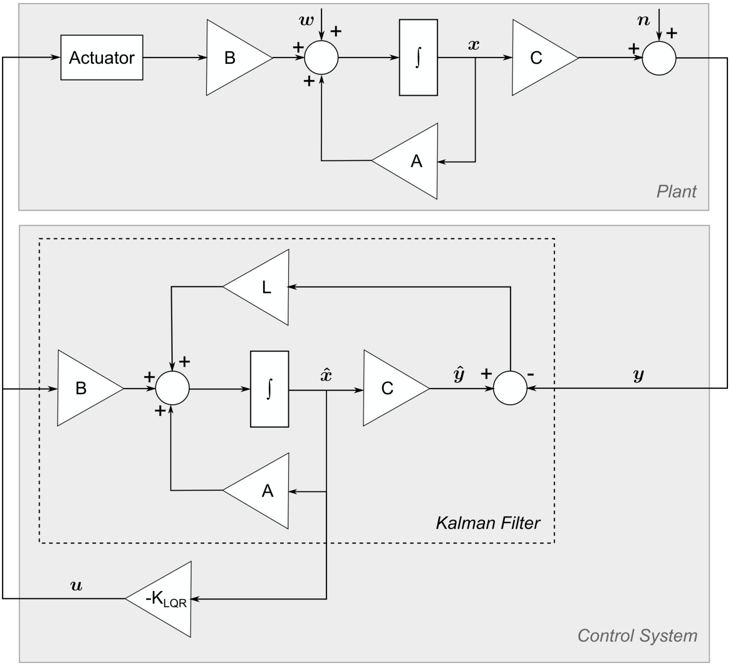

Figure 5.2: The LQG control system scheme.

The LQG closed loop system is expressed by equation 5.16.

$$\dot{x}_{cl} = \begin{bmatrix} \dot{x}_{PL} \\ \dot{x}_{IE} \\ \dot{x}_{DS} \end{bmatrix} = A_{cl}x_{cl} + \begin{bmatrix} 0^{9\times 2} \\ B_r \\ \begin{bmatrix} 0^{9\times 2} \\ B_r \end{bmatrix} \end{bmatrix} r + \begin{bmatrix} w_{DS} \\ 0^{2\times 1} \\ 0^{11\times 1} \end{bmatrix} \tag{5.16}$$

The closed-loop system state matrix A_{cl} is composed of all subsystems as the Plant, Integral Error dynamics and Kalman Filter dynamics, as introduced in the following equation 5.17 [9].

$$A_{cl} = \begin{bmatrix} A_{PL} & 0^{9\times 2} & -B_{PL}K_{LQR} \\ B_{IE} & A_{IE} & 0^{2\times 11} \\ L_{x_{PL}}C_{PL} & L_{x_{IE}} & A_{kf} \end{bmatrix}, \tag{5.17}$$

where the state matrix of the Kalman Filter A_{kf} is expressed by equation 5.18.

$$A_{kf} = \left(\begin{bmatrix} \hat{A}_{PL} & 0^{9\times 2} \\ B_{IE} & A_{IE} \end{bmatrix} - \begin{bmatrix} \hat{B}_{PL} \\ 0^{2\times 11} \end{bmatrix} K_{LQR} - L_{LQG}\hat{C}_{DS} \right) \tag{5.18}$$

5.1.2 *Loop Transfer Recovery*

A significant advantage of the LQG controller design approach lies in the possibility to estimate the missing states, i.e., so the designer doesn't need to have complete knowledge of the state vector. The next advantage is in the noise attenuation capabilities. However, the cost for these features is the system's closed-loop robustness reduction. The idea behind the Loop Transfer Recovery (LTR) technique is to modify the LQG design in order to restore the LQR closed-loop system's robustness. The modification of the LQR gains is not recommended. Instead, tuning of the Kalman filter gain is proposed as a better way to achieve the excellent robustness features of the LQR approach [47].

The LTR method parametrizes both process and measurement noise covariances utilized in the solution of the Riccati equation. The original covariances Q, R are recalculated according to the following expressions introduced in equations 5.19 and 5.20 [56].

$$Q_n = Q + \frac{\nu + 1}{\nu}\bar{B}\bar{B}^T \tag{5.19}$$

$$R_n = \frac{\nu + 1}{\nu}R \tag{5.20}$$

Matrix $\bar{B}$ is created by adding columns to matrix B.

$$\bar{B} = [BX],\ X \in^{n_x \times (n_y - n_u)} \tag{5.21}$$

The matrix X should complete the column rank of matrix B in a way such that the matrix $C\bar{B}$ is invertible and that the corresponding extended system $C(sI - A)^{-1}\bar{B}$ should be a minimum phase, which means the system and its inversion are stable. The reason for the minimum phase requirement is, the system dynamics $C(sI - A)^{-1}\bar{B}$ is inverted within the Kalman filter, and if it contains negative zeros, the closed-loop system becomes unstable. The extended Riccati equation is a combination of equation and equations 5.19, 5.20 and it is expressed in equation 5.22 [47].

$$\begin{aligned} AP_{ricc} &+ P_{ricc}A^T + Q + \bar{B}\bar{B}^T - P_{ricc}C^TR^{-1}CP_{ricc} \\ &+ \frac{1}{\nu}(\bar{B}\bar{B}^T - P_{ricc}C^TR^{-1}CP_{ricc}) = 0 \end{aligned} \tag{5.22}$$

5.2 MODEL REFERENCE ADAPTIVE CONTROL

In practice, the dynamic model used for the controller design is not fully identical to the real controlled plant due to the parametric uncertainties (e.g. differences in aerodynamic parameters). Therefore, even a robust LQR design introduced in the previous section may not provide sufficient robustness to meet the design requirements. Moreover, the design could be too conservative to provide good tracking performance, which leads to a gain adaptation controller design.

The motivation for designing the adaptive control systems is summarized in the following list [22].

- Current FCS design (LQR) assumes an exact knowledge of aircraft dynamics available through respective state-space matrices A, B, C, D.
- Covering larger part of the flight envelope (due to adaptation of control system parameters) than linear FCS, which is designed for only one point of the flight envelope.
- Current LQR based FCS design is not fault-tolerant.
- Various uncertainties can influence the aircraft model's fidelity.
- The aircraft dynamics can change due to unexpected structural or system failures.

The concept used in this work for adaptive augmentation of the LQR baseline FCS is called Model Reference Adaptive Control (MRAC). The core idea behind the MRAC design is the online modification or adaptation of controller gains considering the error between the Plant and the desired reference system. Within the so-called Direct MRAC approach, the controller gains are computed by an adaptation law in order to minimize the error between the plant and reference system response. Figure 5.3 shows the MRAC based adaptive control design concept.

The stability concept used in the MRAC design is Lyapunov's direct stability method in combination with the so-called Massachusetts Institute of Technology (MIT) rule, which creates the adaptation law basis. As this approach guarantees only the stability and not the asymptotic stability, the Barbalat's Lemma is used for proving the asymptotic stability of the error. The following subsection will introduce the Lyapunov stability concept, namely the Lyapunov direct method, that will play a critical role in the adaptive control law derivation process. The Lyapunov stability theory is well covered in references [33, 39, 43].

5.2.1 *Derivation of Adaptive Control Law*

As shown in Figure 5.3 the complete input to the plant is composed of 3 main signals, namely the baseline controller input u_{bl} provided by the LQR control system, the adaptive augmentation input u_{ad} and the model uncertainty. The adaptive augmentation's main purpose is the uncertainty suppression. The adaptive control law derivation process with LQR baseline controller is summarized in the following list [20, 23, 34]:

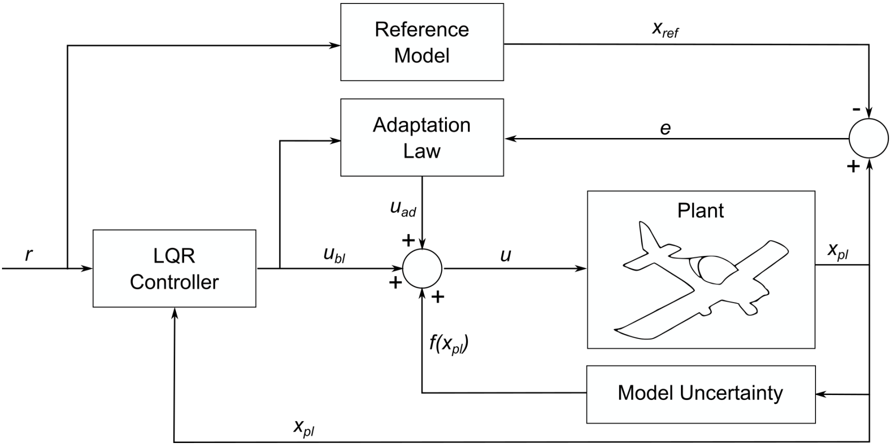

Figure 5.3: MRAC system block diagram.

1. Define the plant dynamics with model uncertainty.
2. Augment the plant dynamics with an Integral Error dynamics and create a Design System
3. Close the loop with LQR based control law.
4. Define matching conditions and the reference model for MRAC.
5. Define the control law composed of baseline controller and adaptation rule.
6. Define the tracking error between the reference state and the plant state.
7. Express error dynamics.
8. Define the Lyapunov function candidate.
9. Solve the Lyapunov equation.
10. Express the Lyapunov function derivative.
11. Form an adaptation law.

Lets consider the plant dynamics with a state-dependent matched uncertainty $f(x_{PL})$,

$$\begin{aligned} \dot{x}_{PL} &= A_{PL}x_{PL} + B_{PL}\Lambda(u + f(x_{PL})), \quad (5.23) \\ f(x_{PL}) &= \theta^T\phi(x_{PL}), \quad (5.24) \end{aligned}$$

where unknown parameter λ represents the input uncertainty. The matched uncertainty $f(x_{PL})$ is composed of an unknown parameter matrix θ and known n-dimensional regressor vector $\phi(x_{PL})$.

The combination of a Plant and an Integral Error dynamics is to be used as a system for the following MRAC design, resulting in a state-space representation shown in equation 5.28. The system is called the Design System since it is used for MRAC controller design and thus contains the subscript DS.

$$A_{DS} = \begin{bmatrix} A_{PL} & 0^{9\times 2} \\ B_{IE} & A_{IE} \end{bmatrix} \tag{5.25}$$

$$B_{DS} = \begin{bmatrix} B_{PL} \\ 0^{2\times 2} \end{bmatrix} \tag{5.26}$$

The whole open loop extended plant dynamics is expressed in equation 5.28. Its state x_{DS} is defined by equation 5.27.

$$x_{DS} = [x_{PL}, x_{IE}]^T \tag{5.27}$$

It contains the plant dynamics state x_{PL} defined by equations 5.2, 5.7 and the Integral Error dynamics state x_{IE} described in equations 5.4, 5.8 as well as the reference input r expressed by equations 5.3, 5.9.

$$\dot{x}_{DS} = A_{DS}x_{DS} + B_{DS}\Lambda(u + \theta^T\phi(x_{PL})) + B_{ref}r \tag{5.28}$$

Now we can set up the matching condition expressed by equations 5.29 and 5.30, which define the dynamics of a Reference model (subscript ref), which is to be followed by the Plant with an uncertainty.

$$A_{ref} = A_{DS} + B_{DS}\Lambda K_{LQR}^T \tag{5.29}$$

$$B_{ref} = \begin{bmatrix} 0^{9\times 2} \\ B_r \end{bmatrix} \tag{5.30}$$

The Reference model inputs are the signal commands and the output is an ideal state x_{ref}. The dynamics of the Reference model is described by equation 5.31.

$$\dot{x}_{ref} = A_{ref}x_{ref} + B_{ref}r \tag{5.31}$$

The total control input u is composed of three main components as defined by equation 5.32 namely the base-line control input u_{bl}, defined in foregoing section, and an adaptation component u_{ad}, responsible for canceling the unknown matched uncertainties $f(x_{PL})$ introduced into the Plant dynamics [34].

$$u = u_{bl} + u_{ad} + f(x_{PL}) \tag{5.32}$$

The baseline control input u_{bl} is calculated as a product of the negative LQR feedback gain K_{LQR} and the Design System state x_{DS}. The adaptation input u_{ad} is composed of an input gain matrix estimate $\hat{K}_u$ and an uncertainty gain matrix estimate $\hat{\theta}$.

$$u = \underbrace{-K_{LQR}x_{DS}}_{u_{bl}} + \underbrace{(-\hat{K}_u^T u_{bl} - \hat{\theta}^T\phi(x_{PL}))}_{u_{ad}} + \underbrace{\theta^T\phi(x_{PL})}_{f(x_{PL})} \tag{5.33}$$

To express the estimate of the previously mentioned gain matrices $\hat{K}_u$ and $\hat{\theta}$, it becomes necessary to compute the tracking error as a difference between the Design System's state and the state of the reference system, which is introduced in equation 5.34.

$$e_{tr} = x_{DS} - x_{ref} \tag{5.34}$$

Based on the equation 5.34 it is possible to define the error dynamics equation 5.35, which will in the next steps lead to the definition of a Lyapunov function $V(e_{tr}, \Delta\bar{\theta})$.

$$\dot{e}_{tr} = A_{ref} e_{tr} - B_{DS} \Lambda \Delta\bar{\theta}^T \bar{\phi} \tag{5.35}$$

Term $\bar{\theta}$ represents an extended adaptive parameter matrix and $\bar{\phi}$ is an extended regressor defined by equations 5.36 and 5.37 respectively.

$$\begin{aligned} \bar{\theta} &= [K_u, \theta] & (5.36) \\ \bar{\phi} &= [u_{bl}, \phi] & (5.37) \end{aligned}$$

The difference between the adaptive parameter matrix θ and its estimate $\hat{\theta}$ is expressed by equation 5.38 and it is necessary for the Lyapunov function $V(e_{tr}, \Delta\bar{\theta})$ computation.

$$\Delta\bar{\theta} = \bar{\theta} - \hat{\bar{\theta}} \tag{5.38}$$

In order to express the parameter update laws and to assure the closed-loop stability of error dynamics, we define the quadratic Lyapunov function $V(e_{tr}, \Delta\bar{\theta})$, known as the "kinetic energy" of the errors in the system, defined by equation 5.39.

$$V(e_{tr}, \Delta\bar{\theta}) = e_{tr}^T P_{lyap} e_{tr} + \mathrm{trace}(\Delta\bar{\theta}^T \Gamma_{\bar{\theta}}^{-1} \Delta\bar{\theta} \Lambda) \tag{5.39}$$

Matrix $\Gamma_{\bar{\theta}}$ is a symmetric positive definite and defines the learning rate of an adaptive controller and matrix P_{lyap} is the solution of Lyapunov algebraic equation introduced in equation 5.40. The Lyapunov equation solution is used as a measure to guarantee the stability of an error dynamics in a closed-loop system.

$$P_{lyap} A_{ref} + A_{ref}^T P_{lyap} = -Q \tag{5.40}$$

The solution of the equation 5.40 is employed to estimate the input and uncertainty gain matrices. In order to define the structure of the MRAC update laws, the time derivative of the above mentioned Lyapunov function $\dot{V}(e_{tr}, \Delta\bar{\bar{\theta}})$ results in equation 5.41.

$$\dot{V}(e_{tr}, \Delta\bar{\theta}) = -e_{tr}^T Q e_{tr} - 2 e_{tr}^T P_{lyap} B_{DS} \Lambda \Delta\bar{\theta}^T \bar{\phi} + 2\mathrm{trace}(\Delta\bar{\theta}^T \Gamma_{\bar{\theta}}^{-1} \dot{\hat{\theta}} \Lambda) \tag{5.41}$$

Then we apply the vector trace identity $a^T b = \mathrm{trace}(b a^T)$ to express the derivative of the Lyapunov function in a form suitable for the MRAC update laws synthesis, which results in equation 5.42. This design strategy aims to dissipate the energy and thus push the derivative of the Lyapunov function to be non-positive, which assures that the Lyapunov function will be non increasing.

$$\dot{V}(e, \Delta\bar{\theta}) = -e^T Q e + 2\mathrm{trace}(\Delta\bar{\theta}^T \{\Gamma_{\bar{\theta}}^{-1} \dot{\hat{\bar{\theta}}} - \bar{\phi} e_{tr}^T P_{lyap} B_{DS}\} \Lambda) \tag{5.42}$$

The condition of a negative semi-definite derivation of the Lyapunov function, which guarantees the stability of a closed-loop system according to Lyapunov's direct method for assessing uniform stability of nonautonomous systems described in [39], is achieved by the definition of the update law in equation 5.43.

$$\dot{\hat{\bar{\theta}}} = \Gamma_{\bar{\theta}} \bar{\phi}(u_{bl}, x_{PL}) e_{tr}^T P_{lyap} B_{DS} \tag{5.43}$$

The matrix $\Gamma_{\bar{\theta}}$ can be expressed by equation 5.44 and contains the adaptation rates for uncertainties Γ_u and Γ_θ.

$$\Gamma_{\bar{\theta}} = \begin{bmatrix} \Gamma_u & 0_{n \times m} \\ 0_{N \times m} & \Gamma_\theta \end{bmatrix} \tag{5.44}$$

The update law in a form of equation 5.43 guarantees the time derivative of Lyapunov function $\dot{V}(e_{tr}, \Delta\bar{\theta})$ becomes

$$\dot{V}(e_{tr}, \Delta\bar{\theta}) = -e^T Q e \leq 0 \tag{5.45}$$

and thus negative semi-definite. According to Barbalat's lemma defined in reference [34] the tracking error e_{tr} is forced to zero asymptotically as $t \to \infty$. Considering the $\bar{\theta}$ and $\bar{\phi}$ are composed variables as shown in equations 5.36 and 5.37, the update law defined by equation 5.43 can be split into equations 5.46 and 5.47 to define update laws for variables K_u and $\hat{\theta}$.

$$\dot{\hat{K}}_u = \Gamma_u u_{bl} e_{tr}^T P_{lyap} B_{DS} \tag{5.46}$$

$$\dot{\hat{\theta}} = \Gamma_\theta \phi(x_P) e_{tr}^T P_{lyap} B_{DS} \tag{5.47}$$

Update laws in representation defined by equations 5.46 and 5.47 is suitable for the MRAC algorithm implementation.

5.2.2 *Projection Algorithm*

As the MRAC algorithm itself does not fully guarantee the parameter convergence, a robustness modification of MRAC laws known as the "projection algorithm" has to be employed. The projection algorithm holds the estimated parameters within predefined boundaries and does not allow for a parameter drift, causing unexpected controller behavior [23]. The projection algorithm's first step is to define the convex function that defines the boundaries within a parameter space. This function is introduced in equation 5.48

$$f(\hat{\theta}) = \frac{1}{\epsilon} \sum_{i=1}^{n} \left| \frac{\hat{\theta}_i}{\theta_{i,max}} \right|^p - \frac{1}{\epsilon} + 1 \leq 0, \tag{5.48}$$

where the variable $\hat{\theta}_i$ is the estimate of i^{th} adaptive parameter and the variable $\theta_{i,max}$ is the boundary of i^{th} adaptive parameter estimate. The variables p and

ϵ define parameter space boundaries. The gradient of the convex function necessary to compute the projection is defined by equation 5.49.

$$\nabla f(\hat{\theta}) = \frac{2(1+\epsilon)}{\epsilon\theta_{max}}\hat{\theta} \tag{5.49}$$

The projection algorithm itself is defined for 3 cases:

- No scaling, if not in transition zone, i.e. $f(\hat{\theta}) < 0$
- No scaling, if $f(\hat{\theta}) \geq 0$ and vertical component of $\dot{\hat{\theta}}$ points away from the boundary
- Scaling, if $f(\hat{\theta}) \geq 0$ and the vertical component of $\dot{\hat{\theta}}$ points to the boundary

Three projection cases shown in equation 5.50 were described in reference [35].

$$\dot{\hat{\theta}} = \mathrm{Proj}(\hat{\theta}, \dot{\hat{\theta}}) = \begin{cases} \dot{\hat{\theta}} \quad \text{if} \quad f(\hat{\theta}) < 0 \\ \dot{\hat{\theta}} \quad \text{if} \quad f(\hat{\theta}) \geq 0, \nabla f(\hat{\theta})^T \dot{\hat{\theta}} \\ \dot{\hat{\theta}} - f(\theta)\frac{\nabla f(\hat{\theta})^T}{\|\nabla f(\hat{\theta})\|}\dot{\hat{\theta}}\frac{\nabla f(\hat{\theta})}{\|\nabla f(\hat{\theta})\|} \quad \text{if} \quad f(\theta) \geq 0, \nabla f(\theta)^T \dot{\hat{\theta}} \end{cases} \tag{5.50}$$

5.2.3 *Hedging*

Hard input nonlinearities due to the actuator saturation can cause a serious challenge to the adaptive control system operation. The solution is to employ a technique known as hedging, which modifies the reference model dynamics defined by equation 5.31 and enhances it by the difference between saturated input $R_s(u)$ and computed input u [2, 38]. Equation 5.51 describes the input saturation while equation 5.52 expresses the difference Δu.

$$R_s(u) = \begin{cases} u \quad \text{if} \quad u_{min} < u < u_{max} \\ u_{max} \quad \text{if} \quad u > u_{max} \\ u_{min} \quad \text{if} \quad u < u_{min} \end{cases} \tag{5.51}$$

$$\Delta u = R_s(u) - u \tag{5.52}$$

The new dynamics of the reference model, including the information about actuators saturation, is defined by equation 5.53.

$$\dot{x}^*_{ref} = A_{ref}x^*_{ref} + B_{ref}r + B_{PL}(\Delta u) \tag{5.53}$$

The modified reference model state x^*_{ref} is used for computing the new tracking error $e_U = x_{DS} - x^*_{ref}$ which propagate to a new definition of update laws [34], as shown in equations 5.54 and 5.55, respectively.

$$\dot{\hat{K}}_u = \Gamma_u u_{bl} e_U^T P B_{DS} \tag{5.54}$$

$$\dot{\hat{\theta}} = \Gamma_\theta \phi(x_P) e_U^T P B_{DS} \tag{5.55}$$

6

DIGITAL FCS IMPLEMENTATION

The rapid prototyping environment MATLAB® /Simulink® was selected for the FCS implementation due to its strong capabilities in control system design and analysis.

The FCS algorithms introduced in Chapter 5 were at first implemented in the Simulink® environment using its block diagrams. The utilization of the block diagrams instead of the classical programming improves readability, traceability and enables convenient and allows easy modifications of the implemented system, making it useful for rapid prototyping. The next step in the implementation process was the code generation for a target hardware platform used in the experimental aircraft platform.

6.1 LINEAR QUADRATIC REGULATOR IMPLEMENTATION

The LQR controller implemented in Simulink® environment is shown in Figure 6.1. The controller structure is based on the algorithm introduced in Chapter 5. The reference input vector r is composed of 3 command signals, the airspeed V_{cmd}, altitude h_{cmd} and heading ψ_{cmd}. The controller structure itself contains two main parts, namely the Integral Error Dynamics (used for the command tracking) and feedback gain K_{LQR}. The simulation model also contains Actuator Saturation, representing actuator's physical limits, Plant Dynamics and Sensor Noise.

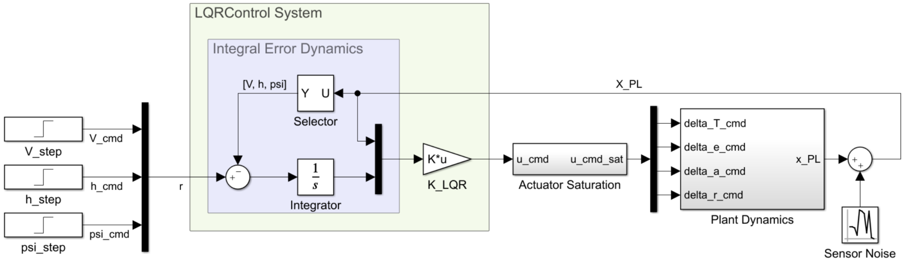

Figure 6.1: LQR simulation model implemented in Simulink® .

The Plant Dynamics structure introduced in Figure 6.2 contains the throttle, elevator, aileron and rudder actuator models connected to the Aircraft Dynamics subsystem in state-space representation. Inputs of the Plant Dynamics subsystems are the commanded control signals generated by the control system. Actuator models process control signals. Every actuator model generates control deflection and rate signal. The control deflections create the input vector to the Aircraft Dynamics subsystem. The output vector of the Plant Dynamics model x_{PL} is composed of the aircraft states and actuator deflections and rates.

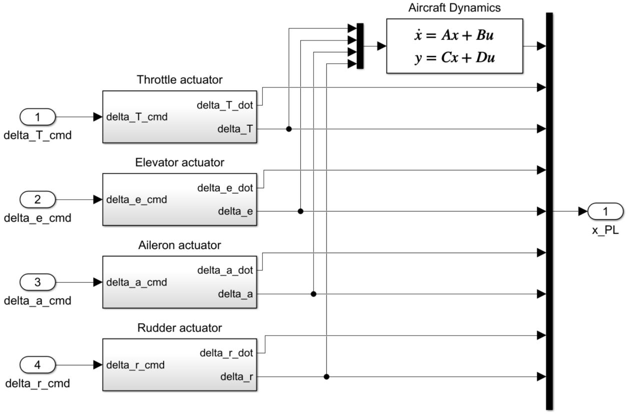

Figure 6.2: Plant dynamics structure.

The actuator dynamics is modeled using a second-order transfer function. The throttle actuator structure shown in Figure 6.3, based on the actuator model introduced in Chapter 3.

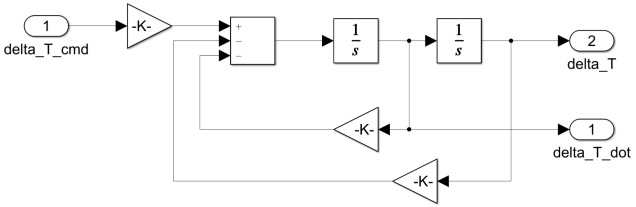

Figure 6.3: Actuator dynamics structure.

6.2 LINEAR QUADRATIC GAUSSIAN CONTROLLER IMPLEMENTATION

The LQG control system implementation in a form of Simulink® block diagram is shown in Figure 6.4. The control system was implemented using the algorithms introduced in Chapter 5. Three main components of LQG controller are the Integral Error Dynamics, Kalman filter and LQR state feedback K_{LQR}. The Plant Dynamics subsystem remaining the same as introduced in Figure 6.2.

The Kalman filter is implemented as a state-space model, which containing the information about controlled plant dynamics in the form of state-space matrices A, B, C, combined with the difference between estimated output $\hat{y}$ and Design System output y_{DS} multiplied by Kalman gain L.

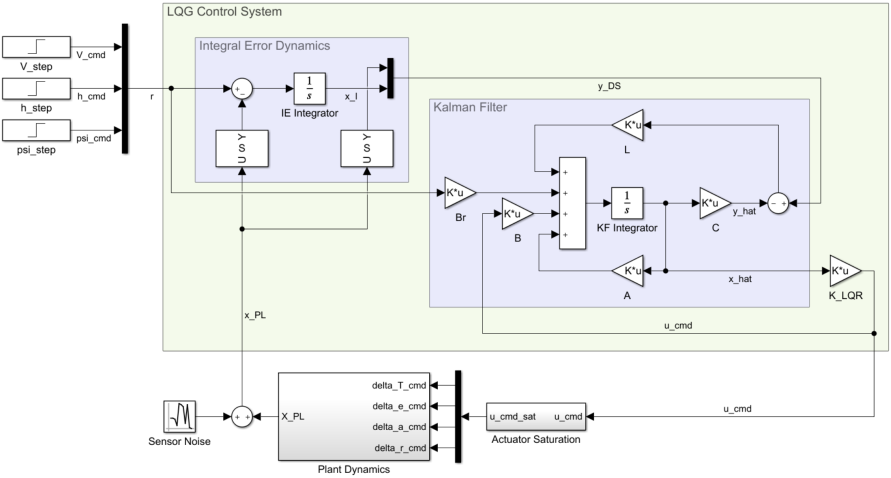

Figure 6.4: LQG simulation model implemented in Simulink® .

6.3 MODEL REFERENCE ADAPTIVE CONTROL IMPLEMENTATION

The MRAC implementation using the Simulink® block diagrams is shown in Figure 6.5. Its design augments the previously described LQR controller selected as the baseline control system. The MRAC system is composed of the Reference Model and Input and State Update Laws. The Reference Model, is extended with the Hedging input u_H to overcome the actuator saturation.

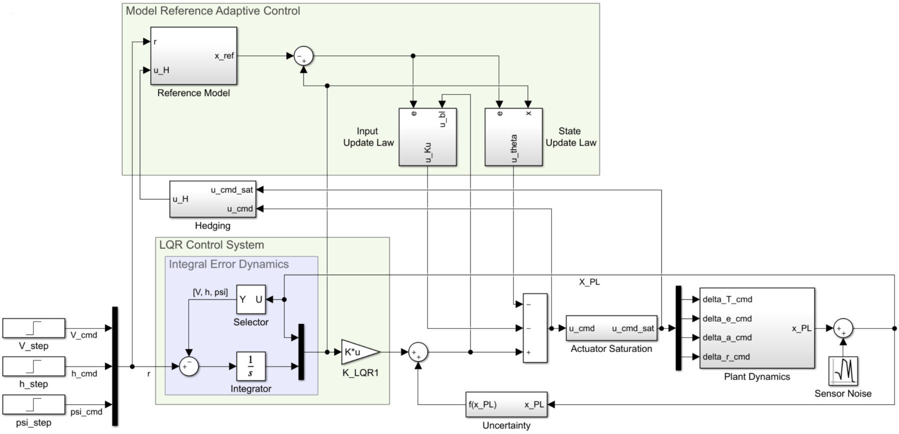

Figure 6.5: MRAC simulation model implemented in Simulink® .

Structure of the Reference Model subsystem is shown in Figure 6.6. The Reference Model dynamics was implemented in a form of a state-space representation defined by matrices A_{ref} and B_{ref} expressed by equations 5.29 and 5.30.

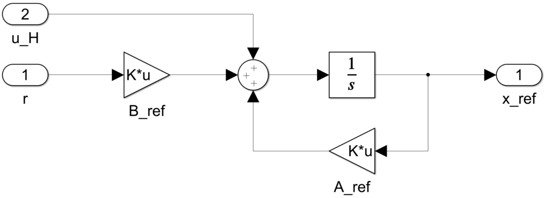

Figure 6.6: MRAC Reference Model subsystem.

The Update Laws defined by equations 5.46 and 5.47 were implemented using a Matlab Function block as introduced in Figure 6.7.

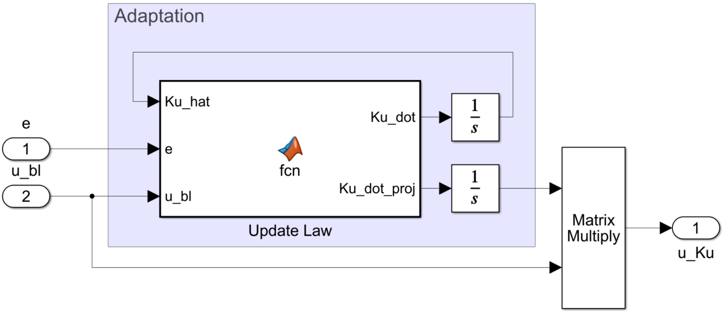

Figure 6.7: MRAC Input Update Law subsystem.

Hedging modification described in Chapter 5 was implemented as a subtraction of the saturated and non-saturated input command signal multiplied by the reference model input matrix B_{ref} as shown in Figure 6.8.

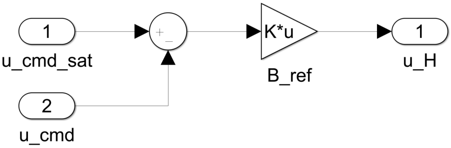

Figure 6.8: MRAC Hedging subsystem.

6.4 CODE GENERATION

The control algorithms implemented using functional blocks in Simulink® can be converted into low-level code like C/C++ directly within MATLAB® environment. This process is called code generation. The generated code can be integrated into a larger project or compiled through a third-party toolchain, and the executable files can be deployed to the target hardware. The code generation process is introduced in block diagram in Figure 6.9 [17].

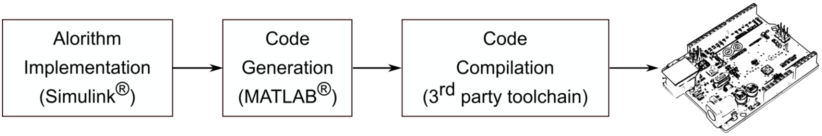

Figure 6.9: Code generation and deployment to the target hardware. Source [17]

The FCS implementations details described in the previous subsections were used mainly for the design and evaluation purposes. They contained the modeled aircraft dynamics and were implemented as continuous-time models. However, the model used for the code generation shall be implemented as a discrete-time model and shall contain only the FCS with defined inputs and outputs.

Figure 6.10 shows the FCS implementation in Simulink® used for code generation with colored inputs and outputs. The blue input ports are used for the aircraft state measurements while the orange input ports are used as command inputs. The yellow output ports send the computed control surfaces and throttle lever deflections to the actuators.

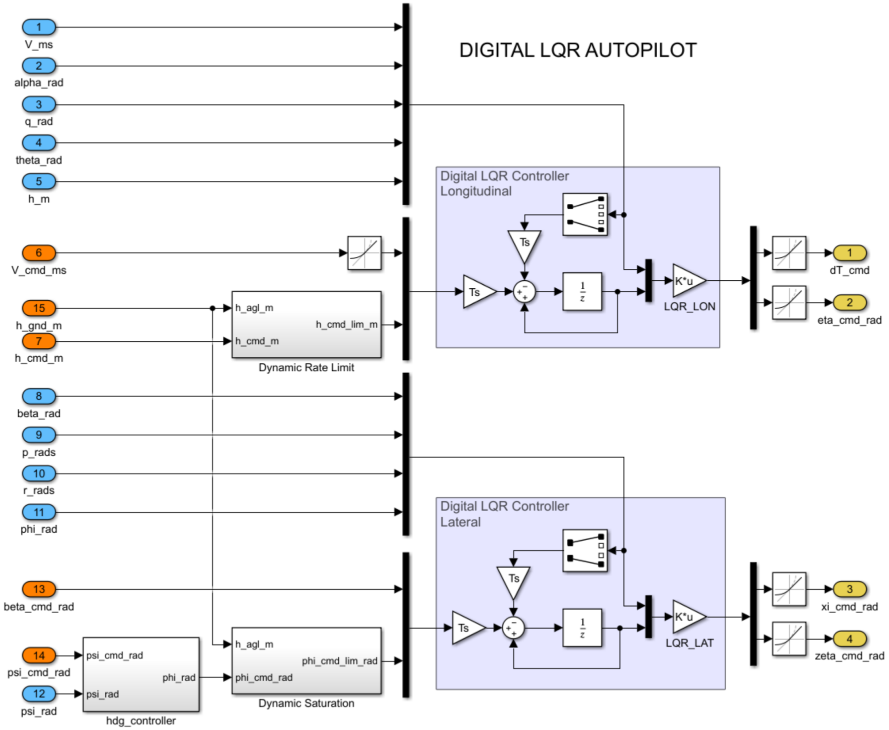

Figure 6.10: Simulink® FCS model used for code generation.

7

DIGITAL FLIGHT CONTROL SYSTEM EVALUATION

This chapter introduces the robustness, performance and flight test evaluations performed with the researched Flight Control System (FCS). The robustness evaluation employs frequency response based techniques as frequency response plots, resulting stability margins or sensitivity functions. The performance evaluation uses offline computer simulations, resulting in time-domain performance analysis using step response characteristics. The robustness evaluation focuses on the baseline controller as it employs techniques suitable for linear systems. This evaluation concept can not be used for adaptive control system designs due to its parameter changes. The performance evaluation validates both, the baseline and the adaptive control design's, time-domain performance. The longitudinal and lateral-directional control systems are to be evaluated separately. The actual flight test evaluation will be investigated in two parts. The first part will focus on the compliance to the criteria inspired by SAE-AS94900 standard for the FCS design, while within the second part an automatic approach to an airport will be tested.

7.1 ROBUSTNESS EVALUATION

The robustness characteristics of designed controllers can be investigated within the frequency domain. The LQG based control techniques generally have worse robustness properties than the LQR based approach due to the additional dynamics introduced by the Kalman filter. Different controller designs can be compared using the robustness evaluation. A favorable robustness can be observed for the case of the LQR design approach, while its noise attenuation exhibits fairly poor results. The LQG design offers good results in noise cancellation but exhibits fairly low stability margins. A good compromise between these two techniques is the utilization of the LTR approach, which improves the stability margins with the noise attenuation potential.

7.1.1 *Longitudinal Controller Robustness*

Tables 7.1 and 7.2 show the computed gain and phase margins in throttle and elevator actuator cuts.

Table 7.1: Comparison of robustness in actuator cut (δ_T) for different controllers.

Controller type	**Gain Margin [dB]**	**Phase Margin [°]**
LQR	∞	80.82
LQG	-18.71	-19.95
LTR(ν = 10)	-13.21	-117.78
LTR(ν = 1)	40.11	103.57
LTR(ν = 0.1)	177.71	52.77
LTR(ν = 0.01)	126.68	84.44

Table 7.2: Comparison of robustness in actuator cut (δ_e) for different controllers.

Controller type	**Gain Margin [dB]**	**Phase Margin [°]**
LQR	-36.16	83.69
LQG	10.25	31.61
LTR(ν = 10)	5.39	28.01
LTR(ν = 1)	8.92	43.49
LTR(ν = 0.1)	26.04	112.39
LTR(ν = 0.01)	12.87	89.81

Figures 7.1 and 7.2 show Bode plots for plant input loop-cuts at throttle and elevator actuators. Stability margins recovery can be observed with the LTR parameter being tuned. Bode plots show an additional roll-off at high frequencies caused by the state estimator and thus good noise attenuation performance for the LQG/LTR techniques. The LQR design suffers from insufficient noise attenuation performance as it does not

contain any state estimator. In the case of noisy measurements, a noise suppression algorithm has to be implemented (e.g., notch filter), which introduces additional time delays in the control loop performance.

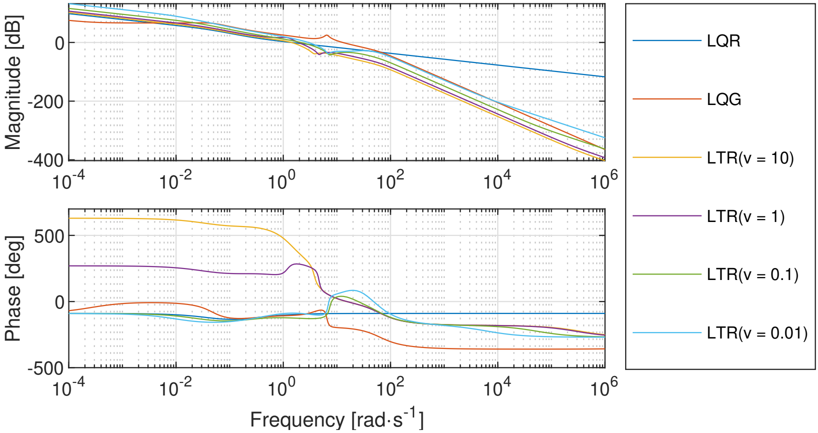

Figure 7.1: Bode plots in throttle actuator cut of different employed controllers.

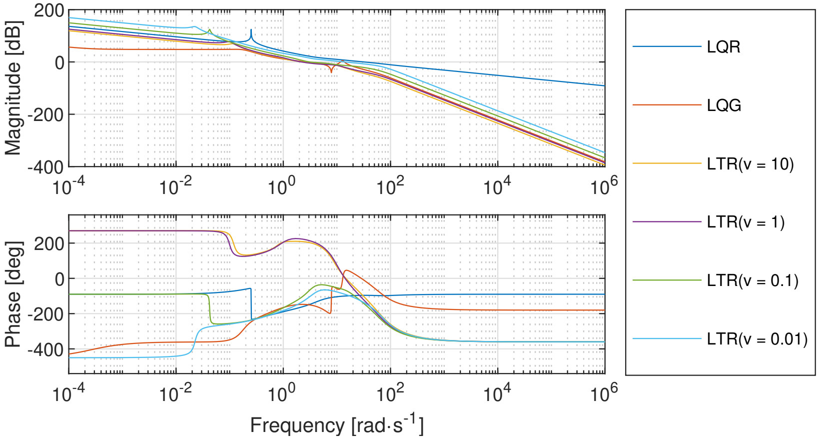

Figure 7.2: Bode plots in elevator actuator cut of different employed controllers.

Figures 7.3 and 7.4 show the Nyquist curves for the Plant input loop-cuts and present the stability margins recovery for the LTR parameter examination, as was also the case for the Bode plots above. The best controller designs, assessed from the perspective of the respective gain and phase margins, are according to the Nyquist plots the LTR based designs with parameters $\nu_1 = 0.1$ and $\nu_2 = 0.01$. These designs represent a balanced combination of robustness and noise attenuation.

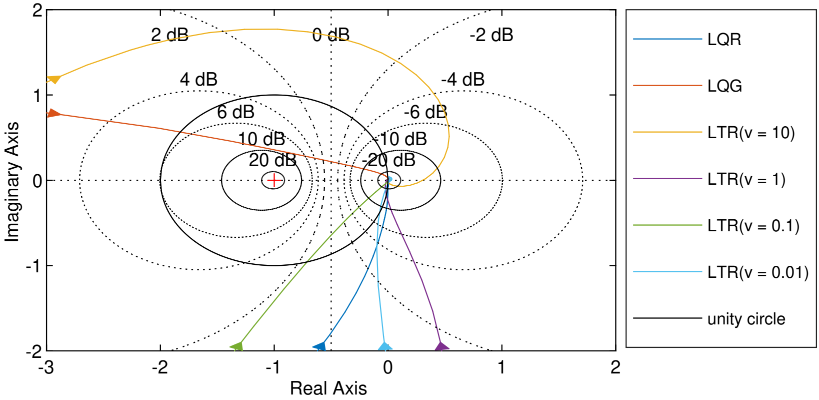

Figure 7.3: Nyquist plots in throttle actuator cut of different employed controllers.

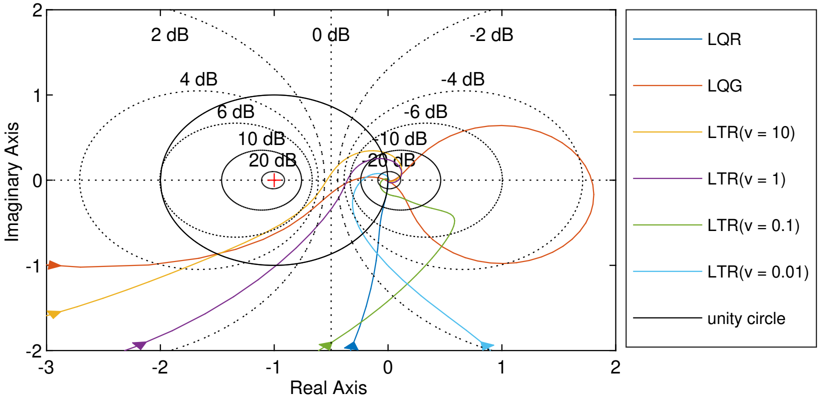

Figure 7.4: Nyquist plots in elevator actuator cut of different employed controllers.

Figures 7.5 and 7.6 present the sensitivity functions for velocity and altitude loops. The sensitivity function is for the investigated case defined as a transfer function from an input reference signal to an output regulation error. The maximum sensitivity peaks are presented in Tables 7.1 and 7.2 and show adequate sensitivity to process disturbances [54].

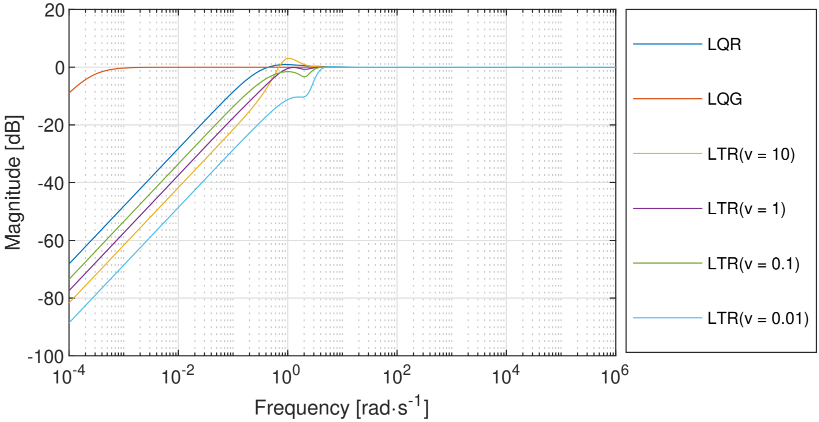

Figure 7.5: Sensitivity functions for different controller types - sensor cut in velocity measurement loop.

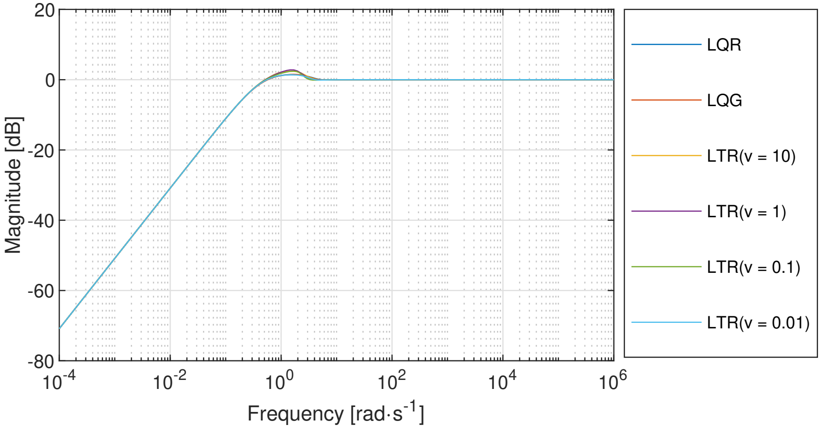

Figure 7.6: Sensitivity functions for different controller types - sensor cut in altitude measurement loop.

Table 7.3: Comparison of sensitivity function maximum in sensor cuts (V, h) for different controllers.

Controller type	Max. Sensitivity - V [1]	Max. Sensitivity - h [1]
LQR	1.18	1.11
LQG	1.19	1.00
LTR($\nu = 10$)	1.32	1.43
LTR($\nu = 1$)	1.38	1.01
LTR($\nu = 0.1$)	1.32	1.01
LTR($\nu = 0.01$)	1.18	1.02

7.1.2 *Lateral-directional Controller Robustness*

This subsection provides insight into the robustness characteristics of the researched lateral-directional FCS. Different types of controllers, namely the LQR, LQG, and its modifications using the LTR techniques are compared in frequency domain characteristics. The stability margins in actuator cut and sensitivity function maximums in sensor cut loop transfer functions are presented in Tables 7.4 and 7.5.

Table 7.4: Comparison of robustness in actuator cut (δ_a) for different controllers.

Controller type	Gain Margin [dB]	Phase Margin [°]
LQR	∞	66.48
LQG	4.93	17.61
LTR($\nu = 10$)	18.67	53.30
LTR($\nu = 1$)	-18.55	45.14
LTR($\nu = 0.1$)	14.67	40.83
LTR($\nu = 0.01$)	-5.52	-37.66

Table 7.5: Comparison of robustness in actuator cut (δ_r) for different controllers.

Controller type	Gain Margin [dB]	Phase Margin [°]
LQR	∞	92.56
LQG	4.29	34.69
LTR($\nu = 10$)	38.18	47.18
LTR($\nu = 1$)	36.43	65.97
LTR($\nu = 0.1$)	26.39	39.79
LTR($\nu = 0.01$)	25.15	-81.02

The values of gain and phase margins in Tables 7.4 and 7.5 show the robustness deterioration when compared to the LQR and LQG controller. The stability margins of the LQG control were restored utilizing the LTR modification. The best values of gain margin, phase margin and sensitivity function maximum were achieved when setting the LTR parameter $\nu = 10$.

Figures 7.7 and 7.8 show Bode plots of loop transfer functions formed in aileron and rudder input loop-cuts. The Bode plots show again the insufficient high frequency noise attenuation capabilities of the LQR controller when compared to the LQG or LTR and stability robustness improvement of the LTR designs.

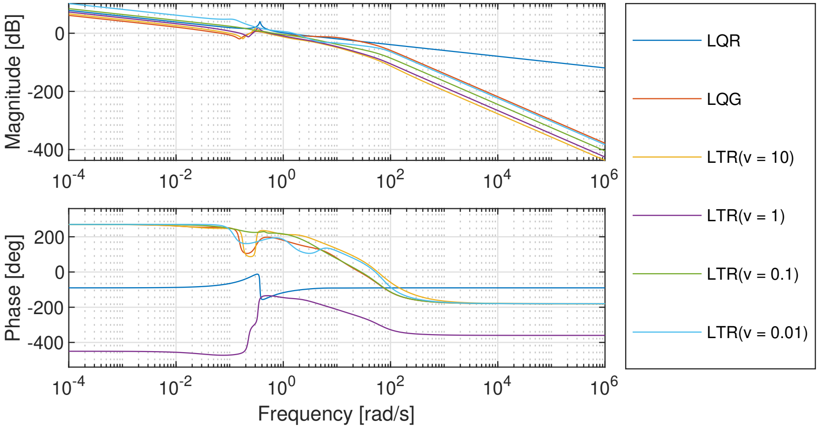

Figure 7.7: Bode plots in aileron actuator cut of different employed controllers.

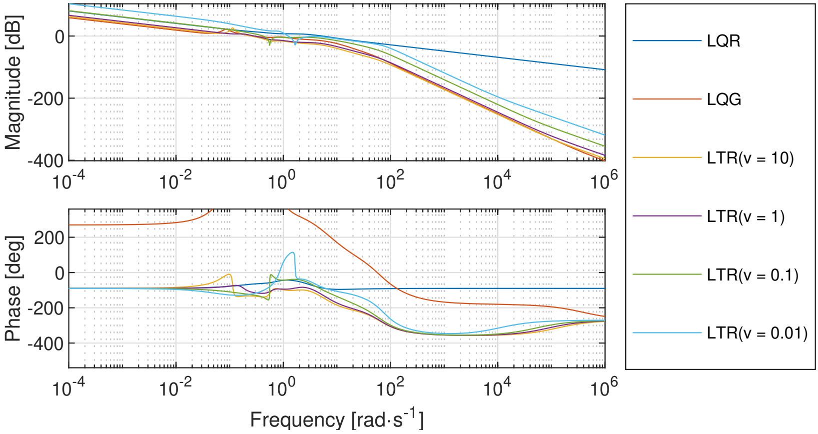

Figure 7.8: Bode plots in rudder actuator cut of different employed controllers.

Figures 7.9 and 7.10 show the Nyquist plots representing the loop transfer function's frequency response in aileron and rudder actuator cuts. The best stability and robustness characteristics according to the Nyquist plot were performed by the LQR, while the LTR modifications improved the stability characteristics of theLQG control system.

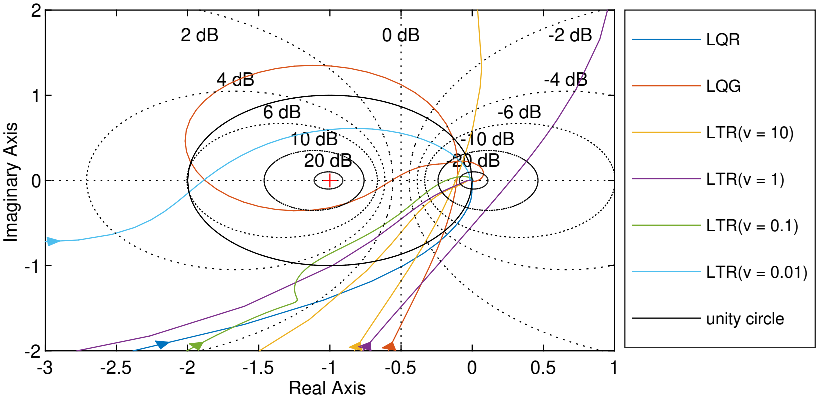

Figure 7.9: Nyquist plots in aileron actuator cut of different employed controllers.

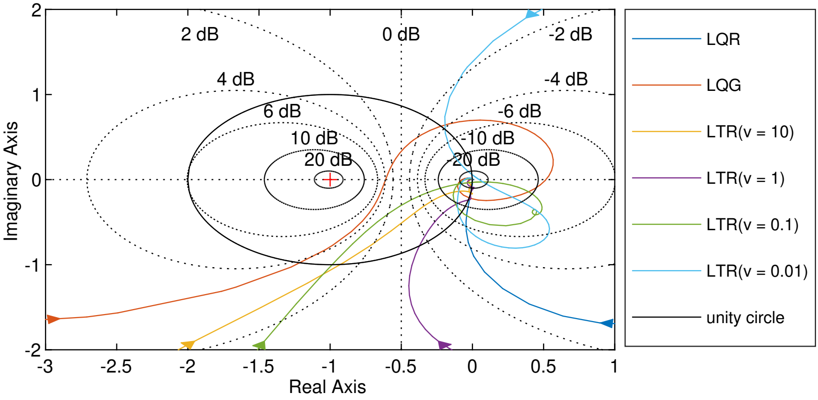

Figure 7.10: Bode plots in rudder actuator cut of different employed controllers.

The sensitivity functions computed at the plant outputs β and ψ (so called sensor cuts) are shown in Figures 7.11 and 7.12.

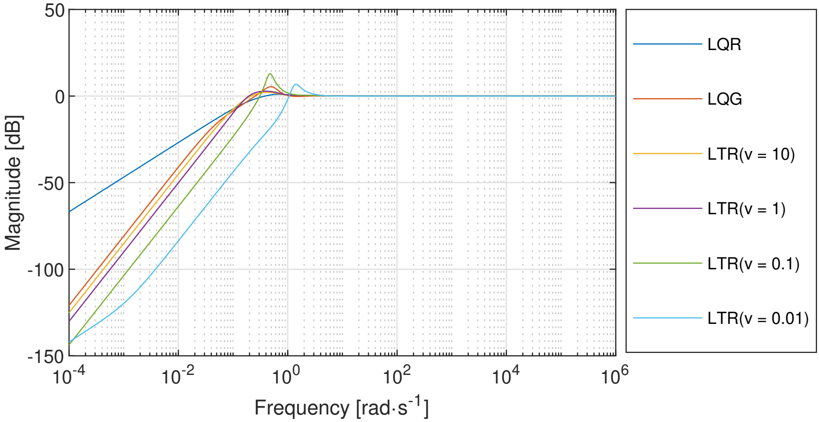

Figure 7.11: Sensitivity functions for different controller types - sensor cut in angle of sideslip loop.

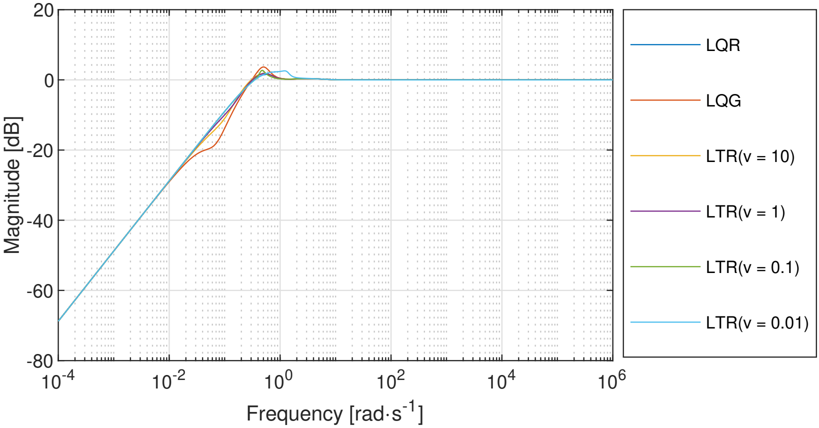

Figure 7.12: Sensitivity functions for different controller types - sensor cut in heading loop.

Table 7.6: Comparison of sensitivity function maximum in sensor cuts (β, ψ) for different controllers.

Controller type	**Max. Sensitivity - β [1]**	**Max. Sensitivity - ψ [1]**
LQR	1.19	1.12
LQG	1.53	1.87
LTR($\nu = 10$)	1.23	1.27
LTR($\nu = 1$)	1.23	1.38
LTR($\nu = 0.1$)	1.37	4.46
LTR($\nu = 0.01$)	1.34	2.20

7.2 PERFORMANCE EVALUATION

The FCS performance can be evaluated by observing the step responses of the closed-loop system. Step response characteristics, namely the rise time, settling time, overshoot, peak value and peak time can be selected as the main performance indicators. The baseline and adaptive controller performances are to be analyzed separately, and both are divided into longitudinal and lateral-directional parts, respectively.

7.2.1 *Baseline Controller Evaluation*

The baseline controller performance was evaluated in computer simulations using the aircraft dynamics in a form of a state-space model introduced in Chapter 2 with modeled actuator dynamics and sensor noise described in Chapter 3. The two designs, the LQR and LQG were considered as baseline controllers, and their performances were compared.

7.2.1.1 *Longitudinal control*

Five different state variables (airspeed V, angle of attack α, pitch rate q, flight path angle γ and altitude h) and 2 control input variables (elevator δ_e and throttle δ_T deflection) were observed for a time-domain performance analysis. The airspeed and altitude were chosen as controlled variables. Step changes of reference airspeed and altitude were performed during the simulation. Figures 7.13, 7.14 and 7.15 show the step response of controlled variables for LQR and LQG control design approaches. As the LQG control employed the Kalman filter for the state estimation, it shows better noise attenuation performance. The control variables, the throttle δ_T and elevator δ_e deflections remained within the saturation limits given by the physical limits of the aircraft.

The time performance characteristics mentioned in the previous paragraph are shown in Table 7.7. Both controlled variables have almost no steady-state error and small overshoot. Short settling time and rise time proves that weight matrices Q and R were selected correctly [54].

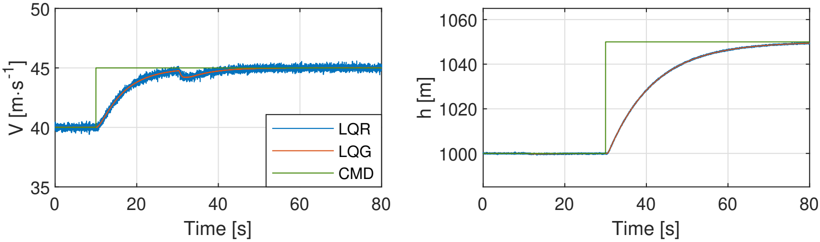

Figure 7.13: Comparison of longitudinal LQR & LQG controllers - command tracking.

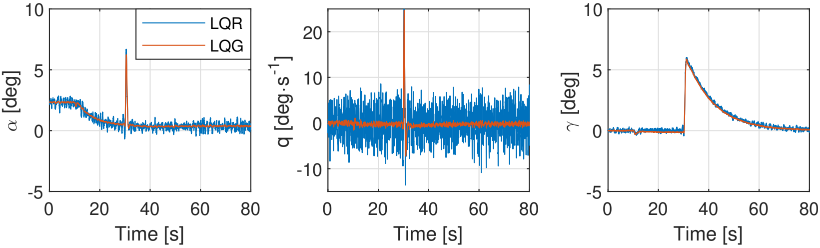

Figure 7.14: Comparison of longitudinal LQR & LQG controllers - plant states.

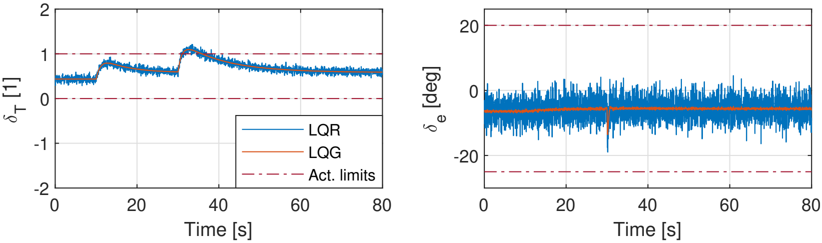

Figure 7.15: Comparison of longitudinal LQR & LQG controllers - plant inputs.

Table 7.7: Time performance characteristics for controlled longitudinal variables in climb.

Command step	$\boldsymbol{\Delta V}$ (+5 m·s^{-1})	$\boldsymbol{\Delta h}$ (+30 m)
Rise Time [s]	3.13	0.84
Settling Time [s]	5.74	7.09
Overshoot [%]	0.00	7.74
Peak [1]	59.99	5.39
Peak Time [s]	8.94	1.88

7.2.1.2 *Lateral-directional control*

The control task performed by the lateral-directional controller is composed of heading angle ψ command tracking and angle of sideslip β regulation to 0 in order to perform the coordinated turn. Figure 7.16 shows the lateral-directional variables controlled by the LQR and LQG controllers.

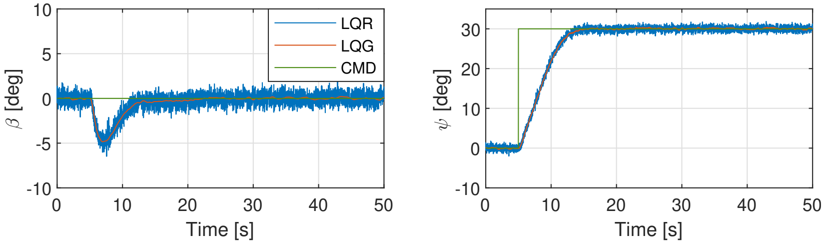

Figure 7.16: Lateral-directional LQR & LQG controllers comparison - command tracking.

Figure 7.17 shows the lateral-directional model states during the heading ψ control task. The Kalman filter state estimates are displayed for the case of the LQG controller, which is the reason why the LQG variables contain less noise. Figure 7.18 displays lateral-directional plant inputs during the heading angle command tracking task. The control deflections did not exceed the actuator's physical limits, due to a conservative controller setting.

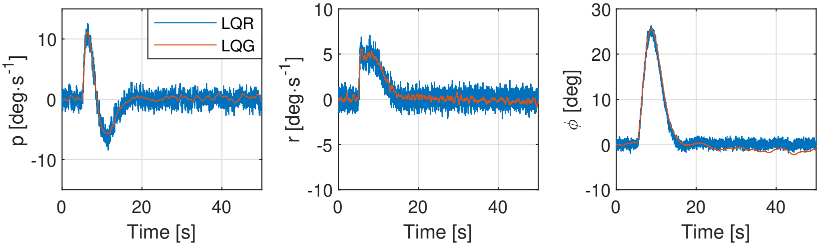

Figure 7.17: Comparison of lateral-directional LQR & LQG controllers - plant states.

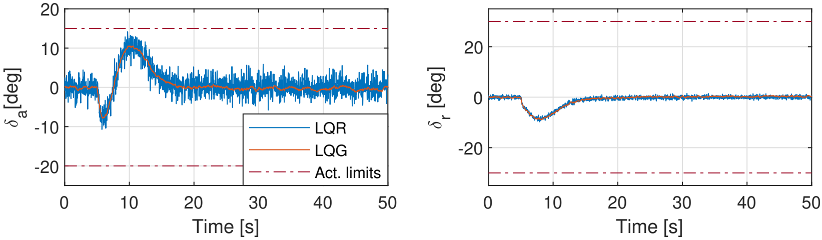

Figure 7.18: Comparison of lateral-directional LQR & LQG controllers - plant inputs.

Table 7.8: Time performance characteristics for controlled lateral-directional variables in level flight.

Command step	$\boldsymbol{\Delta\beta}$ (0°)	$\boldsymbol{\Delta\psi}$ (+ 30°)
Rise Time [s]	0.00	5.88
Settling Time [s]	22.81	13.61
Overshoot [%]	-	0.01
Peak [-]	4.86	30.00
Peak Time [s]	7.13	26.84

7.2.2 *Adaptive Control System Evaluation*

The performance of the adaptive FCS was tested with a simulation model based on the data collected during flight experiments with the utilization of system identification algorithms. The control system maintained preselected airspeed while performing step changes in altitude. During the simulation, a matched uncertainty was introduced to the model in the 250th second. The matched uncertainty affects only the moment equation in the Plant Dynamics and can be directly compensated for by the control surface deflection. The uncertainty was composed of a control effectiveness loss of 50% and a linear state-dependent uncertainty defined by the equations 7.1 and 7.2.

$$f(\alpha, q) = k_\alpha \alpha + k_q q \tag{7.1}$$

$$f(\beta, p, r) = k_\beta \beta + k_p p + k_r r \tag{7.2}$$

where $k_\alpha, k_q, k_\beta, k_p, k_r$ are parameters of uncertainty. The parameter values used in the computer simulations are shown in Table 7.9.

Table 7.9: Control surfaces uncertainty parameter values.

Control element	k_α [1]	k_q [1]	k_β [1]	k_p [1]	k_r [1]
Uncertainty - δ_e	-2.53	-1.06	-	-	-
Uncertainty - δ_a	-	-	-0.21	0.03	-0.99
Uncertainty - δ_r	-	-	-0.21	-13.15	3.13

7.2.2.1 *Adaptive longitudinal control*

During the first simulation, the uncertainty mentioned above was injected into a closed-loop system, which contained only the baseline controller without any adaptation. The uncertainty caused rough oscillations in the altitude control loop, and the closed-loop system became unstable. The instability caused by untcertainty mentioned above is observable in Figure 7.19 after 250th second of simulation.

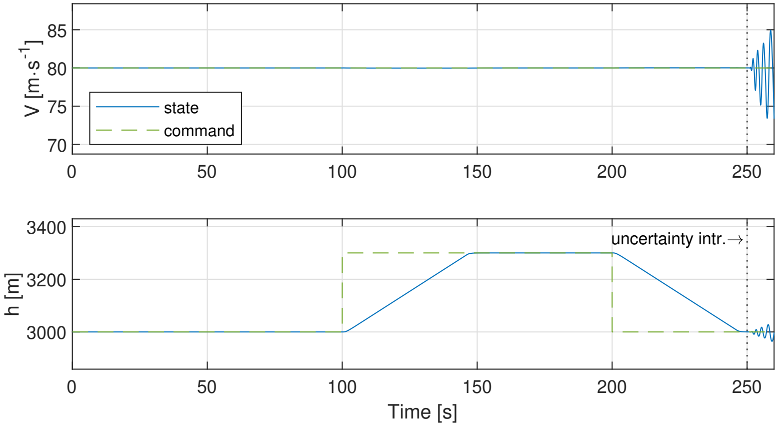

Figure 7.19: Airspeed and altitude control using baseline controller.

Figure 7.20 shows tracked signals of airspeed V and altitude h under active adaptation process. An uncertainty that started the adaptation process was introduced in the 250th second. A small oscillatory response to the first step input occurred after the introduction of the uncertainty. Right after the second step response, the controller maintained minimal overshoot and similar rise time as before the introduction of the uncertainty.

Figure 7.21 shows the remaining states (angle of attack α, pitch rate q and flight path angle γ) in the simulation model to demonstrate the adaptation process. Again, small oscillations are present after the introduction of uncertainty. However, the adaptive controller stabilizes the closed-loop system.

The control surface deflections (throttle δ_T and elevator δ_e) are shown in Figure 7.22 and again demonstrate the ability of the adaptive controller to overcome the uncertainty. The control variables remained within the actuator's physical limits. In

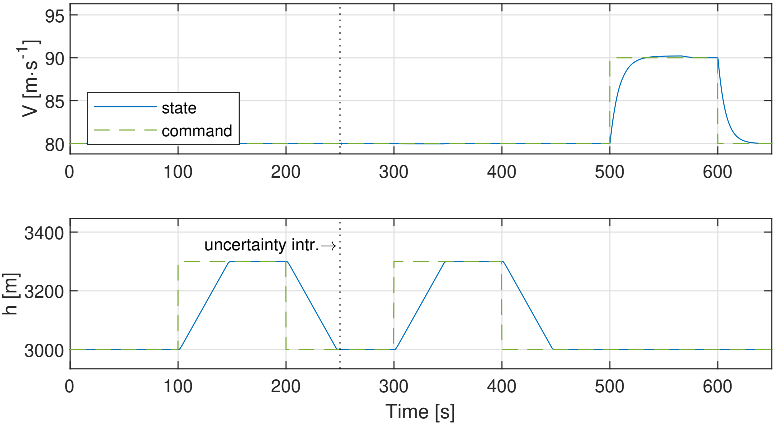

Figure 7.20: Airspeed and altitude control using MRAC

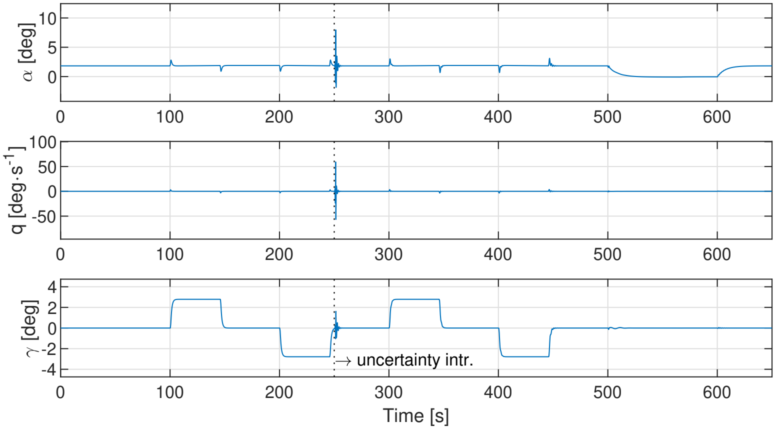

Figure 7.21: Longitudinal state variables under MRAC.

case the actuators would saturate, the hedging algorithm would modify the reference model to compensate for the saturation effect.

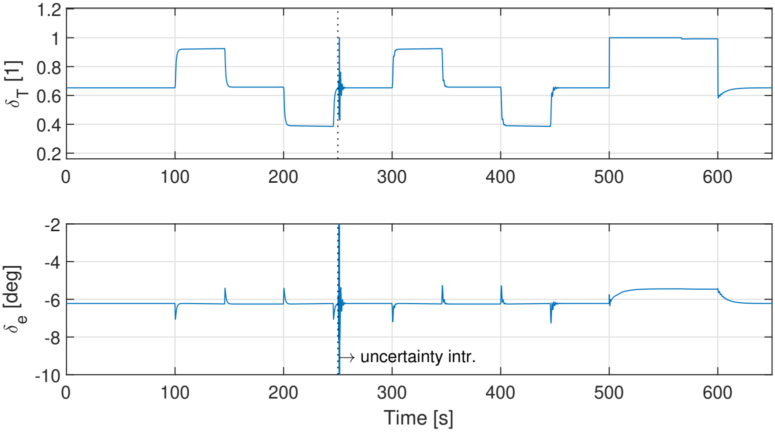

Figure 7.22: Longitudinal input variables under MRAC.

Figure 7.23 demonstrates the change of the adaptive parameters $\hat{\theta}$ and K_u when compensating for the injected uncertainty described in equations 7.1 and 7.2. All eight monitored parameters converge to the optimal values. In the case of a parameter drift, the projection algorithm described in Section 5.2 would keep the parameters within the defined boundaries [53].

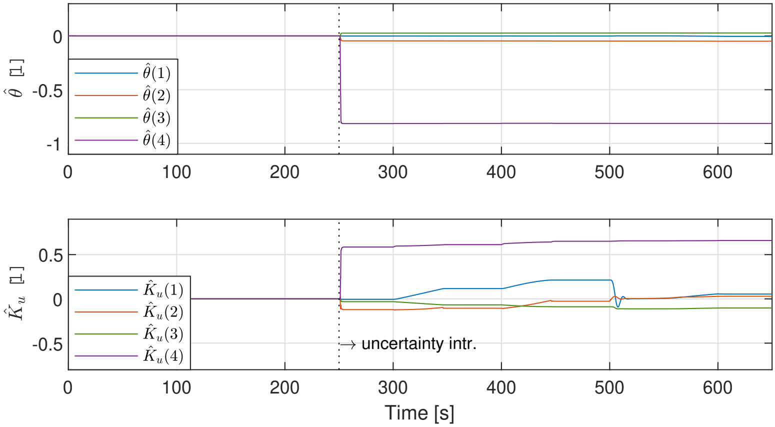

Figure 7.23: Evolution of longitudinal adaptive parameters.

7.2.2.2 *Adaptive lateral-directional control*

The second set of simulations was focused on lateral-directional motion control. The adaptive control system was supposed to track the given heading while maintaining a minimal sideslip angle with the presence of the above-defined uncertainty introduced in the 250th second of the simulation run. Figure 7.24 shows the behavior of the LQR baseline controller without any adaptation under the influence of uncertainty. Violent oscillations can be observed after the onset of the introduced uncertainty.

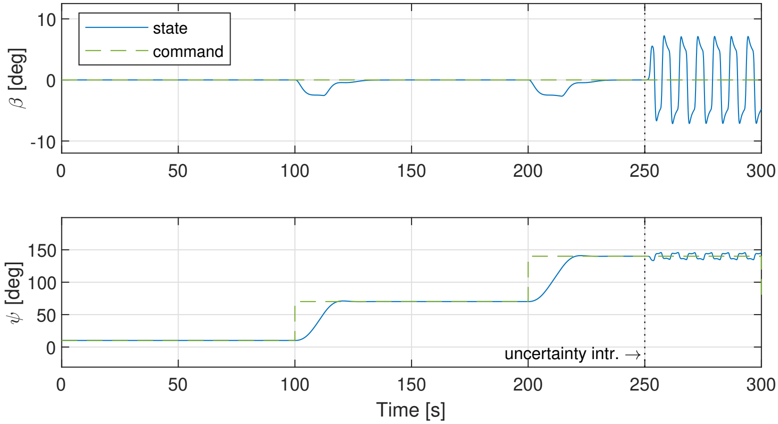

Figure 7.24: Sideslip and heading control using baseline controller.

Figure 7.25 depicts the tracking capabilities of a lateral MRAC controller. The FCS maintains favorable tracking performance of heading angle even after the onset of uncertainty and keeps minimal overshoots and steady-state error. The sideslip angle remains within the 3 degrees interval, which is acceptable.

The remaining lateral-directional states i.e., roll and yaw rates, and the roll angle, can be seen in Figure 7.26. This figure shows a slight oscillation during the first step response after the uncertainty onset. The MRAC controller shows adaptation and a smooth transition during a heading change maneuver in the 400th second.

As seen in Figure 7.27, the control surface deflection remains within the actuator's physical limit. The adaptation process can be seen after the onset of the uncertainty. The reaction to the first step under the uncertainty conditions is slightly oscillatory, while the MRAC controller's reaction to the second heading change is smoother with a minor change in the amplitude.

Figure 7.28 demonstrates the change of adaptive parameters $\hat{\theta}$ and K_u in order to compensate for the injected uncertainty introduced in equations 7.1 and 7.2. As can be seen in Figure 7.28, all eight monitored parameters converge to their optimal values. In the case of a parameter drift, the projection algorithm described in the previous section would keep the parameters within the defined boundaries.

The uncertainty for the lateral-directional motion control case was introduced during a steady level flight. However, the MRAC controller needs to adapt a sufficient

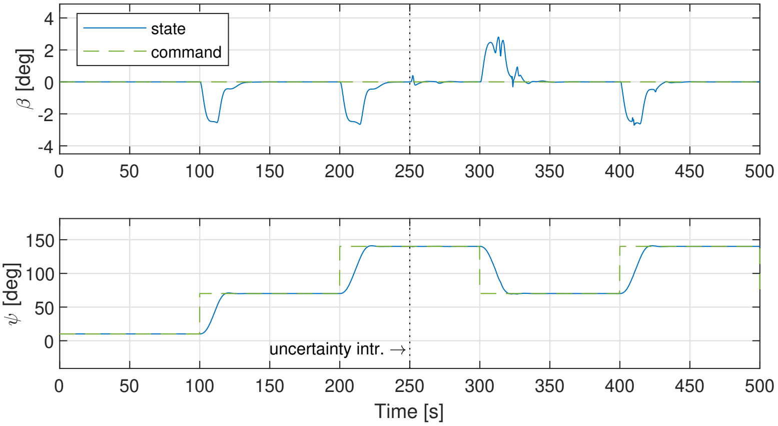

Figure 7.25: Sideslip and heading control using MRAC.

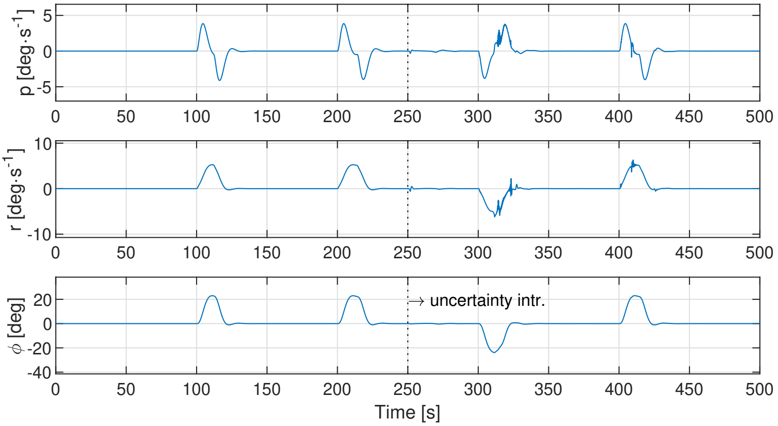

Figure 7.26: Lateral-directional state variables under MRAC.

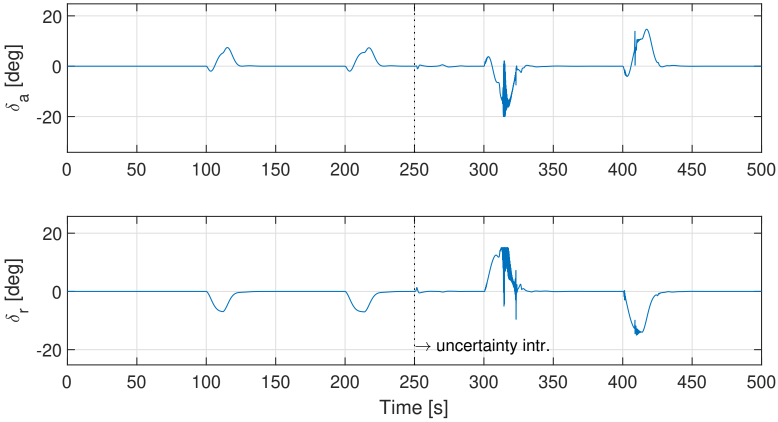

Figure 7.27: Lateral-directional input variables under MRAC.

system excitation, which is why significant parameter changes are observable at the 300th second of the simulation during a heading change and not instantly when the uncertainty is introduced [53].

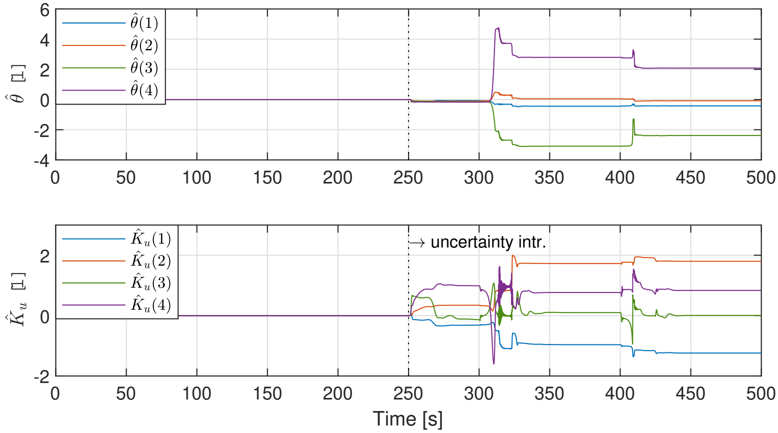

Figure 7.28: Evolution of lateral-directional adaptive parameters.

7.2.2.3 *Adaptive control performance evaluation*

As the adaptation gains change throughout the simulation, the only relevant evaluation criteria are the time domain performance characteristics as the rise time, settling time, overshoot, peak value and peak time. Values of mentioned criteria were monitored after a state-dependent uncertainty was introduced into the simulation. Table 7.10 shows time-domain performance characteristics for longitudinal and lateral-directional simulation cases [53].

Table 7.10: Time-domain performance characteristics for longitudinal and lateral-directional cases.

Command step	$\boldsymbol{\Delta V}$ (+10 m·s^{-1})	$\boldsymbol{\Delta h}$ (+300 m)	$\boldsymbol{\Delta \psi}$ (+70°)
Rise Time [s]	17.28	36.58	12.01
Settling Time [s]	67.33	46.31	19.32
Overshoot [%]	0.24	0.00	1.32
Peak Value [-]	90.22	3300.00	70.91
Peak Time [s]	66.67	100.00	22.64

As the lateral-directional MRAC controller was designed to track the target heading signal while driving the sideslip angle to zero, the time domain performance characteristics are shown only for the heading angle.

7.3 FLIGHT TEST EVALUATION

The operational functionality of the FCS algorithms designed for the automatic flight and automated landing approach has been experimentally confirmed in flight experiments performed with an experimental LSA. This section is divided into two subsections. The first subsection describes the automatic flight results with manually inserted command values of altitude, airspeed and heading. The second subsection is focused on a complex task of automatic landing approach.

7.3.1 *Flight Control System Evaluation*

An important part of the FCS evaluation is the examination of qualitative indicators of automatic control. The reference SAE-AS94900 [42] was employed in evaluation of the FCS design.

7.3.1.1 *Coordination in Steady Banked Turns*

Figure 7.29 shows the aircraft trajectory in an FCS coordinated turn during practical flight experiments. The figure also contains the time series of the angle of sideslip β and lateral acceleration a_y. The quantitative limits for this task specified by reference [42] are shown in respective graphs.

- Increment of angle of sideslip β shall not exceed ±2°.
- Lateral acceleration a_y shall not exceed 0.03 g during steady banks.

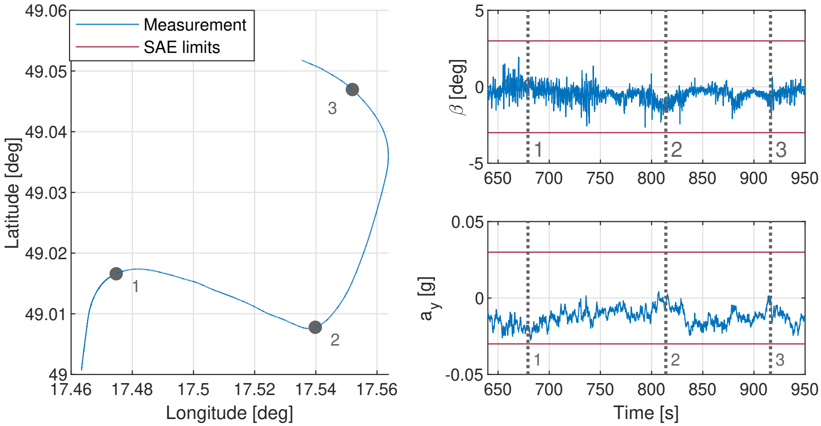

Figure 7.29: Coordinated steady banked turns.

Based on the evaluation of observed criteria defined by regulation [42] the designed FCS fulfills the conditions expressed in paragraph 3.2.4.1.3.1.

7.3.1.2 *Lateral Acceleration Limits During Roll Maneuver*

Figure 7.30 depicts aircraft motion characteristics during roll maneuver with activated FCS. The graphs show time series of lateral acceleration a_y, roll rate p and roll angle ϕ in aircraft's BFF. Every graph contains the quality of control limits taken from paragraph 3.2.4.1.3.2 "Lateral acceleration limits, rolling" of the reference [42]. A short overview of the mentioned criteria is listed below:

- The lateral acceleration a_y in aircraft BFF shall not exceed $\pm 0.1g$ for flight condition with roll rate up to $30^{\circ} \cdot s^{-1}$.
- The limits shall be fulfilled for flight in constant altitude and continuous rolling from one side to the other for maximum roll rate achieved by the FCS.

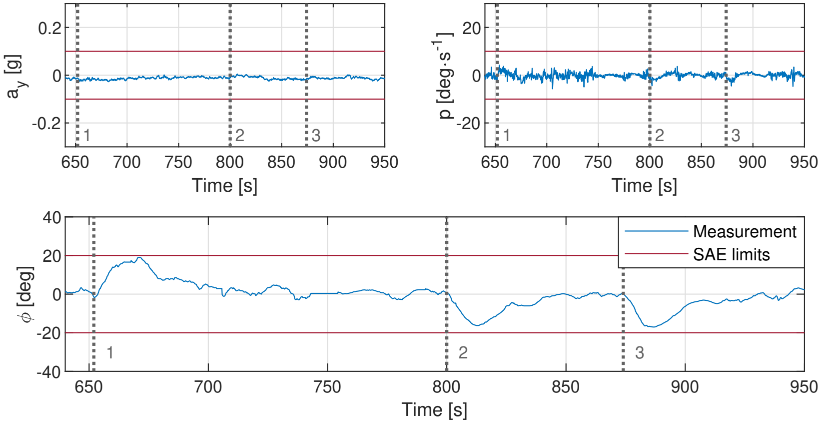

Figure 7.30: Aircraft characteristics during roll motion.

The limit roll angle of 20° comes from an internal setting of the FCS, while the limit roll rate value $10^{\circ} \cdot s^{-1}$ comes from paragraph 3.2.4.2.3 "Heading select" of the reference [42]. Based on the criteria defined by the reference [42], the designed FCS complies to the requirements of paragraph 3.2.4.1.3.2 of mentioned regulation.

7.3.1.3 *Coordination in Steady Level Flight*

Figure 7.31 depicts the aircraft trajectory in FCS controlled steady level flight during a flight test. The figure with aircraft trajectory is completed with plots showing time series of the aerodynamic angle of sideslip β and lateral acceleration a_y during steady level flight. The limit values for FCS performance evaluation are shown in graphs of the angle of sideslip β and lateral acceleration a_y, respectively. The short list of performance criteria defined by paragraph 3.2.4.1.3.3 "Coordination in straight and level flight" of reference [42] are described below:

- The angle of sideslip shall not exceed $\pm 1°$ from the steady-state value in steady level flight.
- The lateral acceleration a_y at the center of gravity shall not exceed $\pm 0.02g$.

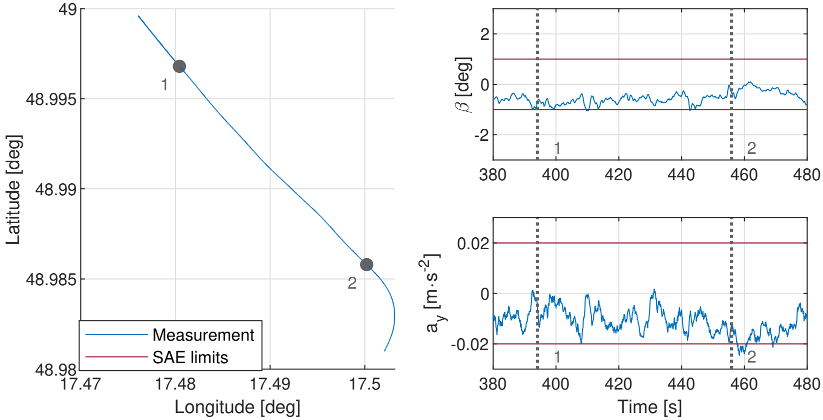

Figure 7.31: Angle of sideslip in steady level flight.

Considering the measurements acquired during the practical flight evaluation, the designed autopilot fulfills criteria of paragraph 3.2.4.1.3.3 from reference [42].

7.3.1.4 *Attitude Hold*

Figure 7.32 shows the aircraft trajectory in a steady level flight during the FCS flight test. The aircraft trajectory is augmented by time series of aircraft attitudes described by respective Euler angles, i.e., roll angle ϕ and pitch angle θ measured in steady level flight. Both graphs with measured aircraft attitude contain respective limit values taken from paragraph 3.2.4.2.1 "Attitude Hold (Pitch and Roll)" of reference [42]. A short list of mentioned criteria is described below:

- For non-turbulent air, the static precision shall be kept within the limits $\pm 0.5°$ for pitch angle and $\pm 1°$ for roll angle with respect to steady-state values.
- In case of a flight in the turbulent atmosphere, the offset in pitch angle shall be lower than 5° RMS, and the offset in roll angle shall not exceed 10° RMS.

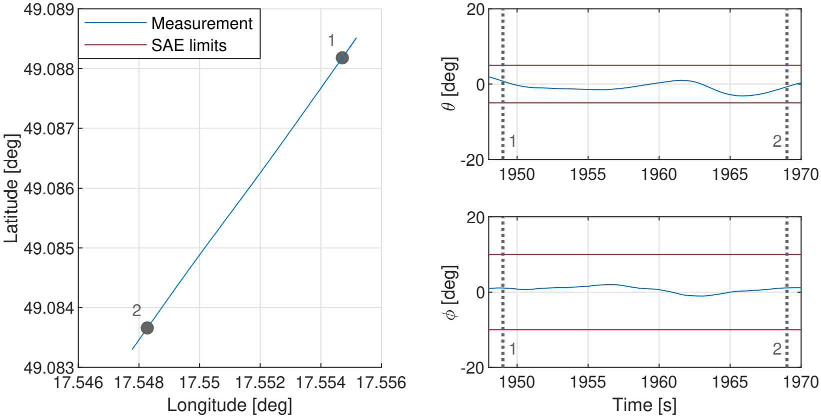

Figure 7.32: Attitude hold mode in steady level flight.

Referring to pitch and roll angle measurements in attitude hold mode it can be concluded that the designed autopilot fulfills conditions of paragraph 3.2.4.2.1 taken from the reference [42].

7.3.1.5 *Heading Hold*

Figure 7.33 introduces an aircraft trajectory during a steady level flight controlled by the researched FCS for the purpose of the flight performance evaluation. The aircraft trajectory is shown in combination with a graph of heading measurement during the steady level flight. The heading measurement graph contains flight performance evaluation limits taken from paragraph 3.2.4.2.2 "Heading Hold" of reference [42]. A short list of mentioned criteria is shown below:

- The steady offset to the reference heading under calm air conditions shall be kept within the range of ±0.5°.
- The offset from the reference heading atmospheric turbulence shall not exceed 5° RMS

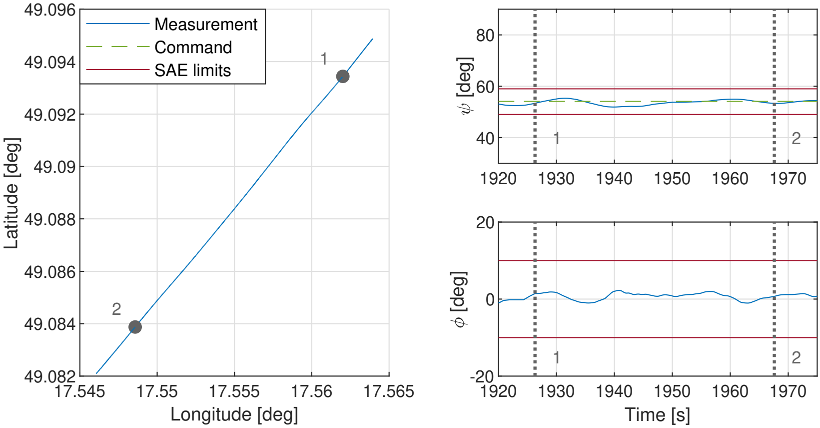

Figure 7.33: Heading hold mode in steady level flight.

Based on the recorded heading measurement during the flight performance evaluation, it can be concluded that the researched autopilot fulfills conditions defined by the paragraph 3.2.4.2.2 of reference [42].

7.3.1.6 *Heading Select*

Figure 7.34 shows the aircraft trajectory during a heading change controlled by the FCS as a part of the flight experiment. The figure also contains the aircraft's trajectory during heading change maneuver, commanded and measured heading and measured roll rate p. Both graphs contain limits for control quality evaluations taken from the paragraph 3.2.4.2.3 "Heading Select" of reference [42]. A short overview of the mentioned criteria is listed below:

- After activation, the FCS shall perform a coordinated turn towards the selected direction with minimal heading change, while maintaining the tolerances mentioned in the subsection Heading Hold.
- The autopilot shall not overshoot the selected heading by more than 1.5° in clean configuration and by more than 2.5° in configuration with flaps.
- The coordinated turn enter and exit shall be quick and continuous.
- The roll rate p shall not exceed $10°\cdot s^{-1}$.

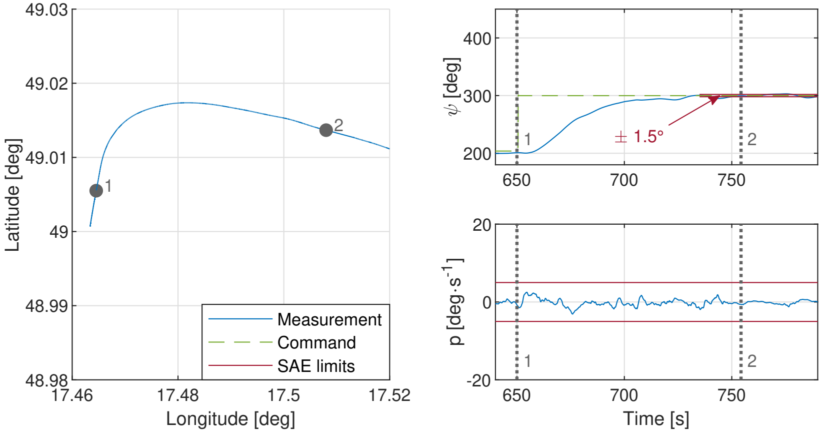

Figure 7.34: Heading select mode in level right turn.

Based on the evaluation of monitored criteria defined by reference [42], it can be concluded that the researched FCS fulfills conditions of paragraph 3.2.4.2.3.

7.3.1.7 *Altitude Select and Hold*

Figure 7.35 shows the aircraft trajectory controlled by the FCS during a flight test. The figure with aircraft trajectory is shown in combination with the time series of aircraft pressure altitude h and normal acceleration a_z. These graphs contain FCS evaluation limits, which were taken from paragraph 3.2.4.2.4 "Altitude Hold and Altitude Select" of reference [42]. A short review of the mentioned criteria is listed below:

- For the vertical speed below $\pm 2000\,\mathrm{ft}\cdot\mathrm{min}^{-}1$, engaging the autopilot shall lead to maintaining current pressure altitude or setting commanded altitude that would be maintained by the autopilot. Acceleration in z-axis shall not exceed $\pm 0.5\,\mathrm{g}$.
- Minimal control accuracy for altitude below $30000\,\mathrm{ft}$:
  - For roll angle 0°-1°, the altitude accuracy shall be within the range $\pm 30\,\mathrm{ft}$.
  - For roll angle 1°-30°, the altitude accuracy shall be within the range $\pm 60\,\mathrm{ft}$ or 0.3%, consider the larger limit.
- After autopilot engage or after any vertical speed instability lower than or equal to $2000\,\mathrm{ft}\cdot\mathrm{min}^{-}1$, the specified instability shall be recovered until $30\,\mathrm{s}$.
- Periodical oscillations shall have a period of at least $20\,\mathrm{s}$.

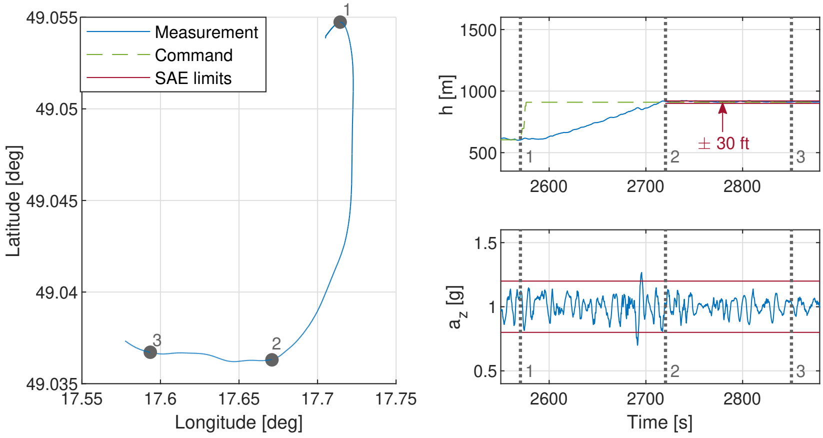

Figure 7.35: Altitude select mode.

Based on the evaluation of monitored criteria defined by reference [42], the researched FCS fulfills conditions of paragraph 3.2.4.2.4.

7.3.1.8 *Airspeed Hold*

Figure 7.36 shows an aircraft trajectory in steady level flight maintained by the FCS during flight experiments. The figure with flight trajectory is shown in combination with a graph of airspeed time history during automatic flight. It shows limits of flight quality criteria, which were taken from paragraph 3.2.4.2.6 Airspeed Hold in reference [42]. A short list of mentioned criteria is described below:

- The airspeed during FCS engagement is taken as a reference value.
- The airspeed shall be maintained within ±2% boundary of reference value or ±5 kts.
- Any periodical oscillation within the above mentioned limits shall have a minimum period of 20 s.

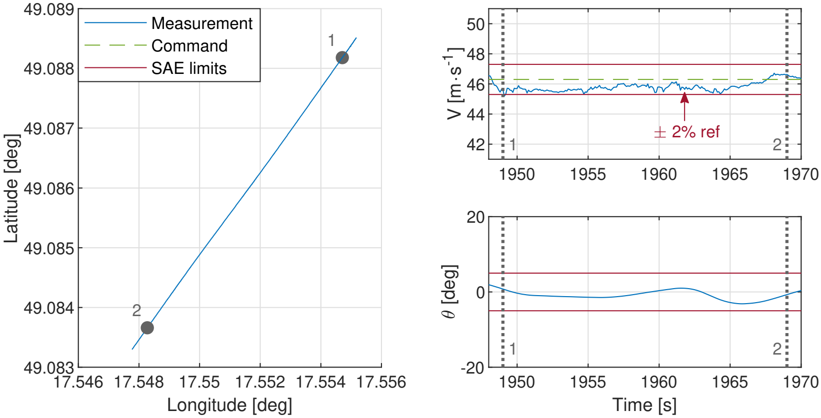

Figure 7.36: Indicated Airspeed hold mode in steady level flight.

Based on the above-described requirements defined by the reference [42] it is obvious that the designed FCS fulfills the conditions specified by paragraph 3.2.4.2.6. The airspeed remains within a ±2% boundary during the observed period, the pitch angle does not exceed ±5° limit specified in the previous subsections.

7.3.2 *Automatic Approach System Evaluation*

The functionality of the researched algorithm for the automatic flight, including autonomous approach for landing was proven feasible through a series of flight experiments performed on an experimental LSA equipped with a digital FCS introduced in Chapters 5 and 6. The flight experiments were performed at the LKKU airport at the end of the year 2018 [6].

Figure 7.37: Experimental aircraft approach to LKKU RWY 20 in an automatic mode.

The experiment was designed to consist of a flight along a predefined rectangular trajectory inspired by a regular flying circuit pattern. During the flight experiment, the test pilot approached the 1st WayPoint (WPT) of the trajectory illustrated in Figure 7.38 in a steady level flight at altitude 1000 ft AGL and 60 kts Indicated Airspeed (IAS). The actual automatic approach mode was engaged by the pilot using a dedicated push-button on the control stick. Figure 7.37 shows the experimental aircraft's instrument panel, containing the digital autopilot's Primary Flight Display (PFD) and Multifunction Display (MFD) set to an automatic approach for landing mode during the landing maneuver.

The weather conditions including the wind speed and direction, air temperature, and QNH encountered during the presented experiment are listed in Table 7.11. Effects of wind, occasional atmospheric turbulence and low temperatures were successfully managed by the researched digital FCS, which steered the aircraft towards the runway.

Figure 7.38 shows the flight test trajectory conveniently defined by four WPTs and the position of the LKKU's runway in the WGS-84 coordinate system. The blue line indicates the aircraft's position while the red marker indicates the point when the autopilot has been engaged the autopilot is engaged. Grey circles mark WPT position of the flight test trajectory.

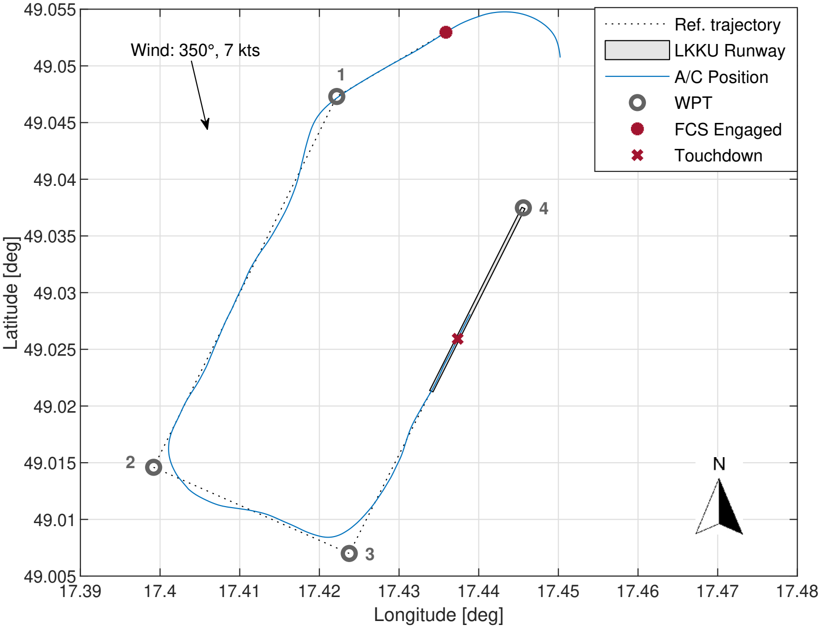

Figure 7.38: Trajectory flown during the automatic landing approach experiment.

Table 7.11: Weather conditions at LKKU at the time of the experiment.

Quantity	**Value**	**Unit**
Wind Speed	7	[kts]
Wind Direction	350	[°]
Temperature	-2	[°C]
QNH	1014	[hPa]

As illustrated in Figure 7.38, the FCS guides the experimental aircraft directly towards the 1st WPT and than follows the predefined flying pattern. Minor oscillations can be observed after passing 1st and 2nd WPT. These can be attributed to the wind conditions, which are represented by an arrow in Figure 7.38.

Figure 7.39 shows the principal quantities controlled by the FCS, namely the airspeed V, altitude h and aircraft heading ψ. Altitude and airspeed command values are defined by fixed step functions related to the current WPT towards which the aircraft is flying. The vertical speed was limited to -2 m·s^{-1} during most of the descent and -1 m·s^{-1} right before touchdown. This limit is responsible for the ramp shape of the altitude command signal. The heading command is computed continuously, in order to navigate the aircraft along the predefined trajectory considering the actual aircraft position. The algorithm for computing the heading command is introduced in thesis Appendix. It is noticeable to mention that minor differences in maintaining the target airspeed V occurred during the descent. However, the FCS was able to guide the aircraft to the runway.

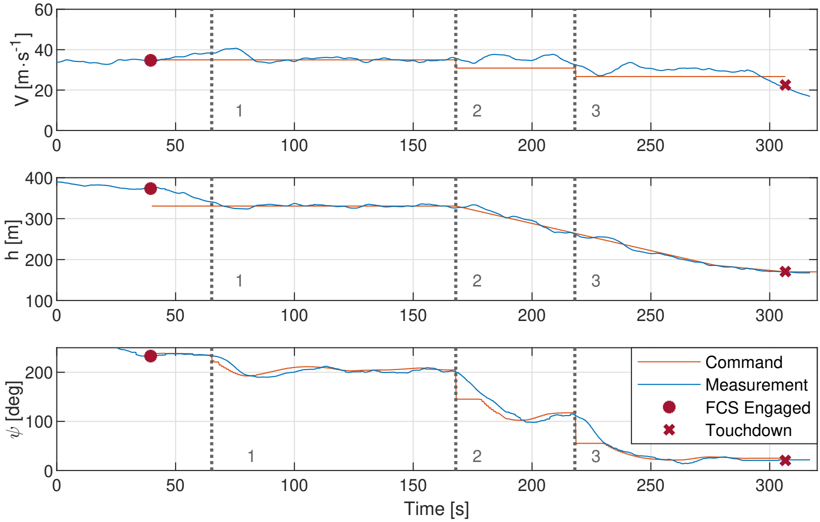

Figure 7.39: Measured flight quantities during automatic landing approach.

Figures 7.40 and 7.41 depict the rest of the aircraft states, namely the values which describe the lateral-directional motion i.e. the lateral acceleration a_y, roll rate p and roll angle ϕ. The roll angle ϕ rotation to -20°, introducing a turn in the trajectory is observable after passing each WPT. The lateral acceleration a_y is maintained close to 0 g, as the FCS is performing a coordinated turn and compensates the lateral acceleration through the use of the rudder. The roll rate p is maintained within $\pm 10°\cdot s^{-1}$ interval. The longitudinal motion is described by normal acceleration a_z, pitch rate q and pitch angle θ. The decrease in pitch angle θ is observable after passing 2nd WPT as the FCS initiates a descent. Since the digital FCS was set conservatively, the accelerations almost never exceeded the ±0.2 g acceleration range [55]. Both Figures 7.40 and 7.41 illustrate the design limits of the FCS inspired by the reference [42].

The digital 4-axis FCS controlled the elevator, rudder, ailerons and throttle lever. Figure 7.42 shows their deflections during an automatic flight and approach for landing. It is observable that the FCS is set very conservatively since changes in control surface deflections are rather slow and do not exceed operational limits illustrated by respective red boundaries.

Since the complete flight experiment was performed in clean aircraft configuration, it was not allowed to use flaps as aerodynamic breaks. This explains the steady-state error in airspeed during the descent maneuver, when thrust control reached its lowest limit. Other aircraft states remained within the design limits introduced in subsections 7.3.1.1 - 7.3.1.8.

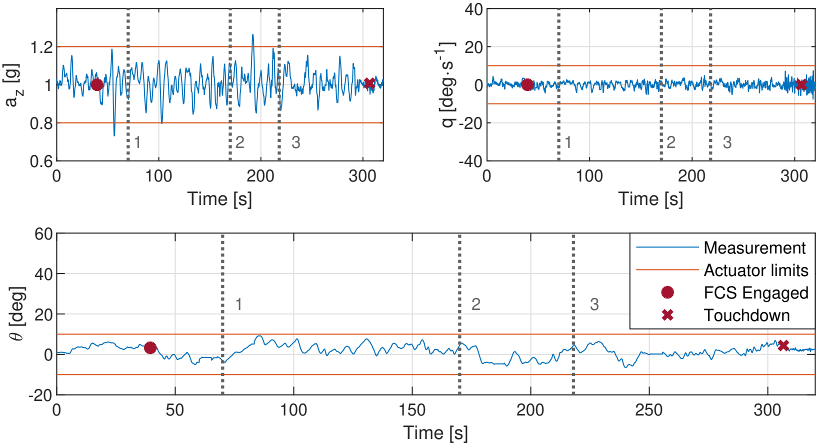

Figure 7.40: Longitudinal variables.

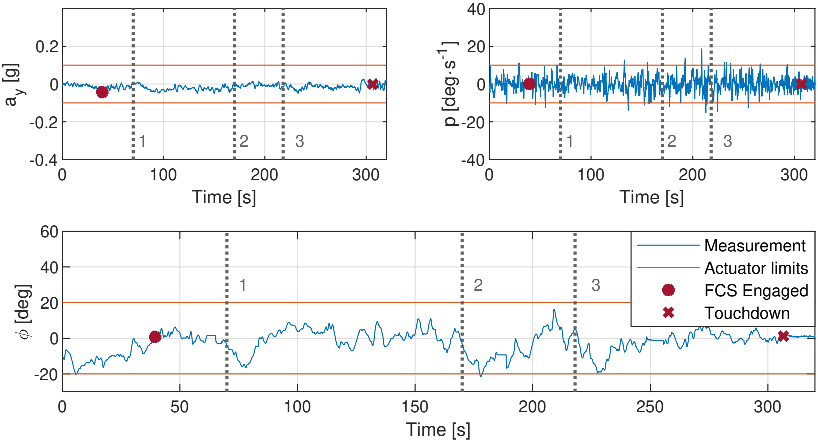

Figure 7.41: Lateral-directional variables.

7.3.2.1 *Automatic Landing Approach Performance Evaluation*

The performance evaluation criteria were inspired by the reference [45] focused on the development of the auto-land system for a general aviation class of aircraft. The document recommends that pitch angle before the touchdown shall be larger than 5° otherwise, the front gear could be damaged during the automatic landing. The vertical speed before the touchdown shall remain within the interval of $\langle 0.3; 2.0\rangle$ m·s^{-1}. Greater values could be unpleasant for the pilot. The automatic landing approach system shall prevent the aircraft from stall, thus the airspeed V during touchdown shall remain above the stall speed, which is declared by the manufacturer at 42 kts, which is

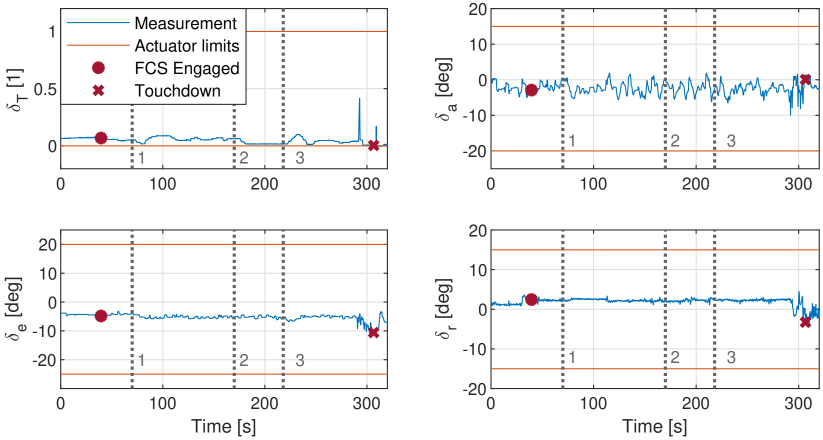

Figure 7.42: Control deflections.

21.6 m·s^{-1}. The designed automatic approach system for fixed-wing experimental LSA complied with the above-mentioned requirements, as can be seen in Table 7.12, which summarizes the performance metrics results, consisting of different aircraft variables measured during the final phase of an automatic landing approach. These variables are the pitch attitude θ, vertical speed VS, airspeed V and normal acceleration a_z [55].

Table 7.12: Measured flight quantities during the automatic approach final phase.

Quantity	**Value**	**Unit**
Pitch angle	5.4	[°]
Vertical speed	-0.33	[m·s^{-1}]
Airspeed	25	[m·s^{-1}]
Normal acceleration	1.01	[g]

CONCLUSION 8

This chapter summarizes and discusses the research on modern FCS introduced in this thesis in light of the main goals and contributions specified in Chapter 1. This chapter is logically divided into three sections. The first section serves as the thesis summary and contains a concluding remark on most of its chapters. The second section lists main contributions and the last section proposes the direction of future research focused on the modern FCS technologies.

8.1 SUMMARY

This thesis demonstrates a modern FCS design, implementation, and stability and performance evaluation using computer simulations and flight tests tailored for a fixed-wing LSA. Chapter 2 was dedicated to the definition of the aircraft's 6DoF nonlinear model. A precise model and selected structure of the controlled plant, in our case representing an experimental LSA, is essential in designing a well performing FCS. The nonlinear aircraft dynamic model was developed from Newton's laws, in a form of Equations of Motion. The nonlinear system was then linearized to express the aircraft dynamics in a form of a linear state-space model suitable for the FCS research and development. Chapter 3 focused on the description of respective subsystems that represent a suitable simulation environment and which enabled the first tests of researched control strategies. Models describing the aircraft propulsion, aerodynamic properties, actuator and sensor dynamics, or atmospheric model, represent an integral part of the simulation framework. Leveraging the aircraft's aerodynamic model fidelity was achieved through utilization of the parameter estimation methods described in Chapter 4. The aerodynamic force and moment coefficients were estimated using the Equation Error method over a range of measured flight parameters. This chapter also presents the state estimation technique, namely the Kalman filter, employed in the FCS design. Chapter 5 introduced the necessary theory on three control system methods, which enabled their proper understanding and follow on research. This chapter started with a robust LQR controller and its adjustment to the command tracking task. Then a more complex LQG controller containing the Kalman filter was researched. The chapter was concluded with the MRAC technique that augments previously defined control system to overcome model uncertainties. Chapter 6 described the implementation of the designed FCS using MATLAB® / Simulink® environment. This chapter introduced the implementation of the control system methods from Chapter 5 and the low-level code generation for the target hardware platform. Chapter 7 presented the designed FCS's stability and performance evaluations results. The FCS evaluation was divided into three main parts. The first part was focused on the FCS stability and robustness evaluation in the frequency domain. Its conclusion confirm the LQR being a more robust FCS design method than the LQG. The second part was dedicated to the investigation of the time-domain performance of implemented designs in computer simulations. The LQG controller showed significant noise-attenuation capabilities due to the Kalman filter's presence in the design. The MRAC augmentation, on the other hand, presented its ability to overcome model uncertainties that influenced the aircraft dynamics. The chapter was concluded by presenting the flight experiment results that proved the suitability of the researched FCS.

8.2 THESIS CONTRIBUTIONS

The following list summarizes the main contributions of this thesis.

- High fidelity 6DoF nonlinear aircraft simulation model of an experimental LSA platform refined with estimated aerodynamic coefficients originating from parameter estimation process on measured flight data.
- The FCS design based on the robust LQR control strategy, with its implementation tailored specifically for a LSA.
- The MRAC based adaptive augmentation of a linear FCS evaluated in computer simulations.
- Three-phase evaluation of the designed FCS, including robustness and stability evaluation, time-domain performance evaluation in the simulation environment and a flight experiment evaluation.

8.3 FUTURE DEVELOPMENT

The future development should account for a higher level of aircraft autonomy. Features as automatic take-off and landing should provide a useful extension to the proposed FCS. The next step could account for a transformation from the experimental LSA platform to Remotely Piloted Aircraft Systems (RPAS) by designing the ground control station with Command and Control (C2) link to the aircraft, taking the pilot out of the flight deck and controlling the aircraft remotely.

BIBLIOGRAPHY

[1] B.D.O. Anderson and J.B. Moore. *Optimal Filtering*. Dover Books on Electrical Engineering. Dover Publications, 2012. ISBN: 9780486136899.

[2] A. M. Annaswamy and Jo-Ey Wong. "Adaptive control in the presence of saturation non-linearity." In: *International Journal of Adaptive Control and Signal Processing* 11.1 (1997), pp. 3–19. DOI: 10.1002/(SICI)1099-1115(199702)11:1<3::AID-ACS391>3.0.CO;2-T.

[3] J.L. Boiffier. *The Dynamics of Flight, The Equations*. The Dynamics of Flight. Wiley, 1998. ISBN: 9780471942375.

[4] S.P. Boyd and C.H. Barratt. *Linear controller design: limits of performance*. Prentice Hall Information and System Sciences Series. Prentice Hall PTR, 1991. ISBN: 9780135386873.

[5] P. Chudy, J. Vlk, and P. Dittrich. "Prototyping framework for digital flight control systems." In: *2013 IEEE/AIAA 32nd Digital Avionics Systems Conference (DASC)*. 2013, 7A3-1-7A3–12.

[6] Peter Chudý, Milan Prustoměrský, and Jan Vlk. *Autonomous Light Aircraft Demonstrator Initiative "ALADIN". Popis ověření experimentálního digitálního systému řízení letu*. Tech. rep. Version AWALA 1.2018. Brno, Czech Republic, 2013.

[7] C.K. Chui and G. Chen. *Kalman Filtering: With Real-Time Applications*. Springer series in information sciences. Springer, 2009. ISBN: 9783540878483.

[8] U.S. Department of Defense. *Flying Qualities of Piloted Aircraft, Department of Defense Handbook. MIL-HDBK-1797*. Tech. rep. Washington, DC, 1997.

[9] J. Doyle and G. Stein. "Multivariable feedback design: Concepts for a classical/-modern synthesis." In: *IEEE Transactions on Automatic Control* 26.1 (1981), pp. 4–16.

[10] Bernard Etkin and Lloyd Duff Reid. *Dynamics of Flight: Stability and Control*. Wiley, 1995. ISBN: 0-471-03418-5.

[11] Pieter Eykhoff. *System identification : parameter and state estimation*. English. Wiley-Interscience, 1974. ISBN: 0-471-24980-7.

[12] Florian Fisch. "Development of a Framework for the Solution of High-Fidelity Trajectory Optimization Problems and Bilevel Optimal Control Problems." PhD thesis. Munich, Germany: Technical University of Munich, 2011.

[13] G.F. Franklin, J.D. Powell, and A. Emami-Naeini. *Feedback control of dynamic systems*. Addison-Wesley series in electrical and computer engineering: Control engineering. Addison-Wesley, 1994.

[14] Graham C. Goodwin and Robert L. Payne. *Dynamic system identification : experiment design and data analysis / Graham C. Goodwin and Robert L. Payne*. Academic Press New York, 1977. ISBN: 0122897501.

[15] Robert Goyer. *LSA safety picture emerging*. URL: `https://www.flyingmag.com/pilot-reports/lsa/sport/lsa-safety-picture-emerging/` (visited on 07/19/2020).

[16] Robert A. Granger. *Fluid Mechanics (Dover Books on Physics)*. Dover Publications, 1995. ISBN: 0486683567.

[17] Christoph Hahn. *Code Generation: Run MATLAB Code and Simulink Models Anywhere!* URL: `https://blogs.mathworks.com/racing-lounge/2019/01/02/code-generation-online-tutorial/` (visited on 08/27/2020).

[18] J.P. Hespanha. *Linear Systems Theory*. Princeton University Press, 2009. ISBN: 9781400831890.

[19] Florian Holzapfel. *Lecture notes in Flight Control I*. 2015.

[20] Florian Holzapfel. *Lecture notes in Nonlinear and Adaptive Flight Control*. 2015.

[21] IEEE. *IEEE Standard Specification Format Guide and Test Procedure for Single-Axis Laser Gyros*. Standard. Version 647-2006. New York, NY, 2006.

[22] P. Ioannou and B. Fidan. *Adaptive Control Tutorial*. Advances in Design and Control. Society for Industrial and Applied Mathematics (SIAM, 3600 Market Street, Floor 6, Philadelphia, PA 19104), 2006. ISBN: 9780898718652. URL: `https://books.google.cz/books?id=wyBbyTnxpawC`.

[23] P.A. Ioannou and J. Sun. *Robust Adaptive Control*. Dover Books on Electrical Engineering Series. Dover Publications, Incorporated, 2012. ISBN: 9780486498171.

[24] ISO. *Flight dynamics – Concepts, quantities and Symbols—Part 1: Aircraft motion relative to the air*. Standard. Version 1151-1:1988. Geneva, Switzerland, 1988.

[25] ISO. *Quantities and Units—Part 1: General*. Standard. Version 80000-1:2009. Geneva, Switzerland, 2009.

[26] ISO. *Quantities and Units—Part 2: Mathematical signs and symbols to be used in the natural sciences and technology*. Standard. Version 80000-2:2009. Geneva, Switzerland, 2009.

[27] ISO. *Standard Atmosphere*. Standard. Version 2533:1975. Geneva, Switzerland, 1975.

[28] Ravindra V. Jategaonkar. *Flight Vehicle System Identification (Progress in Astronautics and Aeronautics)*. American Institute of Aeronautics and Astronautics, 2006. ISBN: 1-56347-836-6.

[29] R. E. Kalman and R. S. Bucy. "New results in linear filtering and prediction theory." In: *TRANS. ASME, SER. D, J. BASIC ENG* (1961), p. 109.

[30] Vladislav Klein and Eugene A. Morelli. *Aircraft System Identification: Theory And Practice*. American Institute of Aeronautics and Astronautics, 2006. ISBN: 1-56347-832-3.

[31] Ajoy Kumar Kundu. *Aircraft Design (Cambridge Aerospace Series)*. Cambridge University Press, 2010. ISBN: 978-0-521-88516-4.

[32] H. Kwakernaak and R. Sivan. *Linear optimal control systems*. Wiley-Interscience publication. Wiley Interscience, 1972. ISBN: 9780471511106.

[33] J. LaSalle. "Some Extensions of Liapunov's Second Method." In: *IRE Transactions on Circuit Theory* 7.4 (1960), pp. 520–527.

[34] E. Lavretsky and K. Wise. *Robust and Adaptive Control: With Aerospace Applications*. Advanced Textbooks in Control and Signal Processing. Springer London, 2012. ISBN: 9781447143963.

[35] Miguel Leitao, Florian Peter, and Florian Holzapfel. "Adaptive Augmentation of a Fighter Aircraft Autopilot Using a Nonlinear Reference Model." In: (Jan. 2013).

[36] Sadie P. Livingston and William Gracey. *Tables of Airspeed, Altitude, and Mach Number Based on Latest International Values for Atmospheric Properties and Physical Constants*. Technical Note. Version D-822. Langley Field, VA, 1961.

[37] L. Ljung. *System Identification: Theory for the User*. Prentice Hall information and system sciences series. Prentice Hall PTR, 1999. ISBN: 9780136566953.

[38] R. V. Monopoli. "Adaptive control for systems with hard saturation." In: *1975 IEEE Conference on Decision and Control including the 14th Symposium on Adaptive Processes*. 1975, pp. 841–843.

[39] K.S. Narendra and A.M. Annaswamy. *Stable Adaptive Systems*. Dover Books on Electrical Engineering. Dover Publications, 2012. ISBN: 9780486141428.

[40] J.P. Norton. *An Introduction to Identification*. Dover Books on Electrical Engineering Series. Dover Publications, 2009. ISBN: 9780486469355.

[41] Jan Roskam. *Airplane Flight Dynamics and Automatic Flight Controls: Part 2*. Darcorporation, 2003. ISBN: 1-884885-18-7.

[42] SAE-International. *AS94900: General Specification For Aerospace - Flight Control Systems - Design, Installation and Test of Piloted Military Aircraft*. Tech. rep. 2007.

[43] J.P.L. Salle, J.P. LaSalle, and S. Lefschetz. *Stability by Liapunov's Direct Method: With Applications*. Mathematics in science and engineering : a series of monographs and textbooks. Academic Press, 1961.

[44] R.S. Sánchez-Peña and M. Sznaier. *Robust Systems Theory and Applications*. Adaptive and Cognitive Dynamic Systems: Signal Processing, Learning, Communications and Control. Wiley, 1998. ISBN: 9780471176275.

[45] D. Siegel, Massachusetts Institute of Technology. Department of Aeronautics, and Astronautics. *Development of an Autoland System for General Aviation Aircraft*. Massachusetts Institute of Technology, Department of Aeronautics and Astronautics, 2012.

[46] Z. S. Spakovszky. *Thermodynamics and Propulsion: Performance of Propellers*. URL: `https://web.mit.edu/16.unified/www/FALL/thermodynamics/notes/node86.html` (visited on 07/01/2020).

[47] G. Stein and M. Athans. "The LQG/LTR procedure for multivariable feedback control design." In: *IEEE Transactions on Automatic Control* 32.2 (1987), pp. 105–114.

[48] R.F. Stengel. *Flight Dynamics*. Princeton University Press, 2015. ISBN: 9781400866816.

[49] Robert F. Stengel. *Stochastic Optimal Control: Theory and Application*. Wiley-Interscience, 1986. ISBN: 0-471-86462-5.

[50] Brian L. Stevens and Frank L. Lewis. *Aircraft Control and Simulation*. Wiley-Interscience, 2003. ISBN: 0-471-37145-9.

[51] Ashish Tewari. *Atmospheric and Space Flight Dynamics: Modeling and Simulation with MATLAB® and Simulink® (Modeling and Simulation in Science, Engineering and Technology)*. Birkhäuser, 2007. ISBN: 0-8176-4373-7.

[52] J. Vande Vegte. *Feedback Control Systems*. Prentice-Hall international editions. Prentice-Hall, 1986. ISBN: 9780133129434.

[53] J. Vlk and P. Chudy. "Adaptive Augmentation of an Unmanned Aerial Vehicle's Flight Control System." In: *2018 IEEE/AIAA 37th Digital Avionics Systems Conference (DASC)*. 2018, pp. 1–9.

[54] J. Vlk and P. Chudy. "General aviation digital autopilot design based on LQR/LQG control strategy." In: *2017 IEEE/AIAA 36th Digital Avionics Systems Conference (DASC)*. 2017, pp. 1–9.

[55] J. Vlk, P. Chudy, and M. Prustomersky. "Light Sport Aircraft Auto-Land System." In: *2019 IEEE/AIAA 38th Digital Avionics Systems Conference (DASC)*. 2019, pp. 1–10.

[56] Kevin Wise and Eugene Lavretsky. "Asymptotic Properties of LQG/LTR Controllers in Flight Control Problems." In: Aug. 2012. ISBN: 978-1-60086-938-9. DOI: `10.2514/6.2012-4889`.

JAN VLK

PERSONAL INFORMATION

	Born in Czech Republic, 1st June 1988
email	ivlk@fit.vutbr.cz
website	`https://www.fit.vut.cz/person/ivlk/.cs`

EDUCATION

2007-2010 University of West Bohemia

Faculty of Applied Sciences
Degree: Bc.
Thesis: *Active Control of Ractive Sputtering Process*
Description: The thesis was focused on a control system design for a process of thin layers application.

2010-2012 University of West Bohemia

Faculty of Applied Sciences
Degree: Ing.
Thesis: *Using Image Processing Methods for Polymer's Mechanical Features Recognition*
Description: The thesis was focused on texture analysis of microscopic polymer images and recognition of their mechanical features.

2012-present Brno University of Technology

Faculty of Information Technology
Ph.D. student, focused on Flight Control System design and simulation of flight.

PROJECT EXPERIENCE

2012-2013	TA01010678 - *Smart Autopilot*
2012-2013	7AMB12DE004 - *Evolution based control design in aeroservoelastic phenomena*
2013-2015	TA03010396 - *Integrated simulation platform*
2015	TUM Contract - *Digital Navigation System*
2016	TUM Contract - *Validation of digital avionics system*
2016	TUM Contract - *Development of prototype models*
2017	HONEYWELL Contract - *Turbulence Simulation*
2017	HONEYWELL Contract - *Big Data Smoothing*
2019 - present	TH04010325 - *TREVAL Flight Training Evaluation Software*
2019 - present	TN01000029/02 - *Artificial Intelligence Driven Autonomy*

OTHER INFORMATION

2015	Study internship - Technical University Stuttgart (Germany)
2015	Study internship - Technical University Delft (Netherlands)
2016	Study internship - Technical University Munich (Germany)

INTERESTS

Running · Cycling · Hiking · Music · Photography · Literature